

ELECTRONIC STRUCTURE AND TRANSPORT PROPERTIES OF NANO-MATERIALS

**THESIS SUBMITTED FOR THE DEGREE OF
DOCTOR OF PHILOSOPHY (SCIENCE)
OF THE
JADAVPUR UNIVERSITY**

SOUMENDU DATTA

**SATYENDRA NATH BOSE NATIONAL CENTRE
FOR BASIC SCIENCES
JD BLOCK, SECTOR III, SALT LAKE CITY
KOLKATA 700 098, INDIA**

December, 2008

CERTIFICATE FROM THE SUPERVISORS

This is to certify that the thesis entitled “**Electronic structure and transport properties of nano-materials**” submitted by **Soumendu Datta**, who got his name registered on June 28, 2005 for the award of the **Ph.D. (Science) degree of Jadavpur University**, is absolutely based upon his own work under the supervision of Professor Tanusri Saha-Dasgupta and Professor Abhijit Mookerjee at the S. N. Bose National Centre For Basic Sciences, Kolkata, India and that neither this thesis nor any part of it has been submitted for any degree/diploma or any other academic award anywhere before.

Tanusri Saha-Dasgupta

Associate Professor,

Department of Material Sciences,

S. N. B. National Centre For Basic Sciences,

JD Block, Sector III, Salt Lake City, Kolkata 700 098, India

Date :

Abhijit Mookerjee

Senior Professor and Head,

Department of Material Sciences,

S. N. B. National Centre For Basic Sciences,

JD Block, Sector III, Salt Lake City, Kolkata 700 098, India

Date :

**Dedicated to my
Dada and Parents**

Acknowledgments

First and foremost, I would like to thank my supervisors Prof. Tanusri Saha-Dasgupta and Prof. Abhijit Mookerjee for their continuous support in carrying out this Ph.D. work. They taught me how to approach a problem and how to solve it. They were always ready to listen and modify my ideas to give it a proper direction. They allowed me enough freedom in independent thinking, in selecting new problems and in collaborating with others to bring out my best. Their cooperation and continuous encouragement encandle my responsibility. It was a nice and enjoyable experience to come in contact and work with them.

During this research period, I came in close contact with Prof. D. D. Sarma. We had active collaboration in our work on semiconductor nanoclusters and he carried out several experiments in his laboratory to verify our theoretical predictions. His advice, encouragement and all sorts of help whenever I asked for, have motivated me to do good work. I would also acknowledge my collaboration with Prof. Surajit Sengupta related to transport properties of strained nanosystems and with Dr. Biplab Sanyal of Uppasala University related to magnetic nanoclusters.

I express my sincere gratitude to Prof. Karsten Jacobsen and Dr. Kristian Thegesen for helping me in learning the basics of transport theory in nanocontacts during my visit in their group at Technical University of Denmark. I cannot ever forget the wonderful hospitality and enjoyable discussions with Prof. Michael Springborg and his group mates of University of Saarland, Germany; with Prof. Roser Valenti and her group at Frankfurt University and with Prof. Daniel Sanchez of DIPIC, Spain during my visit in their respective departments.

Life becomes easier when one has good seniors and juniors around. I can still remember my early days of Ph.D. work when my seniors like Monodeep, Mukul, Asit, Aftab used to teach me like school teacher about the coding related to recursion method, cluster calculation etc. I enjoyed very much my collaboration with my colleagues Mukul, Debashish, Manoj and Shreemoyee. As for other members of our group, I would like to thank Molly, Badiur, Moshour, Swarup, Hena, Rudra, Swastika, Soumyajit, Prashant and Jena. Their vibrancy and wonderful attitudes always kept me going and academic discussions with them are also acknowledged. I am taking this opportunity to thank the faculty and staff of my Centre who wished the best for me all times. However, I cannot overlook the silent cooperation provided over the years by my three inanimate friends : nicknamed 'cmr', 'edra1' and 'edra2' (one a HP computer and two super-computers having 14 and 80 processors respectively.)

Financial support by Council of Scientific and Industrial Research (CSIR), Government of India is gratefully acknowledged. Finally, I am also glad to acknowledge Material Research Society of India (MRSI) for giving me the Young Scientist Award, 2008 in recognition of my work.

Soumendu Datta
Kolkata, India
December, 2008

List of Publications

1. **Soumendu Datta**, D. Chaudhuri, Tanusri Saha-Dasgupta and Surajit Sengupta
Electrical transport in deformed nanostrips : Electrical signature of reversible mechanical failure
Europhys. Lett. **73(5)**, 765-771(2006)
2. **Soumendu Datta**, M. Kabir, S. Ganguly, Biplab Sanyal, Tanusri Saha-Dasgupta and Abhijit Mookerjee
Structure, bonding and magnetism of cobalt clusters from first-principles calculations
Phys. Rev. B, **76**, 014429 (2007)
3. M. K. Yadav, **Soumendu Datta**, M. Ghosh, R. Biswas, Arup K. Raychaudhuri and Abhijit Mookerjee
Band gap variation in Mg and Cd doped Zinc Oxide nanostructures and molecular clusters.
Phys. Rev. B, **76**, 195450 (2007)
4. **Soumendu Datta**, M. Kabir, Tanusri Saha-Dasgupta and D. D. Sarma
First principles study of structural stability and electronic structure of CdS nanoclusters
J. Phys. Chem. C, **112**, 8206 (2008)
5. S. Ganguly, M. Kabir, **Soumendu Datta**, Biplab Sanyal and Abhijit Mookerjee
Magnetism in small bi-metallic Mn-Co clusters
Phys. Rev. B, **78**, 014402 (2008)
6. **Soumendu Datta**, M. Kabir, Tanusri Saha-Dasgupta and D. D. Sarma
Study of structural stability and electronic structure of nonstoichiometric CdS nano clusters from first principles
J. Nanosci. and Nanotechnol., **9**, 1 (2009)
7. M. K. Yadav, **Soumendu Datta**, Biplab Sanyal and Abhijit Mookerjee
Study of the electronic and structural properties of ZnO clusters
(**International Journal of Modern Physics B**, in press)
8. **Soumendu Datta**, Tanusri Saha-Dasgupta and D. D. Sarma
Wannier function Study of Relative Stability of Zinc-blende and Wurtzite Structure in CdX (X=S, Se, Te) series
J. Phys. : Condens. Matter, **20**, 445217 (2008)

9. **Soumendu Datta, Tanusri Saha-Dasgupta and Abhijit Mookerjee**
Recursive approach to study transport properties of atomic wire
Eur. Phys. J. B, 66, 57 (2008)
10. **Soumendu Datta, M. Kabir, Tanusri Saha-Dasgupta and Abhijit Mookerjee**
Co clusters : an unusual host in 3d transition metal series
(Under preparation)
11. **Soumendu Datta, M. Kabir, Tanusri Saha-Dasgupta and Abhijit Mookerjee**
Structure, reactivity and electronic structure of vanadium doped cobalt clusters
(Under preparation)

Contents

1	Introduction	1
1.1	Nano-materials - a preview	1
1.2	Bulk and nano-crystalline semiconductors	4
1.3	Transition metal small clusters	6
1.4	Atomic sized conductors	8
1.5	Outline of the thesis	10
2	Theoretical background of electronic structure calculation	15
2.1	The many-body Hamiltonian	15
2.2	Single-particle approximation	16
2.2.1	Wave function approach	16
2.2.2	Density functional theory	17
2.3	General band-structure methods	21
2.3.1	Basis sets	22
2.3.2	Real space recursion method	28
3	Relative stability of zinc-blende and wurtzite structure in bulk CdX (X = S, Se, Te) : a Wannier function study	33
3.1	Introduction	33
3.2	Crystal structure	35
3.3	Total energy calculations	38
3.4	Calculation of ionicity	38
3.5	Microscopic understanding in terms of calculated Wannier functions	41
3.6	Summary and Conclusions	48
4	First principles study of structural stability and electronic structure of CdS nano-clusters	51
4.1	Introduction	51
4.2	Building up of clusters	53
4.3	Computational Details	54

4.4	Results	56
4.4.1	Energy stability	56
4.4.2	Band Gap Variation with cluster size	66
4.5	Summary and Conclusions	70
5	Interplay of structure and magnetism in pure cobalt clusters Co_n ($n =$ 2-20)	74
5.1	Introduction	74
5.2	Computational Details	76
5.3	Results and discussions	77
5.3.1	Trends in structure and magnetism	77
5.3.2	Understanding structural stability	86
5.3.3	Understanding magnetic moments	92
5.3.4	Comparison with other $3d$ transition metal clusters	95
5.4	Summary and Conclusions	100
6	Structure, reactivity and electronic properties of V-doped Co clusters	106
6.1	Introduction	106
6.2	Computational Details	108
6.3	Structure	109
6.4	Stability analysis	114
6.4.1	Cohesive energy	114
6.4.2	Spin gap	117
6.4.3	Density of states	118
6.5	Chemisorption with H_2 molecules	119
6.6	Summary and Conclusions	123
7	Recursive approach to study transport properties of atomic wires	127
7.1	Introduction	127
7.2	Method	130
7.2.1	Converting quasi-1D lead to effective 1D chain and detection of effective scattering region	130

7.2.2	Calculation of the scattering matrix	131
7.3	Application	137
7.3.1	The model	137
7.3.2	Results and discussions	139
7.4	Summery and conclusions	146

List of Figures

1.1	Evolution of the density of states (g's) with dimensionality showing the variation of density of states with energy for bulk solid, quantum film, quantum wire and quantum dot. (Taken from Ref. [20])	2
1.2	The experimentally stable crystal structures of octet AB compounds, WZ = wurtzite, ZB = zincblende, Cinb. = cinnabar, **** means that the compound does not exist. (Table adapted from Ref. [29])	5
1.3	Schematic diagram of the Stern-Gerlach cluster beam experiment (adapted from Ref. [45])	7
1.4	Quantized conductance curve for a gold contact measured at room temperature in UHV by pressing an STM tip into a clean gold surface and recording the conductance while retracing the tip. (Adopted from Ref. [54]). The direction of tip motion is given by arrow.	9
2.1	Recursive reduction of a square lattice to an equivalent linear chain.	29
3.1	(a) and (b) show the crystal structures in WZ and ZB symmetries. Two different coloured atoms denote cation and anion. (c) WZ structure shows the ABAB... stacking of atoms, while (d) ZB structure shows the ABCABC... stacking. <i>Eclipsed</i> and <i>staggered</i> conformation of atoms along <i>c</i> -axis in WZ structure and along [111] body diagonal in ZB structure have been shown in (e) and (f), respectively.	36
3.2	Downfolded bands (thick line) with the basis sets where <i>sp</i> -MTOs are on S atom and <i>d</i> -MTOs are on Cd atom, are compared with NMTO all bands (thin line) both in ZB (left) and WZ (right) structure of CdS. The energy mesh for downfolding have also been shown.	42

- 3.3 The contour plots show the anion $p[111]$ MTO in ZB structure (left panels) and anion $p[001]$ MTO in WZ structure (right panels) of CdX (X = S, Se, Te). The top most panels correspond to CdS and the bottom most to CdTe. In each case, 35 contours have been drawn in the range -0.15 to 0.15 electrons/Bohr³. From top to bottom, the ionicity decreases and the covalency increases. 43
- 3.4 The contour plots show the p -MTO of S along the four nearest neighbour tetrahedral directions in ZB structure (left panels; from top to bottom they are $p[111]$, $p[1\bar{1}\bar{1}]$, $p[\bar{1}1\bar{1}]$, $p[\bar{1}\bar{1}1]$) and in WZ structure (right panels; from top to bottom they are $p[001]$, $p[1, 0, \frac{u}{\sqrt{3}}c/a]$, $p[\frac{1}{2}, -\frac{\sqrt{3}}{2}, -\frac{2}{\sqrt{3}}uc/a]$, $p[\frac{1}{2}, \frac{\sqrt{3}}{2}, -\frac{2}{\sqrt{3}}uc/a]$) of CdS. The contours chosen are same as in Fig. 3.3. 44
- 3.5 (a) Positions of atoms along $[001]$ direction of wurtzite structure, (b) positions of atoms in unit of lattice constant along $[111]$ direction of zinc-blende structure. 45
- 3.6 The above contour plots show the p -MTO of Te in WZ structure of model CdTe. The left panels correspond to $p[001]$ and right panels correspond to $p[1, 0, (u/\sqrt{3})c/a]$. From top to bottom ionicity decreases and covalency increases and distribution becomes more isotropic. The contours chosen are same as in Fig. 3.3. 46
- 4.1 Band gap shift as a function of cluster diameter (taken from Ref. [11]). Solid dots fitted with solid line are results for sp^3d^5 TB model with cation-anion and anion-anion interactions, dashed line for sp^3s^* nearest-neighbour TB-model and the dotted line from the effective mass-approximation. Experimental data points:- CdS: open circles from Ref. [7], open triangles from Ref. [12], stars from Ref. [13], open squares from Ref. [8]; CdSe: open squares from Ref. [14], open triangles from Ref. [15], stars from Ref. [16]; CdTe: open squares from Ref. [17], open triangles from Ref. [18], stars from Ref. [19] 53

4.2	(a) Variation of cohesive energy with size for unpassivated stoichiometric clusters shown by solid dots in ZB structure and by open triangles in WZ structure. Chemical formula for each shell is given both in ZB (upper) and WZ (lower) structures. (b) The cohesive energy difference between WZ and ZB structures for each shell size in the case of unpassivated stoichiometric clusters. For a particular shell number, the diameter of the ZB and WZ structured cluster differ a bit (cf. Table 4.1), therefore the average diameter is shown in the x -axis of the plot. Same convention is followed in all the following plots wherever applicable.	57
4.3	Variation of surface energy with cluster size for ZB (solid dots) and WZ (open triangles) structures for stoichiometric clusters. The inset shows the surface energy difference (SED) between WZ and ZB structures.	58
4.4	Average number of dangling bonds (DB) per surface atom for unpassivated stoichiometric clusters in ZB (solid dots) and WZ (open triangles) structures. The inset shows difference between WZ and ZB structures.	59
4.5	Cohesive energy difference between WZ and ZB structures for each shell size in case of unpassivated non-stoichiometric clusters. (a) Solid dots connected with solid line represent the results for Cd-centred clusters, while (b) the solid triangles connected with solid line correspond to results for S-centred clusters. The consecutive layers of atoms for 2 shell and 3 shell clusters have been shown for both Cd-centred case (spheres with solid line) and S-centred case (spheres with dashed line). Note, by construction even shell Cd(S)-centred cluster is Cd(S) terminated and odd shell Cd(S)-centred cluster is S(Cd) terminated (see text).	60
4.6	Variation of surface energy difference (SED) between WZ and ZB structures, with increasing shell sizes in (a) Cd-centred (represented by solid dots) and (b) S-centred (represented by solid triangles) non-stoichiometric clusters.	61
4.7	Average number of dangling bonds per surface atom (DB) for non-stoichiometric CdS clusters in ZB and WZ structures. The inset shows the difference between WZ and ZB structures. Plot is independent of whether the clusters are Cd-centred or S-centred.	62
4.8	Charge density contribution ($\delta\rho = \rho_t - \rho_a - \rho_s$) around a surface atom of 4-shell non-stoichiometric CdS nano-clusters. The isosurface is chosen at $.007 e^- /(\text{\AA}^3)$	64

- 4.9 Density of states for 4 shell ZB structured stoichiometric cluster. Left panel shows the DOS for unpassivated cluster while the right panel shows the DOS for passivated cluster. Black, red, green and blue lines correspond to total DOS, Cd-contribution, S-contribution and that of H-contribution (in case of passivated cluster only) respectively. 65
- 4.10 Variation of cohesive energy difference between WZ and ZB structures with size for passivated stoichiometric clusters. 66
- 4.11 DOS for 4 shell Cd-centred (left panels) and S-centred (right panels) ZB non-stoichiometric cluster. Upper panels correspond to unpassivated case while bottom panels correspond to passivated case. Black, red, green and blue lines correspond to total DOS, Cd-contribution, S-contribution and that of H-contribution (in case of passivated cluster only) respectively. . . 67
- 4.12 Variation of cohesive energy difference between WZ and ZB structures with size for passivated Cd-centred (left panel) and S-centred (right panel) non-stoichiometric clusters. 68
- 4.13 Calculated band gaps of the ground state structures at each shell size for stoichiometric clusters. Inset shows the positions of HOMO (solid right triangles) and LUMO (solid left triangles) with respect to HOMO of 6th shell cluster, as a function of cluster size. 69
- 4.14 Calculated band gaps of the ground state structures at each shell size for non-stoichiometric clusters. Left and right panels show the results for Cd-centred and S-centred clusters respectively. Insets show the positions of HOMO (solid right triangles) and LUMO (solid left triangles) with respect to HOMO of 6th shell cluster, as a function of cluster size. 69
- 5.1 Ground state structures of Co_n clusters for $n = 2-12$ obtained by our DFT calculation. Numbers in the parenthesis represent number of atoms in the cluster (followed by .1 indicates ground state) and total magnetic moment, respectively. 80

- 5.2 The minimum energy state and a higher energy isomer of Co_n clusters ($n = 13-20$). For $n = 14$, the hcp and icosahedral structures are almost degenerate. For $n = 13$ and 15-20, the minimum energy structure has hcp symmetry and we have shown the optimal icosahedral structure as the higher isomer. The first entry in the parenthesis gives the cluster size as well as isomeric position, second entry corresponds to total magnetic moment and the third entry in the alternate parentheses indicates the relative energy to the minimum energy state. 83
- 5.3 Plot of cohesive energy per atom (E_c) for optimal hcp and optimal icosahedral structures (left) and plot of total energy difference between these optimal structures, $E_{\text{diff}} = -[E(\text{hcp}) - E(\text{icosahedral})]$, (right) for the size range $n = 13-20$. E_{diff} increases with cluster size. 84
- 5.4 Plot of total energy as a function of magnetic moment for (a) Co_{13} , (b) Co_{15} , (c) Co_{17} and (d) Co_{19} clusters. The dot (square) represents icosahedral (hcp) structure. Insets represent magnification around the minima. 89
- 5.5 Plot of cohesive energy per atom as a function of cluster size n for the ground state structures of the entire size range $2 \leq n \leq 20$. (a) Plot of cohesive energy per atom (C.E.) as a function of $n^{-1/3}$ for the clusters Co_n , $6 \leq n \leq 20$ and a linear fit ($-3.90 n^{-1/3} + 5.00$) to the data. (b) Plot of second difference in total energy ($\Delta_2 E$), which represents the relative stability. 90
- 5.6 Plot of single channel, D_1 and dimer channel, D_2 , dissociation energies as a function of cluster size n for the GS configurations. We compare our calculated single channel dissociation with the CID experimental result in Ref. [33]. 91
- 5.7 Plot of (a) average bond length $\langle r \rangle$ and (b) average coordination $\langle n_c \rangle$, as function of cluster size n for the ground state geometries. Dots and squares represent the data points, while solid line through them is guide to eye. . . 93
- 5.8 Size dependent variation of magnetic moment of the corresponding ground states. Calculated magnetic moments of the first isomers have also been shown. Calculated magnetic moments are compared with experimental results (Ref. [11] and Ref. [10]). 94

- 5.9 Comparison of magnetic moment between optimized hcp and optimized icosahedral structures for Co_n in the size range $n = 15-20$. The filled squares and filled circles correspond to results for hcp and icosahedral structures, respectively. The insets show the corresponding comparisons for (a) average bond length and (b) average coordination number. 95
- 5.10 Plot of density of states (DOS) (with half-width = 0.1 eV) of the optimal hcp and optimal icosahedral structures of Co_{19} and Fe_{19} clusters, both in nonmagnetic phase (left panel) and magnetic phase (right panel). Energy along x -axis is with respect to Fermi energy of the corresponding system. Magnetic DOS is averaged out between majority and minority channels. 99
- 5.11 Plot of cohesive energy per atom for X_{19} [$\text{X} = \text{Mn}, \text{Fe}, \text{Co}, \text{Ni}, \text{Cu}$] in both nonmagnetic phase(left) and magnetic phase(right). The blue vertical bars correspond to hcp structure and orange bars correspond to icosahedral structure. The inset shows the trend in bulk cohesive energy for Mn, Fe, Co, Ni and Cu. 100
- 6.1 The reactivity of $\text{Co}_{n-m}\text{V}_m$ ($n > m$) clusters for reaction with H_2 . Open circles, closed circles, open squares, open triangles, and closed triangles correspond to measured values for $n = 6, 8, 10, 11$ and 13 , respectively. (adopted from Ref. [3]) 108
- 6.2 Structures of optimal hcp, icosahedron and cub-octahedron of pure Co_{13} cluster (from left to right respectively). Optimal hcp structure is the minimum energy state. 110
- 6.3 Structures of optimal icosahedron (minimum energy state), optimal cub-octahedron (2nd isomer) and hcp (4th and 5th isomers) (from left to right) for Co_{12}V cluster. Green dot represents Co atom, while yellow dot represents V-atom. Same convention is followed in next three figures. 112
- 6.4 A, B, C represent the three inequivalent *homotops* in icosahedral Co_{10}V_3 structure having one V-atom always at the centre. The three structures are the optimal structures for the three types, however, type A is the most probable. 112
- 6.5 A, B, C, D represent the four probable *homotops* in icosahedral Co_9V_4 structure having one V-atom at the centre and two other V-atoms are closest to each other on the surface, while the position of fourth V-atom is varied. The four structures represented above are the optimal structures for the respective four types. However, type A is the most probable. 113

6.6	Cohesive energy of the minimum energy structures of $\text{Co}_{13-m}\text{V}_m$ clusters with respect to the cohesive energy of optimal Co_{13} cluster. The dashed line is the reference fixed at the cohesive energy of optimal Co_{13} . Inset shows the second difference ($\Delta_2 E$) in cohesive energy [as defined in Eqn. (6.2)] for Co_{12}V , Co_{11}V_2 and Co_{10}V_3	115
6.7	Total DOS per atom (black curve), total Co DOS per atom (green curve), total V-DOS per atom (red curve) and total d-projected DOS per atom (orange curve) for the optimal structures of Co_{12}V , Co_{11}V_2 , Co_{10}V_3 and Co_9V_4 . The smearing width is fixed at 0.1 eV. Vertical line through zero is the Fermi energy.	120
6.8	Total DOS of the central V atom in the optimal structures of Co_{12}V , Co_{11}V_2 , Co_{10}V_3 and Co_9V_4 . The Fermi energy is fixed at zero.	121
6.9	The calculated minimum energy chemisorption structures with H_2 on the minimum energy structures of $\text{Co}_{13-m}\text{V}_m$ ($m = 0-4$). It is clearly seen that hollow site on the surface is preferred by chemisorbed hydrogen.	123
6.10	The calculated chemisorption energy of $\text{Co}_{13-m}\text{V}_m$	124
7.1	Recursive reduction of (a) a system of two quasi 1D semi-infinite leads plus 1D wire into (b) a system of infinite linear chain. The numbering of sites of the equivalent 1D infinite chain is shown in (b). The directions of incident wave $e^{in\theta}$ to the scattering region, the reflected wave $re^{-in\theta}$ and transmitted wave $te^{in\theta}$ from the scattering region are shown with arrows. (c) Formation of vector basis by folding the infinite chain and clubbing the two sites together.	136
7.2	Variation of recursion coefficient β with recursion steps for different cross-sectional sizes of the lead, with $t_{lead} = 2.0$ and $\epsilon_{lead} = 0.0$. The lower left inset shows the variation of converged values of β (β_c) with cross-sectional size.	138
7.3	Variation of conductance with cross-sectional sizes for an even numbered wire, $N = 4$ considering direct coupling and $ \Delta\epsilon = 0.2$. Variation in conductance is around 5% for even numbered wire. For odd numbered wire (not shown in the above plot), it is less than 1%.	140

- 7.4 Conductance as a function of the number of atoms in the wire. For given values of t_{lead} and t_{wire} , we consider three cases: (a) $|\Delta\epsilon| = 0$, (b) $|\Delta\epsilon| = 0.2$ and (c) $|\Delta\epsilon| = 0.4$. For each case, we consider three types of coupling between lead and wire : green curve for strong coupling, black for direct coupling and red curve for weak coupling. 141
- 7.5 Density of states (left panel) and total transmittance (right panel) in no charge transfer ($|\Delta\epsilon| = 0$) and direct coupling ($t_c = t_{\text{lead}}$) situation for wires of lengths $N = 1$, $N = 2$ and $N = 3$ (from top to bottom). The dashed lines label the Fermi energy. 142
- 7.6 DOS around Fermi energy for several even numbered wires in two cases - $|\Delta\epsilon| = 0$ (left) and $|\Delta\epsilon| = 0.4$ (right). For $|\Delta\epsilon| = 0.4$, DOS at E_F gradually increases with wire size. For $N = 14$, the deep at E_F for $|\Delta\epsilon| = 0$ case is replaced by a peak at E_F for $|\Delta\epsilon| = 0.4$. Lead-wire coupling was considered to be of direct type in all cases. 143
- 7.7 Plot of conductance as a function of wire size for two values of $|\Delta\epsilon|$: circles connected by solid line for $|\Delta\epsilon| = 0.6$ and squares connected by dashed line for $|\Delta\epsilon| = 0.8$. Conductances for all even numbered wires and all odd numbered wires are shown separately by red line and green line respectively within the insets. Inset (a) for $|\Delta\epsilon| = 0.6$ and inset (b) for $|\Delta\epsilon| = 0.8$. Inset (c) shows the variation of period of parity flip with $|\Delta\epsilon|$ and solid line through the right triangles is the fitted curve. 144
- 7.8 Plot of conductance as a function of wire size for two values of t_c - circles connected by solid line for $t_c = 1.1 t_{\text{lead}}$ and squares connected by dashed line for $t_c = 0.9 t_{\text{lead}}$. Conductances for all even numbered wires and all odd numbered wires are shown separately by red line and green line respectively. Left inset corresponds to $t_c = 1.1 t_{\text{lead}}$ and right one to $t_c = 0.9 t_{\text{lead}}$ 145

List of Tables

3.1	Structural parameters of ZB and WZ phases for CdX (X = S, Se, Te) series. Lattice parameters have been taken from Ref. [16] for both ZB and WZ phases of CdS, from Ref. [22] for ZB CdSe, from Ref. [23] for WZ phase of CdSe, from Ref. [19] for ZB CdTe and from Ref. [20] for WZ CdTe.	37
3.2	Total energy per formula, energy difference $\Delta E = E(ZB) - E(WZ)$ and band gaps. + ve sign of ΔE indicates WZ is more stable than ZB and vice versa. The numbers within the parenthesis in the columns of band gap, correspond to their experimental values taken from Ref. [25].	39
3.3	Covalent gap ΔE_{sp^3} , hopping term $E_h = -2h$ and ionicity f_i for the CdX series in ZB and WZ structure. $f_i(C)$ means calculated value of ionicity by Christensen <i>et al</i> from Ref. [15], $f_i(Ph)$ that of Phillips taken from Ref. [4] and $f_i(Pa)$ that of Pauling taken from Ref. [5].	41
3.4	Covalent gap ΔE_{sp^3} , hopping term $E_h = -2h$ and ionicity f_i for model CdTe in WZ structure, with $\Delta(c/a)$ and u as given in the first column.	45
3.5	Bond ionicity β for <i>CdX</i> series in both ZB and WZ structure. Previously reported values of β by Abu-Farsakh <i>et al</i> [27] for ZB structure of <i>CdS</i> and <i>CdSe</i> are also listed.	47
4.1	Number of atoms and diameters of both stoichiometric and non-stoichiometric CdS clusters listed in order of increasing shell sizes for wurtzite structure. The corresponding values for the zincblende structure are shown within parenthesis.	54
5.1	Cohesive energy, relative energy to the theoretically computed minimum energy state ($\Delta E = E - E_{\min}$) and magnetic moment for Co_n ($n = 2-14$) clusters. The entry in the first column “ <i>n.i</i> ” indicates ground state for $i = 1$ and isomers for $i > 1$ of n atoms cluster. Recent SG experimental results (Refs. [10, 11, 29, 30]) of the magnetic moment are shown for comparison.	87

5.2	Cohesive energy, relative energy to the theoretically computed minimum energy state ($\Delta E = E - E_{\min}$) and magnetic moment for Co_n ($n = 15-20$) clusters. Recent SG experimental results (Refs. [10, 11, 29, 30]) of the magnetic moment are shown for comparison.	88
5.3	Theoretically calculated single channel bond dissociation energies (BDE) compared with experimentally measured values in Ref. [33] for Co_n ($n = 2-20$). Experimental uncertainties are within parentheses.	92
5.4	Cohesive energies of the optimal hcp and optimal icosahedral structures for both Co_n and Fe_n clusters ($n = 13-20$) in the spin-polarized calculation. It is clearly seen that while Co_n clusters prefer hcp-like symmetry, Fe_n clusters favor icosahedral growth pattern. Number in the parenthesis is the total magnetic moment of the optimal structure.	96
5.5	<i>rms distortions</i> of the optimal hcp and optimal icosahedral structures for both Co_n and Fe_n clusters ($n = 13-20$) in the spin-polarized calculation. Less distorted structures appear as more stable.	97
5.6	Cohesive energies of the optimal hcp and optimal icosahedral structures for both Co_n and Fe_n clusters ($n = 13-20$) in non-magnetic calculation.	98
6.1	Our calculated cohesive energy and bond length of Co_2 , Co-V and V_2 dimers. For comparison, we have also listed the experimental values for Co_2 dimer (Ref. [12]) and V_2 dimer (Ref. [13]).	116
6.2	The average distances in Å between centre to vertex and between two nearby vertices for the minimum energy structures of all the studied clusters. For Co_{13} , the values correspond to the optimal icosahedron.	116
6.3	Positions of HOMO and LUMO in both the spin channels and the values of δ_1 and δ_2 for the optimized structures of all compositions.	118
6.4	Our theoretically calculated cohesive energy, bond length and vibrational frequency for H_2 dimer. Experimental values in Ref. [17] are also given for comparison.	119
7.1	Values of conductances for various wire lengths in absence of mirror symmetry. t_{c1} and t_{c2} are the two lead-wire couplings of the two junctions.	146

Chapter 1

Introduction

1.1 Nano-materials - a preview

The earliest observation of the change of material properties with reduced dimensionality was made by the work of Michael Faraday in 1850 [1] on colloidal gold which showed optical properties different from those of the corresponding bulk metal. Stained glass windows, dating back to medieval times, provide beautiful examples of colours which can be created by suspending small colloidal particles of copper, silver, and gold in the glass. About a hundred years later, Richard P. Feynman gave a classic talk titled “*There’s Plenty of Room at the Bottom*” at the annual meeting of the American Physical Society at the California Institute of Technology in 1959, where he explained the enormous possibilities of materials on a small scale. During the last two decades, research on materials with sizes in the nanometer regime has gained huge momentum. The impressive progress in the fabrication of low-dimensional structures has made it possible to reduce the effective dimension of materials from three dimensional bulk, to quasi-two dimensional quantum well systems, quasi-one dimensional quantum wires, and even quasi-zero dimensional quantum dots (QDOT). Several books [2]-[5] and review articles [6]-[12] have been published in the recent years on nano-materials. The interest in nano-materials arise because they constitute a new type of material which have properties different from those of the individual atoms and molecules or bulk and they are well suited for applications ranging from catalysis [13] (*e.g.* catalytic converters in automobiles and electrochemical fuel cells) to optoelectronic [14]-[16], magnetic [8] and even medical applications [17, 18]. More recently, there have been developments towards biological uses. For example, gold nano-particles studded

with short segments of DNA [19] could form the basis of an easy-to-read test to single out genetic sequences.

An important reason for the interest in nano-materials is the size-dependent evolution of their properties. This is partly because of the fact that being small objects, they have most of the constituent atoms on their surface, thereby having large surface to volume ratio. The surface energy contribution is therefore strongly size dependent and plays an important role in deciding various properties. Another reason for the marked difference in the characteristic features of nano-materials is the change in electronic properties with reduced dimensionality. To have a feel, Fig. 1.1 shows the evolution of this density of states as dimension is lowered one by one. In going from 3D bulk to 2D film, the parabolic 3D density of states is converted to a staircase structure in which the density of states for individual sub-bands is constant in energy. For a quasi-1D rectangular quantum wire, the density of states shows divergences at specific energies, which may lead to interesting effects in their transport properties. Density of states of a quantum dot is, on the other hand, is completely discrete.

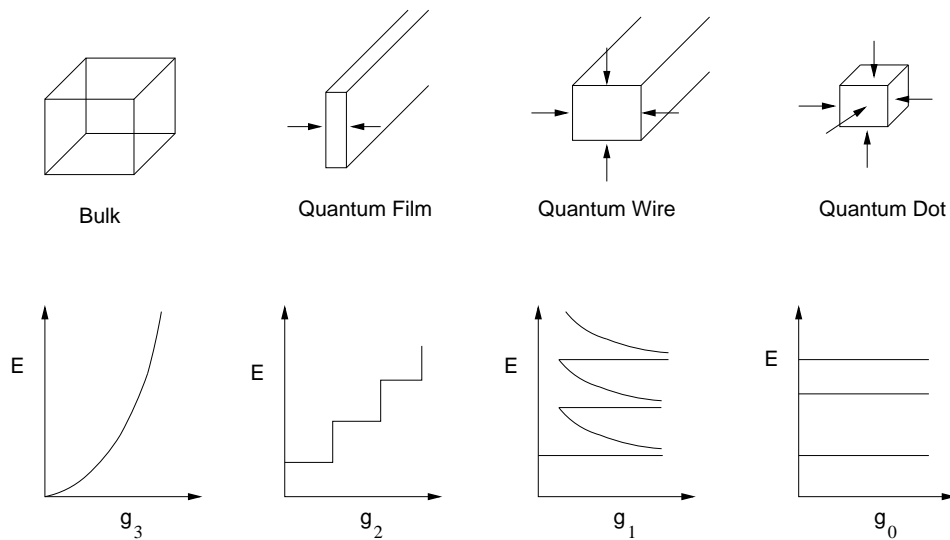


Figure 1.1: Evolution of the density of states (g 's) with dimensionality showing the variation of density of states with energy for bulk solid, quantum film, quantum wire and quantum dot. (Taken from Ref. [20])

With the present advance in technology, it is now possible to produce and to measure most of the properties of the nano-materials. However, the crucial point is to understand their behaviour, for they are much more complex than the bulk. Theoretical investigations therefore play a vital role in understanding material properties in this new field of science. Indeed, investigations of properties of finite material aggregates and studies with the aim at gaining deep insights into the development of material characteristics from the molecular regimes to the bulk phase, are major themes of current interdisciplinary basic and applied research endeavours. To this day, the fact that experiments and theory proceed hand in hand is a hallmark of the work in this field. Not everything that we imagine, analyze or compute can be measured and many observations still provide significant challenge for their interpretation.

Clusters are one type of nano-materials belonging to the general class of QDOT and are made up of atoms or molecules, ranging from a dimer to several thousands of atoms. They may consist of identical atoms or molecules or two or more different species. They can be classified as *small* clusters or *large* clusters depending upon the number of constituent atoms and molecules. For *small* clusters, physical properties change abruptly as we change their size. On the other hand, if the properties vary relatively smoothly with the number of constituent atoms and molecules, nevertheless showing significant finite size effects, then these clusters are classified as *large* clusters. In this thesis, we have theoretically investigated the electronic properties of semiconductor nano-clusters generally belonging to the class of *large* clusters, as well as *3d* transition metal clusters which generally belong to the class of *small* clusters.

We have studied the structural stability of semiconductor nano-clusters, considering the effect of size, stoichiometry and passivation. To understand this in the context of the bulk scenario, we have also revisited the structural stability in bulk phase of binary octet semiconductors. In the bulk, most of the II-VI and III-V semiconductors have either the cubic zincblende or hexagonal wurtzite structure at ambient temperature and pressure. The structural differences between these two phases is very subtle.

For transition metal clusters, we have dealt with *small* clusters and have studied the evolution of structure and magnetic properties with the increase of cluster size by one-by-one atom addition. We have studied both mono-atomic as well as di-atomic transition

metal clusters.

Besides nano-clusters, we have also studied the electrical transport properties of atomic sized conductors like a mono-atomic wire connected to semi-infinite leads. The important point about this study is that we have, for the first time, implemented the block-recursion approach [21]-[23] to calculate electrical conductance for such systems.

In the following three sections, we explain our motivation behind studying these three classes of problems in particular. The final section contains the outline of the thesis.

1.2 Bulk and nano-crystalline semiconductors

Because of their potential application in optoelectronic devices, semiconductor materials have been the subject of intensive experimental and theoretical research. An important issue in tetrahedrally coordinated bulk semiconductors of the $A^N B^{8-N}$ type is that their structure belongs either to the cubic zincblende (ZB) or the hexagonal wurtzite (WZ) at ambient temperature and pressure. Depending on the details of growth parameters, a number of these binary semiconductors like SiC, CdS, CdSe, ZnS, CuCl and CuBr can be prepared at ambient pressure in either form [24]. This is known as WZ-ZB polytypism. Thermodynamical analysis by Jagodzinski [25] demands that a necessary condition for polytypism is a low temperature cubic phase with WZ-like phases at elevated temperatures. The experimentally stable crystal structure at low temperature for several binary octet compounds are given in Fig. 1.2. A large number of theoretical investigations [26]-[29] have been devoted to the systematization of polytypism in bulk binary octet semiconductors and the qualitative conclusion coming out of all these works is that more ionic compounds favour WZ structure, while more covalent compounds favour ZB phase.

While structural stability in the bulk phase has been well studied, speculations began during the last decade about *what happens to structural stability in nano regime* ? In semiconductor nano-clusters, size effect is observable when the particle diameter is almost equal to or smaller than the Bohr diameter of excitons in the corresponding bulk material. This can be observed as a blue shift in the optical band gap with decreasing particle size [30, 31] (therefore, one can produce white CdS instead of orange bulk CdS and yellow-brown PbS instead of black bulk PbS). Being finite objects, clusters are expected to have

II-VI					III-V				
	O	S	Se	Te		N	P	As	Sb
Be	WZ	ZB	ZB	ZB	B	Graphite	ZB	ZB	****
Mg	NaCl	NaCl	NaCl	WZ	Al	WZ	ZB	ZB	ZB
Ca	NaCl	NaCl	NaCl	NaCl	Ga	WZ	ZB	ZB	ZB
Zn	WZ	ZB	ZB	ZB	In	WZ	ZB	ZB	ZB
Cd	NaCl	WZ	ZB	ZB					
Hg	Cinb	Cinb	ZB	ZB					

Figure 1.2: The experimentally stable crystal structures of octet AB compounds, WZ = wurtzite, ZB = zincblende, Cinb. = cinnabar, **** means that the compound does not exist. (Table adapted from Ref. [29])

noncrystalline structures. However, it is also possible to build up crystalline clusters, which have bulk-like core regions and modified surfaces. An important issue in cluster science is to understand whether crystalline or noncrystalline structures prevail for a given size and composition. One problem with studying bare clusters is that they could be difficult to isolate and handle on a preparative scale like conventional molecules. To enable the investigation of approximately uniformly sized clusters and exploit cluster properties in device applications, it is necessary to protect (“passivate”) them with a ligand shell as this avoids coalescence at high cluster densities. Determination of crystalline structure of nano-clusters is, therefore, a complex issue, as the stable phase depends on several parameters, like size, shape, stoichiometry, type of passivator used etc. Methods have recently been developed to prepare highly crystalline, mono-disperse nano-crystals of semiconductors in the condensed phase [32]-[41]. However, theoretical studies [42]-[44] have been devoted so far only to account for band gap variation with cluster size, not the structural stability issue in a systematic manner. One of our main concern in this thesis is, therefore, the structural stability issue of semiconductor nano-clusters.

1.3 Transition metal small clusters

The interesting fact about clusters is that their properties are not only size dependent, even the addition or subtraction of a single atom can change cluster properties drastically if the cluster size is sufficiently small. It is therefore important to study the evolution of cluster properties as it is built up atom by atom. Geometrical structure of clusters is a crucial ingredient in any attempt of interpreting any experimental measurement of electronic properties. However, these small clusters are produced in gas phase and unfortunately there is no direct means in experiments to get information about geometrical structure. The reactivity toward certain molecules provides an indirect way to determine the structure since the number of molecules adsorbed on the cluster surface gives information on the number of available adsorption sites and consequently on the shape of the cluster. A difficulty in this context is the extent of modification of the original free cluster structure by the adsorbed molecules. Evidently the kind of adsorbed molecules should be such as to leave the geometry of the cluster unaffected. First principles methods can, therefore, play a vital role in determining the ground state cluster geometry. On top of ground state, it is also possible to have many stable local structures for a particular sized cluster within very small energy window. These are called ‘isomers’ whose number increase very rapidly with the number of atoms constituting the clusters.

Transition metal clusters are of special interest in the context of *small* clusters, as the free atoms of the transition metals have an incomplete *d*-shell in the ground state and these localized *d*-electrons dominate most of their properties, in contrast to clusters or solids of simple *sp*-metals whose properties are dominated by the delocalized behaviour of the external *sp* electrons. Because of the incomplete *d*-shell, most of the transition metal clusters possess finite magnetic moment. In fact, magnetism of transition metal (TM) clusters constitutes one of the fundamental challenges, since atomic and bulk behaviours are intrinsically different. Atomic magnetism is due to electrons that occupy localized orbitals (it is well known that in isolated atoms almost all elements show a non-vanishing magnetic moment given by Hund’s rules), while in TM solids the electrons responsible for magnetism are itinerant, *e.g.* conducting *d*-electrons. Consequently, the magnetic properties of nano particles are very sensitive to size, composition and local atomic en-

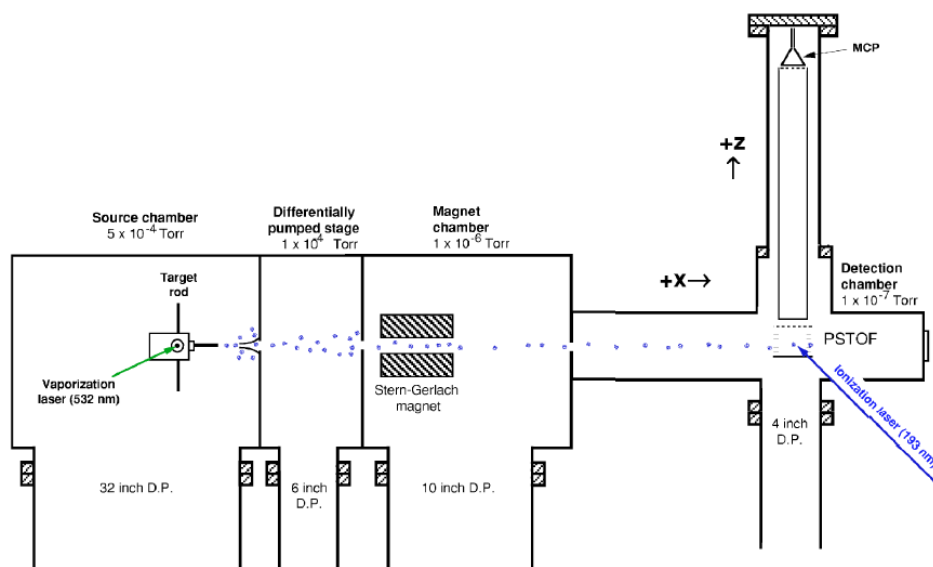


Figure 1.3: Schematic diagram of the Stern-Gerlach cluster beam experiment (adapted from Ref. [45])

vironment thus showing a wide variety of intriguing phenomena. There have been many experimental studies [10], [45]-[49] of the magnetism of free transition-metal clusters in molecular beams which use Stern-Gerlach (SG) type deflection experiments. A schematic diagram of the experimental setup is shown in Fig. 1.3.

Metal clusters are produced in a laser vaporization cluster source, leave the source in a supersonic expansion of helium gas and form a cluster beam. The cluster beam passes through a series of collimating slits and a rotating beam chopper before entering the gradient field magnet. While passing through gradient magnet, the free magnetic clusters interact with the applied inhomogeneous magnetic field and are deflected from the original beam trajectory. The deflection experiments are normally analyzed assuming that the free ferromagnetic clusters are single-domain particles following the super-paramagnetic behaviour, which is true under certain experimental conditions, namely, when the thermal relaxation time of the clusters is much lower than the time required by the clusters to pass through the poles of the Stern-Gerlach magnet. As the deflection is proportional to the cluster magnetization M , magnetization is therefore computed from the magnitude of beam deflection. The intrinsic cluster magnetic moment μ is in turn calculated from

M assuming Curie law behaviour. The validity of applying this thermodynamic-based analysis to molecular beam deflection experiments has been discussed in detail elsewhere [48, 49].

While investigations on pure or mono-atomic transition metal clusters yield insight into the basic mechanisms, alloy or multi-atomic clusters seem to be more promising in terms of technical application since they offer the possibility to adjust the properties by varying the composition and atomic ordering in addition to the size of the cluster. Surface structures, compositions and segregation properties [50, 51] of alloy clusters are of interest as they are important in determining chemical reactivity and especially catalytic activity [52]. Another interesting property of alloy clusters is that their structures may be quite different from the structures of the pure clusters of the same size and they may display properties which are distinct from the corresponding bulk alloys due to finite size effect. For example, iron and silver are immiscible in the bulk, but readily mix in finite clusters [53]. One major part of this thesis has been devoted to study the structures, energetic, magnetism and chemical reactivity of $3d$ transition metal clusters and their alloys in small sizes.

1.4 Atomic sized conductors

The common knowledge about the electrical properties of a piece of any metal becomes invalid, as soon as its size approaches the atomic scale. The familiar Ohm's law, from which we learn that the resistance of a conductor scales proportional to its length, breaks down. The reason is that the distance an electron travels between two scattering events is typically much larger than the atomic size. The electrons, therefore, traverse an atomic-sized conductors ballistically, and the resistance becomes independent of its length. At this length scale quantum effects such as conductance quantization, interference of electron waves, Anderson localization, Coulomb blockade, and Kondo effects become dominant. In fact, when the size of the conductor becomes of the order of or less than the inelastic scattering length, the character of the resistance changes and it is necessary to invoke the wave nature of the electrons in the conductor for a proper description. Experiments on molecular junctions are far from trivial. The main difficulty in experimental mea-

surement comes from the extreme sensitivity of the junction's electrical properties to the detailed atomic arrangement of the contacts, which is beyond experimental control. This is particularly pronounced at the nano-scale, where the electrons often travel phase coherently through the junction. This means that interference effects are directly observable in macroscopic quantities, such as conductance. One example of experimental measurement of conductance at the gold contact is shown in Fig. 1.4, which gives a clear evidence of conductance quantization.

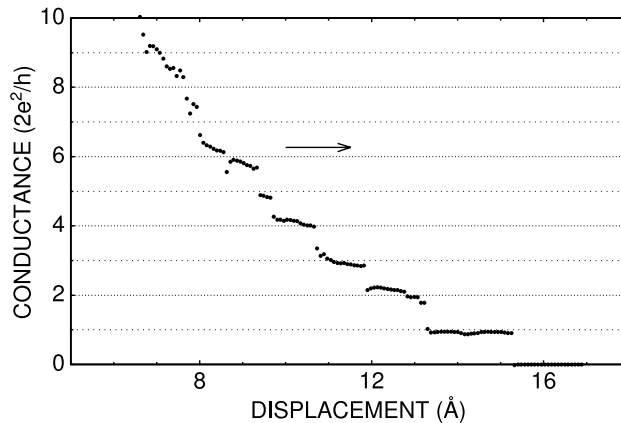


Figure 1.4: Quantized conductance curve for a gold contact measured at room temperature in UHV by pressing an STM tip into a clean gold surface and recording the conductance while retracing the tip. (Adopted from Ref. [54]). The direction of tip motion is given by arrow.

The above discussion demonstrates that theoretical study is very demanding in order to understand not only the quantum nature of electrons, but also the atomistic details of the junctions. Landauer first formulated a quantum mechanical approach to study transport property of atomic sized conductors and related the conductance G to the total transmission probability of the electrons at the Fermi energy $T(E_F)$ in the linear response regime as,

$$G = \frac{2e^2}{h} T(E_F) \quad (1.1)$$

In this thesis, we have introduced a method to calculate the transmission function and to study the effect of contact on the conductance of atomic chain.

1.5 Outline of the thesis

The outline of the thesis is as follows:

- (i) Chapter 2 introduces and discusses in some detail the theoretical frameworks to carry out electronic structure calculations in this thesis.
- (ii) For semiconductor clusters, we are mainly concerned about their structural stability between ZB and WZ phases at ambient pressure. For this purpose, we have first attempted to understand the relative stability in bulk phase for CdS, CdSe and CdTe in Chapter 3 in terms of constructed Wannier functions.
- (iii) Moving to nano-clusters, we have considered CdS in particular. Our choice is primarily motivated by experimental controversies (cf. section 4.1 of chapter 4) concerning the structural stability of medium sized CdS nano-clusters. We have dealt with this problem in chapter 4.
- (iv) Two recent experiments [46, 47] of magnetic moment measurement of smaller sized cobalt clusters motivated us to study the interplay of structure and magnetism in pure Co_n clusters ($n \leq 20$), which is the subject matter of chapter 5. The structural growth of these clusters have been compared with other $3d$ late transition metal clusters.
- (v) Chapter 6 provides an account of our study on $\text{Co}_{13-m}\text{V}_m$ ($m = 1-4$) alloy clusters which are reported to show anomalous variation in reactivity with hydrogen [55]. Here we have investigated the influence of V doping in Co_{13} cluster on structure, energetics and chemical reactivity using *ab-initio* calculations.
- (vi) Finally, chapter 7 presents our method of conductance calculation of atomic sized conductor and discusses the influence of nano-contacts.

Bibliography

- [1] Michael Faraday, *M. Philos. Trans. R. Soc.*, London, **147**, 145, 1857.
- [2] *Clusters of Atoms and Molecules*; Ed. H. Haberland; Springer: Berlin, 1994; Vols. I and II.
- [3] *Theory of Atomic and Molecular Clusters*; Ed. J. Jellinek; Springer: Berlin, 1999.
- [4] R. L. Johnston, *Atomic and Molecular Clusters*; Taylor and Francis: London, 2002.
- [5] *Encyclopedia of Nanoscience and Nanotechnology*, American Scientific Publishers, 2004.
- [6] R. Ferrando, J. Jellinek, and R. L. Johnston, *Chem. Rev.* **108**, 845 (2008).
- [7] F. Baletto, and R. Ferrando, *Rev. Mod. Phys.* **77**, 371 (2005).
- [8] J. Bansmann, S. H. Baker, C. Binns, J. A. Blackman, J. -P. Bucher, J. Dorantes-Davila, V. Dupuis, L. Favre, D. Kechrakos, A. Kleibert, K. -H. Meiwes-Broer, G. M. Pastor, A. Perez, O. Toulemonde, K. N. Trohidou, J. Tuaille, and Y. Xie, *Surf. Sci. Rep.* **56**, 189 (2005).
- [9] J. A. Alonso, *Chem. Rev.* **100**, 637 (2000).
- [10] W. A. de Heer, *Rev. Mod. Phys.* **65**, 611 (1993).
- [11] M. D. Morse, *Chem. Rev.* **86**, 1049 (1986).
- [12] J. Koustecky, and P. Fantucci, *Chem. Rev.* **86**, 539 (1986).
- [13] C. R. Henry, *Surf. Sci. Rep.* **31**, 235 (1998).

- [14] J. Nanda, K. S. Narayan, B. A. Kuruvilla, G. L. Murthy, and D. D. Sarma, *Appl. Phys. Lett.* **72**, 1335 (1998).
- [15] P. Gomez-Romero, *Adv. Matter.* **13**, 163 (2001).
- [16] R. Elghanian, J. J. Storhoff, R. C. Mucic, R. L. Letsinger, and C. A. Mirkin, *Science* **277**, 1078 (1997).
- [17] P. Alivisatos, *Nat. Biotechnol.* **22**, 47 (2004).
- [18] N. L. Rosi, C. A. Mirkin, *Chem. Rev.* **105**, 1547 (2005).
- [19] C. A. Mirkin, R. L. Letsinger, R. C. Mucic, and J. J. Sstorhoff, *Nature (London)* **382**, 607 (1996).
- [20] J. Nanda, Ph.D Thesis, Indian Institute of Science, Bangalore (2000).
- [21] R. Haydock, V. Heine, M. J. Kelly, *J. Phys. C :Solid State Phys* **5**, 2845 (1972).
- [22] R. Haydock, *Solid State Physics*, editor: H. Ehrenreich, F. Sietz, D. Turnbull (Academic, New York, 1980) volume 35.
- [23] T. J. Godin, R. Haydock, *Phys. Rev. B* **38**, 5237 (1988).
- [24] *ibid.* Vols. 17a and 17b.
- [25] H. Jagodzinski, *Neues Jahrb. Mineral.* **10**, 49 (1954); H. Jagodzinski and H. Arnold, Proceedings of the Conference on Silicon Carbide, Boston, 1959 (Pergamon, New York, 1960), p. 141.
- [26] P. Lawaetz, *Phys. Rev. B* **5**, 4039(1972).
- [27] N. E. Christensen, S. Satpathy and Z. Pawlowska, *Phys. Rev. B* **36**, 1032(1987).
- [28] C.-Y. Yeh, Z. W. Lu, S. Froyen and A. Zunger, *Phys. Rev. B* **45**, 12130(1992).
- [29] C.-Y. Yeh, Z. W. Lu, S. Froyen and A. Zunger, *Phys. Rev. B* **46**, 10086(1992).
- [30] L. E. Brus, *J. Chem. Phys.* **80**, 4403 (1984).

- [31] Y. Wang, N. Herron, *J. Phys. Chem.* **95**, 523 (1991).
- [32] T. Vossmeier, L. Katsikas, M. Giersig, I. G. Popovic, K. Diesner, A. Chemseddine, A. Eychmuller, and H. Weller, *J. Phys. Chem.* **98**, 7665 (1994).
- [33] Y. Wang, and N. Herron, *Phys. Rev. B* **42**, 7253 (1990).
- [34] T. Torimoto, H. Kontani, Y. Shibusaki, S. Kuwabata, T. Sakata, H. Mori, and H. Yoneyama, *J. Phys. Chem. B* **105**, 6838 (2001).
- [35] J. Nanda, B. A. Kuruvilla, and D. D. Sarma, *Phys. Rev. B* **59**, 7473 (1999).
- [36] B. O. Dabbousi, C. B. Murray, M. F. Rubner, and M. G. Bawendi, *Chem. Mater.* **6**, 216 (1994).
- [37] A. L. Rogach, A. Kornowski, M. Gao, A. Eychmuller, and H. Weller, *J. Phys. Chem. B* **103**, 3065 (1999).
- [38] S. Gorer, and G. Hodes, *J. Phys. Chem.* **98**, 5338 (1994).
- [39] Y. Mastai, and G. Hodes, *J. Phys. Chem. B* **101**, 2685 (1997).
- [40] Y. Masumoto, and K. Sonobe, *Phys. Rev. B* **56**, 9734 (1997).
- [41] H. Arizpe-Chrez, R. Ramirez-Bon, F. J. Espinoza-Betrun, O. Zelaya-Angel, J. L. Marn, and R. Riera, *J. Phys. Chem. Solids.* **61**, 511 (2000).
- [42] P. E. Lippens and M. Lannoo, *Matter. Sci. Eng.* **B9**, 485 (1991).
- [43] R. Viswanatha, S. Sapra, T. Saha-Dasgupta, and D. D. Sarma, *Phys. Rev. B* **72**, 045333 (2005) and references therein.
- [44] S. Sapra, and D. D. Sarma, *Phys. Rev. B* **69**, 125304 (2004).
- [45] M. B. Knickelbein, *Phys. Rev. B* **70**, 014424 (2004).
- [46] X. Xu, S. Yin, R. Moro and W. A. de Heer, *Phys. Rev. Lett.* **95**, 237209 (2005).
- [47] M. B. Knickelbein, *J. Chem. Phys.* **125**, 044308 (2006).

- [48] D. C. Douglass, A. J. Cox, J. P. Bucher and L. A. Bloomfield, *Phys. Rev. B* **47**, 12874 (1993).
- [49] M. B. Knickelbein, *J. Chem. Phys.* **121**, 5281 (2004).
- [50] A. V. Ruban, H. A. Skriver, J. K. Nørskov, *Phys. Rev. B* **59**, 15990 (1999).
- [51] G. Bozzolo, J. Ferrante, R. D. Noebe, B. Good, F. S. Honey, P. Abel, *Comput. Matter. Sci.* **15**, 169 (1999)
- [52] A. M. Molenbroek, S. Haukka, B. S. Clausen, *J. Phys. Chem. B* **102**, 10680 (1998).
- [53] M. P. Andrews, S. C. O'Brien, *J. Phys. Chem* **96**, 8233 (1992).
- [54] M. Brandbyge, J. Schiøtz, P. Stoltze, K. W. Jacobsen, J. K. Nørskov, L. Olesen, E. Lægsgaard, I. Stensgaard, F. Besenbacher, Quintized conductance in atomic-sized wires between two metals, *Phys. Rev. B* **52**, 8499 (1995).
- [55] S. Nonose, Y. Sone, K. Onodera, S. Sudo and K. Kaya, *J. Phys. Chem.* **94**, 2744 (1990).

Chapter 2

Theoretical background of electronic structure calculation

2.1 The many-body Hamiltonian

Atoms, molecules, clusters or solids, composed of ion cores and valence electrons, are described by a many-body Schrödinger equation of the form $H\Psi(\mathbf{R}, \mathbf{r}) = E\Psi(\mathbf{R}, \mathbf{r})$ with

$$H = -\sum_i \frac{\hbar^2}{2m_e} \nabla_{\mathbf{r}_i}^2 - \sum_I \frac{\hbar^2}{2M_I} \nabla_{\mathbf{R}_I}^2 - \sum_{i,I} \frac{Z_I e^2}{|\mathbf{R}_I - \mathbf{r}_i|} + \sum_{i>j} \frac{e^2}{|\mathbf{r}_i - \mathbf{r}_j|} + \sum_{I>J} \frac{Z_I Z_J e^2}{|\mathbf{R}_I - \mathbf{R}_J|} \quad (2.1)$$

where $\mathbf{R} = \{\mathbf{R}_I\}$ and $\mathbf{r} = \{\mathbf{r}_i\}$ are the ionic and electronic coordinates respectively (for simplicity we refer ion cores as ions and valence electrons as electrons). This is a complex problem to solve because it deals with a large number of interacting ions and electrons which have very different masses. The first step towards the simplification of the above equation is the *Born-Oppenheimer (B-O) approximation* (1927) [1] : since ions are much heavier than electrons [$(m_e/M_I) \sim (1/1836)$ for H atom], they move much slower compared to electrons and the electrons respond instantaneously to any ionic motion. In essence the electronic and the ionic degrees of freedom can be decoupled and the electronic properties can be calculated by assuming that the ions are fixed to a particular configuration. Following this approximation, the kinetic energy of ions can be neglected and the ion-ion interaction [last term in Eqn. (2.1)] is assumed to be constant. The constant term is called Madelung energy and is calculated classically. So under B-O approximation, the many-body Hamiltonian for a system of N interacting electrons moving

in the field of fixed ion cores, takes the form

$$H = - \sum_i \frac{\hbar^2}{2m_e} \nabla_{r_i}^2 - \sum_{i,I} \frac{Z_I e^2}{|\mathbf{R}_I - \mathbf{r}_i|} + \sum_{i>j} \frac{e^2}{|\mathbf{r}_i - \mathbf{r}_j|} \quad (2.2)$$

2.2 Single-particle approximation

Even with this simplification, it represents a very complicated many-electron eigen value problem and further approximation is needed to solve it. Efforts have been put, therefore, to develop an *effective single-particle picture*, in which the system of interacting electrons can be mapped into a system of non-interacting quantum mechanical particles that approximates the behaviour of original system. Two distinct approaches have been put forward in this direction: *wave function approach* and *density functional theory*.

2.2.1 Wave function approach

Hartree (1928) first expressed the many-body wave function as a product of single-electron functions $\{\phi_i(\mathbf{r}_i)\}$ as $\psi^H(\mathbf{r}_1, \mathbf{r}_2, \dots, \mathbf{r}_N) = \phi_1(\mathbf{r}_1)\phi_2(\mathbf{r}_2) \dots \phi_N(\mathbf{r}_N)$ and solved, numerically, the equation for each electron moving in a central potential due to other electrons and the nucleus [2]. This simplest approximation can only take into account the electron-electron Coulomb repulsion in a mean-field way, neglecting the exchange and correlation properties completely. The next level of sophistication was then introduced by Fock (1930) [3], incorporating the antisymmetric character of electronic wave function in terms of Slater determinant [4]

$$\psi^{HF} = \frac{1}{\sqrt{N!}} \begin{vmatrix} \phi_1(\mathbf{r}_1) & \phi_1(\mathbf{r}_2) & \dots & \phi_1(\mathbf{r}_N) \\ \phi_2(\mathbf{r}_1) & \phi_2(\mathbf{r}_2) & \dots & \phi_2(\mathbf{r}_N) \\ \vdots & \vdots & & \vdots \\ \phi_N(\mathbf{r}_1) & \phi_N(\mathbf{r}_2) & \dots & \phi_N(\mathbf{r}_N) \end{vmatrix}, \quad (2.3)$$

Application of the variational principle shows that such one-electron wave functions satisfy the Hartree-Fock (H-F) equations like

$$\left[-\frac{\hbar^2}{2m_e} \nabla_{r_i}^2 + V_{ion}(\mathbf{r}_i) + V_i^H(\mathbf{r}_i) + V_i^X \right] \phi_i(\mathbf{r}_i) = \epsilon_i \phi_i(\mathbf{r}_i) \quad (2.4)$$

with

$$V_i^H(\mathbf{r}_i) = e^2 \sum_j^{occ} \int \frac{|\phi_j(\mathbf{r}_j)|^2}{|\mathbf{r}_i - \mathbf{r}_j|} d\mathbf{r}_j \quad (2.5)$$

as the Hartree potential and the non-local exchange potential is given by

$$V_i^X \phi_i(\mathbf{r}_i) = - \sum_j^{occ} \phi_j(\mathbf{r}_i) \int \phi_j^*(\mathbf{r}_j) \frac{e^2}{|\mathbf{r}_i - \mathbf{r}_j|} \phi_i(\mathbf{r}_j) d\mathbf{r}_j \quad (2.6)$$

The effective Hartree potential as given by Eqn. (2.5) includes an unrestricted sum over all electrons (denoted by index j), thereby includes an unphysical self term and the Hartree potential becomes orbital independent, while Hartree potential defined by Hartree himself subtracts this self-term and it is orbital dependent. However, this unphysical term in H-F theory, has no effect as it is canceled by a same term in exchange potential. The exchange term V_i^X describes the effects of exchange between electrons. In agreement with the variational principle, the Hartree-Fock energy E_0^{HF} is higher than the exact ground state energy E_0^{exact} of the many body system and the difference $E_0^{exact} - E_0^{HF}$ is called the correlation energy. In spite of the importance and achievements of the Hartree-Fock approximation, corrections beyond it are often considered due to the fact that a single determinantal state, even with the best possible orbitals, remains in general a rather poor representation of the complicated ground state wave function of a many-body system. Therefore, methods like configuration interaction (CI) approach have been developed by quantum chemists, which consider a linear combination of different determinantal states to improve the situation. However, such approach becomes quickly computationally prohibitive as the system size grows.

2.2.2 Density functional theory

In density functional theory (DFT) [5, 6] one ignores the precise details of the many-body wave function $\psi(\mathbf{r}_1, \mathbf{r}_2, \dots, \mathbf{r}_N)$ and takes the density of electrons in the system $\rho(\mathbf{r}) = N \int \psi^*(\mathbf{r}, \mathbf{r}_2, \dots, \mathbf{r}_N) \psi(\mathbf{r}, \mathbf{r}_2, \dots, \mathbf{r}_N) d\mathbf{r}_2 d\mathbf{r}_3 \dots d\mathbf{r}_N$ as the basic variable. This is a huge simplification, since the many-body wave functions need not to be explicitly specified, as is in case of Hartree and Hartree-Fock approximations. Thus, instead of starting with a drastic approximation for the behaviour of the system, one can develop the approximate single-particle equations in an exact manner, and then introduce approximations as needed.

Also it gives huge simplification by replacing the complex object like wave-function which depends on the positions of all the N electrons by electron density which depends only on single position.

Basic theorems of DFT and Kohn-Sham equation

Density functional theorem can be expressed in terms of two basic theorems:

Theorem I: For a system of interacting particles in an external potential $V_{ext}(\mathbf{r})$, the potential $V_{ext}(\mathbf{r})$ is determined uniquely, up to an additive constant, by the ground state density. This defines a one-to-one correspondence between an external potential $V_{ext}(\mathbf{r})$ and the density $\rho(\mathbf{r})$. Since external potential determines the wave function, the wave function must be a unique functional of density. Therefore, for a given ground state density, all properties of the system are completely determined.

Theorem II: If T represents the kinetic energy and U the electron-electron interaction, then the expression, $F[\rho(\mathbf{r})] = \langle \psi | T + U | \psi \rangle$ must be a universal functional of the density, since the kinetic energy and the interaction energy are functional of density only. From this considerations, we conclude that the total energy of the system is a functional of the density and is given by,

$$E_v[\rho(\mathbf{r})] = \langle \psi | \mathcal{H} | \psi \rangle = F[\rho(\mathbf{r})] + \int V_{ext}(\mathbf{r})\rho(\mathbf{r})d\mathbf{r} \quad (2.7)$$

The Hohenberg-Kohn variational theorem states that if the functional $E_v[\rho(\mathbf{r})]$ is varied with respect to $\rho(\mathbf{r})$, then $E_v[\rho_0(\mathbf{r})]$ takes the lowest value, corresponding to the ground state, with the correct ground state density $\rho_0(\mathbf{r})$, *i.e.* $E_v[\rho_0] \leq E_v[\rho]$.

Now to reduce the expression (2.7) to a single particle equation, one can write the universal functional as

$$F[\rho] = T_S[\rho] + \frac{e^2}{2} \int \frac{\rho(\mathbf{r})\rho(\mathbf{r}')}{|\mathbf{r} - \mathbf{r}'|} d\mathbf{r}d\mathbf{r}' + E_{xc}[\rho(\mathbf{r})] \quad (2.8)$$

where $T_S[\rho]$ is the kinetic energy of the non-interacting electrons with density $\rho(\mathbf{r})$, second term is the classical mean-field inter-electron Coulomb (Hartree) energy $E_{Coulomb}$, which we separate out from the electron-electron interaction term in F and the third term E_{xc} ($= \langle T \rangle - T_S[\rho] + \langle U \rangle - E_{Coulomb}$) is the non-classical many-body exchange-correlation energy

functional. Therefore the ground-state energy functional in the Kohn-Sham approach is

$$E_{KS}[\rho] = T_S[\rho] + \int V_{ext}(\mathbf{r})\rho(\mathbf{r})d\mathbf{r} + \frac{e^2}{2} \int \frac{\rho(\mathbf{r})\rho(\mathbf{r}')}{|\mathbf{r} - \mathbf{r}'|} d\mathbf{r}d\mathbf{r}' + E_{xc}[\rho(\mathbf{r})] \quad (2.9)$$

There are three major problems in evaluating the functional $E_{KS}[\rho]$: (i) one needs a method of self-consistently evaluating the correct ground state charge density $\rho(\mathbf{r})$, (ii) evaluation of $T_S[\rho]$ given only $\rho(\mathbf{r})$ cannot be done straightforwardly as there is no information on wave functions, and (iii) the functional $E_{xc}[\rho]$ remains unknown and must therefore be represented in some simple and sufficiently accurate form.

These difficulties were resolved by Kohn and Sham (1965). The minimization of E_{KS} is carried out subject to the constraint of normalized density $\int \rho(\mathbf{r})d\mathbf{r} = N$. Application of the variational principle of the Kohn-Sham theory requires that for the ground state

$$\frac{\delta}{\delta\rho(\mathbf{r})} \{E_{KS}[\rho] - \mu N\} = 0 \quad (2.10)$$

μ is the Lagrange multiplier. Using Eqn. (2.9), one gets,

$$\frac{\delta T_S[\rho]}{\delta\rho(\mathbf{r})} + V_{KS}(\mathbf{r}) = \mu \quad (2.11)$$

where

$$V_{KS}(\mathbf{r}) = V_{ext}(\mathbf{r}) + V_H(\mathbf{r}) + V_{xc}(\mathbf{r}) = V_{ext}(\mathbf{r}) + \int \frac{\rho(\mathbf{r}')}{|\mathbf{r} - \mathbf{r}'|} d\mathbf{r}' + \frac{\delta E_{xc}}{\delta\rho(\mathbf{r})} \quad (2.12)$$

Kohn and Sham showed that solving Eqn. (2.11) is equivalent to solving the following set of single-particle Schrödinger-like equations for the variational wave-functions of fictitious non-interacting electrons

$$\left[-\frac{\hbar^2}{2m_e} \nabla^2 + V_{KS}(\mathbf{r}) \right] \phi_i = \epsilon_i \phi_i \quad (2.13)$$

where ϕ_i and ϵ_i are the single-particle wave-functions and eigenvalues, respectively, such that $\rho(\mathbf{r}) = \sum_i |\phi_i(\mathbf{r})|^2$. The Eqn. (2.13), therefore, represents the set of Kohn-Sham self-consistent field equations.

The first two difficulties outlined above are now resolved. Firstly, the ground-state electronic charge density is obtained through the self-consistent solution of Eqn. (2.13). Secondly, once the self-consistency is reached, $T_S[\rho]$ is calculated as

$$T_S[\rho] = \sum_i \langle \phi_i | -\frac{\hbar^2}{2m_e} \nabla^2 | \phi_i \rangle = \sum_i \epsilon_i - \int V_{KS}[\rho]\rho(\mathbf{r})d\mathbf{r} \quad (2.14)$$

Exchange-correlation functional

As mentioned earlier, the third difficulty with the application of DFT is that the exact form of $E_{xc}[\rho]$ is unknown and it's a great challenge in DFT. It is to be noted that this exchange-correlation energy contains — (i) kinetic correlation energy, which is the difference in the kinetic energy functional between the real and the non-interacting system, (ii) the exchange energy, which arises from the requirement of antisymmetric nature of fermions, (iii) Coulombic correlation energy, which arises from the inter-electronic repulsion and (iv) a self-interaction correction.

Two levels of approximations have been suggested to estimate $E_{xc}[\rho]$: local density approximation (LDA) and generalized gradient approximation (GGA). They are very successful in predicting most of the material properties and below we discuss them briefly.

The local density approximation (LDA)

In this approximation it is assumed that the electronic charge density in the system corresponds to that of a homogeneous electron gas and the functional $E_{xc}[\rho]$ is approximated as

$$E_{xc}^{LDA}[\rho(\mathbf{r})] = \int \rho(\mathbf{r})\mathcal{E}_{xc}[\rho(\mathbf{r})]d\mathbf{r}, \quad (2.15)$$

where $\mathcal{E}_{xc}[\rho]$ is the exchange plus correlation energy per electron in a homogeneous electron gas with electron density $\rho(\mathbf{r})$. The functional derivative of E_{xc}^{LDA} gives the exchange-correlation potential within LDA,

$$V_{xc}^{LDA} = \frac{\delta E_{xc}^{LDA}}{\delta \rho} = \mathcal{E}_{xc}[\rho(\mathbf{r})] + \rho(\mathbf{r})\frac{\partial \mathcal{E}_{xc}[\rho]}{\partial \rho}. \quad (2.16)$$

The contribution of exchange to the total energy is $\mathcal{E}_x^{LDA}[\rho(\mathbf{r})] = -\frac{3}{4}e^2 \left(\frac{3}{\pi}\right)^{1/3} [\rho(\mathbf{r})]^{1/3}$ (one can obtain this general form of exchange part starting from the solution of a uniform system [7]). For the correlation part, a number of expressions have been given. In all these expressions, the exchange-correlation functional is written as

$$E_{xc}^{LDA}[\rho(\mathbf{r})] = \int (\mathcal{E}_x[\rho(\mathbf{r})] + \mathcal{E}_c[\rho(\mathbf{r})])\rho(\mathbf{r})d\mathbf{r} \quad (2.17)$$

where the pure exchange energy $\mathcal{E}_x[\rho]$ is the expression as given above. The expressions for correlation energy are usually given in terms of Wigner-Seitz radius, $r_s = (3/4\pi\rho(\mathbf{r}))^{1/3}$.

The expression proposed by Wigner [8] extrapolates between known limits in r_s , obtained by series expansions. The parameters that appear in the expression proposed by Hedin and Lundquist [9] are determined by fitting to the energy of the uniform electron gas, obtained by numerical methods at different densities. A similar type of expression was proposed by Perdew and Zunger [10], which captures the more sophisticated numerical calculations for the uniform electron gas at different densities performed by Ceperly and Alder [11]. The common feature in all these approaches is that E_{xc} depends on $\rho(\mathbf{r})$ in a local fashion, that is, ρ needs to be evaluated at one point in space at a time. For this reason they are referred to as the Local Density Approximation to Density Functional Theory. This is actually a severe restriction, because even at the exchange level, the functional should be non-local, that is, it should depend on \mathbf{r} and \mathbf{r}' simultaneously. It is a much more difficult task to develop non-local exchange-correlation functionals.

The generalized gradient approximation (GGA)

In a generalized gradient approximation, the functional depends on the density and its gradient,

$$E_{xc}^{GGA}[\rho] = \int \rho(\mathbf{r}) \mathcal{E}_{xc}(\rho(\mathbf{r}), |\nabla\rho(\mathbf{r})|) d\mathbf{r} \quad (2.18)$$

Several GGA functionals like Perdew-Wang 1991 [12] and Perdew, Burke and Ernzerhof (PBE) [13] are the most popular. In comparison to LDA, GGA's tend to improve total energies, atomization energies, energy barriers and structural energy differences [13], while retaining all the correct features of LDA. GGA's expand and soften bonds, an effect that sometimes corrects and sometimes overcorrects the LDA prediction.

2.3 General band-structure methods

To solve the single-particle Kohn-Sham Eqn. (2.13) and to obtain the eigenvalues (band structure) and eigenfunctions, a number of methods have been introduced. These methods are based on either k-space approach or real space approach and are applicable to both finite systems such as molecules or clusters as well as extended systems such as solids. For periodic solids, one usually exploits the translational periodicity and handles the solutions in k-space. For finite sized molecules and clusters also, k-space approach is used by constructing super-cell which imposes artificial periodicity in the system. Since

super-cell must be large enough to avoid spurious interactions with the images, the secular equation becomes large and it will be computationally heavy to solve, specially for bigger clusters. On the other hand, real space based methods [14] like recursion become particularly advantageous for finite and non-periodic systems where the wave-functions vanish outside a boundary and the Coulomb potentials, in general, do not obey periodic boundary conditions. This avoids the use of artificial super-cell.

2.3.1 Basis sets

Regardless of whether it is k-space approach or real-space approach, one has to choose an appropriate basis set to expand the single-particle wave-functions and depending on the choice of basis functions, different schemes, therefore, can be broadly grouped into two categories: (i) methods using energy independent basis sets or fixed basis sets, like tight binding method using linear combination of atomic orbitals (LCAO) type basis [15], orthogonalized plane wave (OPW) method within a pseudopotential scheme using plane waves orthogonalized to core states as the basis set [16, 17] and (ii) methods using energy dependent basis set, like cellular method [18], augmented plane wave (APW) method [19] and the Korringa-Kohn-Rostocker (KKR) Green's function method [20], which use partial waves as basis set. In the methods of fixed basis set, by standard variational techniques one obtains a set of linear eigenvalue equations given by

$$(H - \epsilon O) \cdot \mathbf{b} = 0 \quad (2.19)$$

in terms of the Hamiltonian H and overlap matrix O to determine the eigenvalues ϵ and the expansion coefficients \mathbf{b} . Most of the fixed basis set uses pseudopotential for the electron-ion interaction, where localized core states are got rid of by replacing the strong crystalline potential by a weak pseudopotential, while giving faithful determination of the valence and conduction bands. Pseudopotential in conjunction with plane wave basis has become one of the most versatile and efficient approaches for calculating electronic properties. Methods of partial waves, on the other hand, result in a secular equation of the form,

$$M(\epsilon) \cdot \mathbf{b} = 0 \quad (2.20)$$

In contrast to Eqn. (2.19) which is a polynomial in ϵ , the Eqn. (2.20) has a complicated non-linear energy dependence. We have no a priori idea how many roots we expect, nor whether all roots are physically permissible. The partial wave methods though complicated to solve, do have advantages. Firstly, they provide solutions of arbitrary accuracy for a muffin-tin potential and for closed packed systems, this makes them far more accurate than the traditional fixed basis methods. Secondly, the information about the potential enters only via a few functions of energy. However as already stated, it has the disadvantage of being computationally heavy, the eigen energy ϵ_j must be found individually by tracing the roots of the determinant of M as a function of ϵ . To overcome this, Andersen (1975) first proposed a unified approach for linear methods [21] such as linear augmented plane wave (LAPW) and linear muffin-tin orbital (LMTO) methods which are the linearized versions of APW and KKR methods, respectively. These methods therefore lead to secular equations like (2.19) rather than (2.20) and combine the desirable features of the fixed basis and partial wave methods.

In this thesis, we use pseudopotential method along with plane wave basis, as implemented in the Vienna *ab initio* simulation package (VASP) [22], to study finite sized clusters. Being finite sized objects, cluster calculations have been done using super-cell technique and structural optimization is performed using conjugate gradient or quasi-Newtonian dynamics. For bulk semiconductors as studied in chapter 3, we use N-th order muffin-tin orbital (NMTO) method [23], which use LMTO self-consistent potential as inputs. Therefore, in the following two subsections, we discuss the pseudopotential method and LMTO method in greater details.

Pseudopotential Method

It is well known that electrons in the outermost shell of atoms, the so called valence electrons, actively participate in determining the most of the chemical and physical properties of molecules and solids. This leads to the idea behind the pseudopotential theory. Here we will develop the basic concept of pseudopotential by a simple transformation of single-particle Kohn-Sham equation (2.13) for an atom where core and valence states are denoted as ψ^c and ψ^v respectively. A new set of single-particle valence states $\tilde{\phi}^v$ can be

defined as

$$\psi^v(\mathbf{r}) = \tilde{\phi}^v + \sum_c \alpha_c \psi^c(\mathbf{r}) \quad (2.21)$$

where α_c are determined from the condition that ψ^v and ψ^c are orthogonal to each other *i.e.* $\langle \psi^v | \psi^c \rangle = 0$ which gives $\alpha_c = - \langle \psi^c | \tilde{\phi}^v \rangle$. Eqn. (2.13) then can be manipulated, with the help of Eqn. (2.21), to

$$\left[T_S + V_{KS} + \sum_c (\epsilon^v - \epsilon^c) |\psi^c\rangle \langle \psi^c| \right] \tilde{\phi}^v = \epsilon^v \tilde{\phi}^v \quad (2.22)$$

with ϵ^c as the eigenvalue of the core state. Considering $V_R = \sum_c (\epsilon^v - \epsilon^c) |\psi^c\rangle \langle \psi^c|$ which is a repulsive potential operator (as $\epsilon^v > \epsilon^c$, making $\epsilon^v - \epsilon^c$ positive), Eqn. (2.22) can be written as

$$[T_S + V_{PS}] \tilde{\phi}^v = \epsilon^v \tilde{\phi}^v \quad (2.23)$$

The operator

$$V_{PS} = V_{KS} + \sum_c (\epsilon^v - \epsilon^c) |\psi^c\rangle \langle \psi^c| \quad (2.24)$$

represents a weak attractive potential, denoting the balance between the attractive potential V_{KS} and the repulsive potential V_R , and is called a pseudopotential. The new states $\tilde{\phi}^v$ obey a single-particle equation with a modified potential, but have the same eigenvalues ϵ^v as the original valence state ψ^v and are called pseudo-wavefunctions. These new valence states project out of the valence wavefunctions any overlap they have with the core wavefunctions, thereby having zero overlap with the core states. In other words, through the pseudopotential formulation, we have created a new set of valence states, which experience a weaker potential near the atomic nucleus, but the proper ionic potential away from the core region. Since it is this region in which the valence electrons interact to form bonds that hold the solid together, the pseudo-wavefunctions preserve all the important physics relevant to the behaviour of the solid.

Since then several methods have been used to generate more accurate as well as more efficient pseudo-potentials, keeping the basic principles same. In norm-conserving pseudopotential [24], the all electron (AE) wave function is replaced by a soft nodeless pseudo (PS) wave function, with the restriction to the PS wave function that within the chosen core radius the norm of the PS wave function has to be the same with the AE wave function

and outside the core radius both the wave functions are just identical. Good transferability of constructed pseudopotential requires a core radius around the outermost maximum of the AE wavefunction, because only then the charge distribution and moments of the AE wavefunctions are well produced by the PS wavefunctions. Therefore, for elements with strongly localized orbitals like first-row, $3d$ and rare-earth elements, the resulting pseudopotentials require a large plane-wave basis set. To work around this, compromises are often made by increasing the core radius significantly beyond the outermost maximum in the AE wave-function. But this is usually not a satisfactory solution because the transferability is always adversely affected when the core radius is increased, and for any new chemical environment, additional tests are required to establish the reliability of such soft PS potentials. This was improved by Vanderbilt [25], where the norm-conservation constraint was relaxed and localized atom centred augmentation charges were introduced to make up the charge deficit. These augmentation charges are defined as the charge density difference between the AE and the PS wavefunction, but for convenience, they are pseudized to allow an efficient treatment of the augmentation charges on a regular grid. Only for the augmentation charges, a small cutoff radius must be used to restore the moments and the charge distribution of the AE wavefunction accurately.

The success of this approach is partly hampered by rather difficult construction of the pseudopotential. Later Blöchl [26] has developed the projector-augmented-wave (PAW) method, which combines idea from the LAPW method with the plane wave pseudopotential approach, and finally turns out computationally elegant, transferable and accurate method for electronic structure calculation of transition metals and oxides. Below we have outlined the idea behind the PAW method.

In the PAW method, the AE wavefunction Ψ_n (which is a full one-electron Kohn-Sham wavefunction) is derived from the PS wavefunction $|\tilde{\Psi}_n\rangle$ by means of a linear transformation:

$$|\Psi_n\rangle = |\tilde{\Psi}_n\rangle + \sum_i (|\phi_i\rangle - |\tilde{\phi}_i\rangle) \langle \tilde{p}_i | \tilde{\Psi}_n \rangle \quad (2.25)$$

The index i is a shorthand for the atomic site \mathbf{R} , the angular momentum numbers $L = (l, m)$ and an additional index k referring to the reference energy ϵ_{kl} . The all electron partial waves ϕ_i are the solutions of the radial Schrödinger equation for the isolated atom, and the PS partial waves $\tilde{\phi}_i$ are equivalent to the AE partial waves outside a core

radius r_c^l and match with value and derivative at r_c^l . The core radius r_c^l is usually chosen approximately around half the nearest-neighbour distance. The projector function \tilde{p}_i for each PS partial wave localized within the core radius, obeys the relation $\langle \tilde{p}_i | \tilde{\phi}_i \rangle = \delta_{ij}$. Starting from Eqn. (2.25), it is possible to show that in the PAW method, the AE charge density is given by

$$\rho(\mathbf{r}) = \tilde{\rho}(\mathbf{r}) + \rho^1(\mathbf{r}) - \tilde{\rho}^1(\mathbf{r}) \quad (2.26)$$

where $\tilde{\rho}$ is the soft pseudo-charge density calculated directly from the pseudo wavefunctions on a plane wave grid:

$$\tilde{\rho}(\mathbf{r}) = \sum_n f_n \langle \tilde{\Psi}_n | \mathbf{r} \rangle \langle \mathbf{r} | \tilde{\Psi}_n \rangle \quad (2.27)$$

The on-site charge densities ρ^1 and $\tilde{\rho}^1$ are treated on radial support grids localized around each atom. They are defined as

$$\rho^1(\mathbf{r}) = \sum_{n,(ij)} f_n \langle \tilde{\Psi}_n | \tilde{p}_i \rangle \langle \phi_i | \mathbf{r} \rangle \langle \mathbf{r} | \phi_j \rangle \langle \tilde{p}_j | \tilde{\Psi}_n \rangle \quad (2.28)$$

and

$$\tilde{\rho}^1(\mathbf{r}) = \sum_{n,(ij)} f_n \langle \tilde{\Psi}_n | \tilde{p}_i \rangle \langle \tilde{\phi}_i | \mathbf{r} \rangle \langle \mathbf{r} | \tilde{\phi}_j \rangle \langle \tilde{p}_j | \tilde{\Psi}_n \rangle \quad (2.29)$$

It is to be noted that the charge density $\tilde{\rho}^1$ is exactly the same as $\tilde{\rho}$ within the augmentation spheres around each atom. In PAW approach, an additional density, called compensation charge density is added to both auxiliary densities $\tilde{\rho}$ and $\tilde{\rho}^1$ so that the multi-pole moments of the terms $\rho^1(\mathbf{r}) - \tilde{\rho}^1(\mathbf{r})$ in Eqn. (2.26) vanish. Thus the electrostatic potential due to these terms vanishes outside the augmentation spheres around each atom, just as is accomplished in LAPW method. Like density, the energy can also be written as a sum of three terms and by functional derivatives of the total energy, one can derive the expressions of Kohn-Sham equations.

Linear Muffin-Tin Orbital (LMTO) method

The method relies on the muffin-tin approximation of the potential which divides the space into atom-centred muffin-tin spheres and the interstitial. While the solution of Schrödinger equation inside the spherically symmetric muffin-tin sphere is partial waves, that in the interstitial is plane waves which can be expanded in terms of spherical Neumann and

Bessel functions. The basis is constructed by joining these two solutions at the muffin-tin sphere boundaries continuously and smoothly. Finally the LMTO basis is derived by linearizing this energy dependent basis set. In the further step towards simplification, the method relies on atomic sphere approximation (ASA) which replaces the muffin-tin spheres by space-filling atomic spheres, called Wigner-Seitz (WS) spheres. With the above mentioned approximations, the information needed to set up the Hamiltonian can be divided into two independent parts. The first part contains the structure matrix which depends only on the structure and the positions of the atoms and not on the type of atoms occupying the sites. The second part of the information depends on the solution of the Schrödinger equation inside each inequivalent WS sphere with appropriate boundary conditions. The second part yields the so-called potential parameters for each site.

Within the ASA, the LMTO basis functions have the following form:

$$\chi_{RL}^{\alpha}(\mathbf{r}_R) = \phi_{RL}(\mathbf{r}_R) + \sum_{\mathbf{R}'L'} \dot{\phi}_{R'L'}^{\alpha}(\mathbf{r}'_R) h_{R'L',RL}^{\alpha} \quad (2.30)$$

where L denotes collective angular momentum index (lm). Atomic sites are given by the position vectors \mathbf{R} with $\mathbf{r}_R = \mathbf{r} - \mathbf{R}$. ϕ is a product of a spherical harmonic and the solution $\phi_{\nu RL}(|\mathbf{r}_R|)$ to the radial equation, *i.e.* the partial waves inside the sphere centred at \mathbf{R} for a certain energy $\epsilon_{\nu RL}$ which is the energy of linearization. The functions $\dot{\phi}^{\alpha}$ are the linear combinations of the ϕ 's and their energy derivatives $\dot{\phi}$. The actual choice of how the linear combination is made determines the basis *i.e.* the label α . The functions ϕ are normalized inside the spheres to which they are associated, α and $\dot{\phi}$ are orthogonal and they vanish, by definition outside their own sphere. The matrix h^{α} is given by

$$h^{\alpha} = C^{\alpha} - \epsilon_{\nu} + (\Delta^{\alpha})^{1/2} S^{\alpha} (\Delta^{\alpha})^{1/2} \quad (2.31)$$

where C and Δ are the diagonal potential matrices and S is the structure matrix depending on the representation and the geometrical arrangement of the atomic sites.

Although the LMTO method has been highly successful in doing electronic structure calculation with nominal computational cost, it has some disadvantages, like :

(i) The basis is complete to $(\epsilon - \epsilon_{\nu})$ (*i.e.*, 1st order) inside the sphere while it is complete to $(\epsilon - \epsilon_{\nu})^0 = 1$ (*i.e.*, 0th order) in the interstitial which is inconsistent. It can be made consistent by removing the interstitial region by ASA.

(ii) The expansion of the Hamiltonian H in the orthogonal representation as a power series in the two centred tight-binding Hamiltonian h :

$$\langle \tilde{\chi} | H | \tilde{\chi} \rangle = \epsilon_\nu + h - hoh + \dots \quad (2.32)$$

is obtained only within ASA and excluding downfolding.

All these disadvantages have been taken into account in NMTO method, which provides a more consistent formalism, treats the interstitial region accurately and goes beyond the linear approximation. The primary features of this method are : (i) it still has a muffin-tin potential, (ii) it still uses the partial waves, ϕ within the atomic spheres, (iii) instead of Neumann function it uses screened spherical waves (SSWs) in the interstitial region, (iv) out of partial waves and SSWs it defines the kinked partial waves (KPWs), (v) it constructs energy-independent NMTOs, which are superpositions of KPWs evaluated at $N+1$ energy points. We will discuss more about this method in chapter 3.

2.3.2 Real space recursion method

Besides clusters, we have also studied in this thesis, the conductance of 1D atomic chain. Our formalism for this study is based on real space vector recursion technique which is the generalized version of scalar recursion technique. Here we will discuss the scalar recursion technique briefly. The real-space based scalar recursion method (Haydock, Heine and Kelly, 1972) is a very convenient approach for the determination of the eigen-solutions of matrices, especially those of very large rank and sparse character (*i.e.* with many matrix elements equal to zero). In the field of electronic structure calculations, the recursion method has been originally introduced in connection with local basis representation of the electronic states in solids. Since the LMTO method gives the Hamiltonian in the tight-binding form [Eqn. (2.32)], the recursion method is therefore suitably used in connection with TB-LMTO basis sets. The underlying principle of the recursion method is very simple and very general at the same time. Consider a quantum system, described by Hamiltonian H which may be of tight-binding form and a number N (arbitrarily large) of orthonormal basis states $\{|i\rangle\} (i = 1, 2, \dots, N)$. Starting from any given state $|n_0\rangle$ belonging to the space spanned by $\{|i\rangle\}$, the recursion method maps the original basis set $\{|i\rangle\}$ into a new set of orthonormal basis set $\{|n\rangle\rangle\}$ such that the Hamiltonian in this new

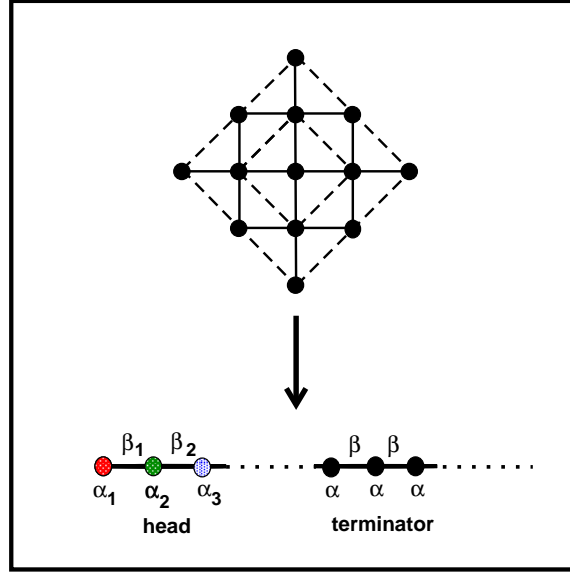


Figure 2.1: Recursive reduction of a square lattice to an equivalent linear chain.

representation becomes a tridiagonal matrix. A tridiagonal matrix is equivalent to a one-dimensional chain. So recursion method is nothing but a change of basis which converts the original quantum system into an effective one-dimensional chain representation.

To illustrate the procedure, let us take an example of a square lattice with the starting state of the new basis $|1\rangle\rangle$ at site 1 *i.e.* $|1\rangle$. The other members are then generated using the following recursion formula:

$$\begin{aligned} |2\rangle\rangle &= H|1\rangle\rangle - a_1|1\rangle\rangle \\ |n+1\rangle\rangle &= H|n\rangle\rangle - a_n|n\rangle\rangle - b_n^2|n-1\rangle\rangle \quad n \geq 3 \end{aligned} \quad (2.33)$$

Using Eqn. (2.33), we immediately get :

$$a_n = \frac{\langle\langle n|H|n\rangle\rangle}{\langle\langle n|n\rangle\rangle} \quad \text{and} \quad b_n^2 = \frac{\langle\langle n|n\rangle\rangle}{\langle\langle n-1|n-1\rangle\rangle} \quad (2.34)$$

Fig. 2.1 shows schematically the recursive reduction of a square lattice where the dotted shells represent the consecutive recursion steps.

Once the linear transformation has been achieved, we can write expression for the Green

function matrix elements; in particular the matrix element $G_{11}(E)$ of the Green's function is given by the continued fraction expression

$$G_{11}(E) = \langle\langle 1 | \frac{1}{E - H} | 1 \rangle\rangle = \frac{b_1^2}{E - a_1 - \frac{b_2^2}{E - a_2 - \frac{b_3^3}{E - a_3 - \dots}}} \quad (2.35)$$

Notice that the expansion of the Green function is possible only because of the tridiagonal structure of the Hamiltonian. Once the Green function is obtained, one can calculate any physically measurable quantity related to electronic properties of a solid. For example, using $G_{11}(E)$, the local density of states projected on $|1\rangle$ of the Hamiltonian operator H can be obtained as

$$\rho_0(E) = -\frac{1}{\pi} \lim_{\epsilon \rightarrow 0^+} \text{Im} G_{11}(E + i\epsilon) \quad (2.36)$$

where ϵ is an infinitesimal positive quantity.

Vector recursion is the generalized version of the recursion technique which transforms the system Hamiltonian into block-tridiagonal form where each matrix element is itself a matrix. This transformation allows calculation of the scattering matrix by means of a stable three-term recurrence and a straightforward matching of boundary conditions. We will discuss the vector recursion technique in detail in chapter 7, where we have implemented it to study the electrical transport properties of 1D atomic chain connected with 3D leads.

Bibliography

- [1] M. Born, and J. R. Oppenheimer, “Zur Quantentheorie der Molekeln”, *Ann. Physik* **84**, 457 (1927).
- [2] D. R. Hartree, “The wave mechanics of an atom with non-coulombic central field: parts I, II, III”, *Proc. Cambridge Phil. Soc.* **24**, 89, 111, 426 (1928).
- [3] V. Fock, “Naherungsmethode zur Losung des quanten-mechanischen Mehrkorperprobleme”, *Z. Phys.* **61**, 126 (1930).
- [4] J. C. Slater, “The Theory of Complex Spectra”, *Phys. Rev.* **34**, 1293 (1929).
- [5] P. Hohenberg and W. Kohn, *Phys. Rev. B* **136**, 864 (1964).
- [6] W. Kohn and L. J. Sham, *Phys. Rev. A* **140**, 1133 (1965).
- [7] E. Kaxiras, *Atomic and Electronic Structure of Solids*; Cambridge University Press, UK, p. 62-65, 2003.
- [8] E.P. Wigner, *Phys. Rev.* **46**, 1002 (1934); see also R.M. Dreizler and E.K.U. Gross, *Density Functional Theory*, Springer, New York (1990).
- [9] L. Hedin and B.I. Lundqvist, *J. Phys. C* **4**, 2064 (1971).
- [10] J.P. Perdew and A. Zunger, *Phys. Rev. B* **23**, 5048 (1981).
- [11] D.M. Ceperley and B.J. Alder, *Phys. Rev. Lett.* **45**, 566 (1980).
- [12] J. P. Perdew, *in Electronic Structure of Solids ' 91*, edited by P. Ziesche and H. Eschrig (Akademie Verlag, Berlin, 1991), p. 11.

- [13] J. P. Perdew, K. Burke and M. Ernzerhof, *Phys. Rev. Lett.* **77**, 3865 (1996).
- [14] T. L. Beck, *Rev. Mod. Phys.* **72**, 1041 (2000).
- [15] J. C. Slater and G. F. Koster, *Phys. Rev.* **94**, 1498 (1954).
- [16] W. C. Herring, *Phys. Rev.* **57**, 1169 (1940); W. C. Herring and A. G. Hill, *Phys. Rev.* **58**, 132 (1940).
- [17] J. C. Phillips and L. Kleinman, *Phys. Rev.* **116**, 287 (1959).
- [18] E. P. Wigner and F. Seitz, *Phys. Rev.* **46**, 509 (1934).
- [19] T. L. Loucks, *Augmented Plane Wave Methods*, (Benjamin, New York, 1967).
- [20] J. Koringa, *Physica* **13**, 392 (1947); J. Koringa, *Phys. Rev.* **238**, 341 (1994).
- [21] O. K. Andersen, *Phys. Rev. B* **12**, 3060 (1975).
- [22] G. Kresse and J. Hafner, *Phys. Rev. B* **47**, 558 (1993); G. Kresse and J. Furthmuller, *Phys. Rev. B* **54**, 11169 (1996).
- [23] O.K. Andersen and T. Saha-Dasgupta, *Phys. Rev. B* **62**, R16219 (2000) and references there in.
- [24] D.R. Hamann, M. Schlüter and C. Chiang, *Phys. Rev. Lett.* **43**, 1494 (1979).
- [25] D. Vanderbilt, *Phys. Rev. B* **41**, 7892 (1985) .
- [26] P. E. Blöchl, *Phys. Rev. B* **50**, 17953 (1994).

Chapter 3

Relative stability of zinc-blende and wurtzite structure in bulk CdX (X = S, Se, Te) : a Wannier function study

Tetrahedrally co-ordinated binary octet semiconductors are reported to crystallize both in cubic ZB and hexagonal WZ structures at ambient temperature and pressure. The relative stability of these structures and its origin have been investigated in terms of model as well as first principles calculations in past. The common understanding arising out of these studies is that more ionic solids prefer WZ structure, while more covalent solids stabilize in ZB structure. However, the search is still on for a microscopic understanding behind this general trend. With the help of our work in this chapter, we have been able to provide a microscopic detail of the relative stability in the bulk CdX (X = S, Se, Te) series using Wannier function analysis constructed out the of N-th order muffin-tin orbital technique. The applied methodology brings out the correct experimental trend within this series.¹

3.1 Introduction

Tetrahedrally coordinated binary semiconductors of $A^N B^{8-N}$ type having total of eight valence electrons are compounds of great technological importance [1, 2]. They have been widely studied both theoretically and experimentally [3]-[5]. An interesting aspect of

¹This chapter is based on the following paper:

Soumendu Datta, Tanusri Saha-Dasgupta and D. D. Sarma, *Wannier function Study of Relative Stability of Zinc-blende and Wurtzite Structure in the CdX (X = S, Se, Te) series*, J. Phys. : Condens. Matter, **20**, 445217 (2008).

these compounds is that they can belong to either in cubic or in hexagonal symmetry, namely in ZB or in WZ structure. The difference between the two structures is subtle, both being of tetrahedral coordination, and also the associated total energy difference is small, of the order of few meV/atom. These particular aspects have made the ZB vs WZ structural stability issue a topic of significant interest that have been discussed in literature both in terms of model calculations as well as in terms of first principles calculations [6]-[16]. Phillips and Van Vechten [8] first gave a well defined prescription in terms of ionicity to predict the crystalline phase in binary octet semiconductors of $A^N B^{8-N}$ type, with the help of the dielectric theory. While their theory nicely described the transition from four-fold to six-fold coordination and possibly also to eight-fold coordination, it was not able to distinguish clearly between structures having the same coordination. P. Lawaetz [10] investigated the stability of WZ structure more closely. Taking into account the short-range elastic forces and long-range Coulomb forces, he correlated the ZB vs WZ stability with the deviation of the axial ratio c/a from the ideal value, which was further related with a structure-independent charge parameter. However, the results were not fully satisfactory because of limited knowledge about the long-range Coulomb-effects in partially ionic materials. Tomonori [14] achieved some success in systematization of polytypism by relating the energy difference of ZB and WZ phases to a simple empirical formula. Christensen *et al* [15] studied the structural phase stability of 34 elemental and compound semiconductors from first principles electronic structure calculations which involved mostly four-fold to six-fold coordination transitions. They studied the chemical trends by calculating the valence charge densities using LMTO based localized basis sets. Their calculated ionicities from tight-binding representation of LMTO Hamiltonian, gave better chemical trend than Phillips value. Recently, the ZB - WZ polytypism in binary octet semiconductors has been studied by Yeh *et al* [16] in terms of quantum mechanically defined atomic-orbital radii. They showed a linear scaling between the ZB - WZ energy difference and atomistic orbital radii and successfully predicted the structural trends in most of the octet compounds, except some few cases. However, this study was mainly based on atomistic characteristics and not directly related with the atomic arrangement of both the phases. The general understanding that emerged out of all these calculations is that it is the competition between the covalency and the ionicity effects that determines

the relative stability of ZB vs WZ structures, with covalency favouring ZB structure and ionicity favouring WZ structure.

Experimentally, the stable crystal phase of CdS is hexagonal WZ structure [17] (see also Fig. 1.2). For CdSe, ZB is the stable low temperature phase and above a critical temperature, it transforms to WZ structure [18]. On the other hand, CdTe always stabilizes in cubic ZB structure [19]. However, there is a few indication of metastable WZ growth for CdTe in some special situation [20]. In the present work, we revisited the issue of relative stability of ZB and WZ in the CdX series, with $X = \text{S, Se, Te}$ using NMTO technique [21] within the framework of DFT. In particular, we employed the “direct generation of Wannier-like orbitals” feature of NMTO technique for obtaining the microscopic understanding in this context.

3.2 Crystal structure

The ZB structure consists of two interpenetrating face centred cubic sub-lattices, one of atom A, the other of atom B, displaced from each other along the body diagonal by $a/4$, a being the lattice constant for the ZB structure. On the other hand, an ideal WZ structure consists of two interpenetrating hexagonal closed packed sublattices, one of atom A, the other of atom B, displaced from each other by $3c/16$ along the c -axis. These result into two different stacking sequences: ABCABC... along [111] direction for ZB and ABAB... along c -axis for WZ. The ZB structure corresponds to the *staggered* conformation of atomic arrangement along [111] body diagonal, while the WZ structure corresponds to the *eclipsed* conformation as seen looking down the c -axis. The nearest neighbour (tetrahedral bond) arrangements in the ZB structure and in the ideal WZ structure are identical. The main difference starts to come in the relative position of 3rd nearest neighbours and beyond. Also the arrangement of the distant atoms along the four different tetrahedral bonds are different for a WZ structure. The structural differences between these two phases have been shown in Fig. 3.1.

The lower symmetry of the WZ structure allows for a distortion with the c/a ratio deviating from the ideal value of $\sqrt{\frac{8}{3}} = 1.633$. A further kind of distortion, that is possible in the hexagonal structure and forbidden in the cubic, is that the two interpenetrating

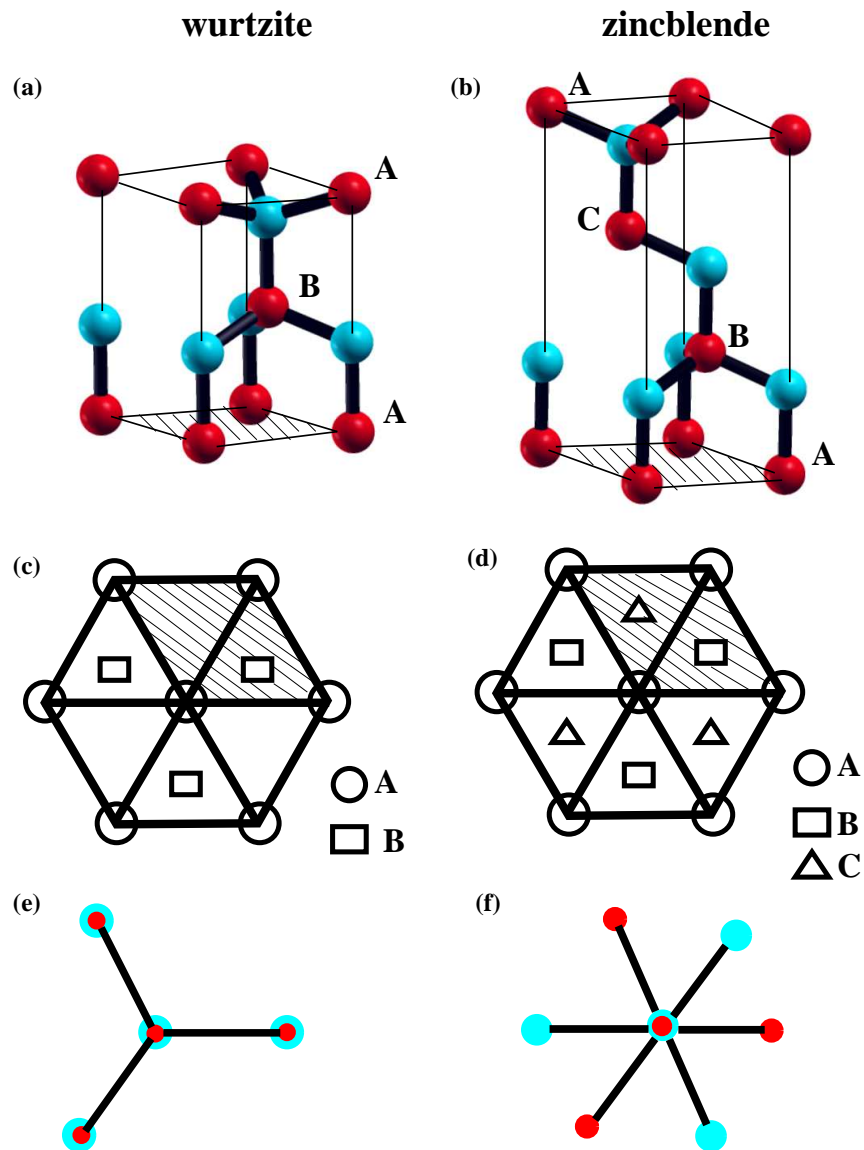


Figure 3.1: (a) and (b) show the crystal structures in WZ and ZB symmetries. Two different coloured atoms denote cation and anion. (c) WZ structure shows the ABAB... stacking of atoms, while (d) ZB structure shows the ABCABC... stacking. *Eclipsed* and *staggered* conformation of atoms along c -axis in WZ structure and along $[111]$ body diagonal in ZB structure have been shown in (e) and (f), respectively.

sublattices are slightly displaced from their ideal positions. In order to capture these distortions, it is necessary to define another internal parameter “ u ”, which is the nearest neighbour distance along c -axis, in unit of c . The value u in the ideal WZ structure is $3/8 = 0.375$. Deviation of u from its ideal value gives rise to a dipole at the centre of each tetrahedron, containing an atom of opposite kind, the magnitude of which depends upon Δu [$\Delta u = u - 0.375$] and the ionicity of the chemical bonds. This effect also lowers the ionization energy. The structural parameters of CdS, CdSe and CdTe used in the present calculation are listed in Table 3.1.

Table 3.1: Structural parameters of ZB and WZ phases for CdX (X = S, Se, Te) series. Lattice parameters have been taken from Ref. [16] for both ZB and WZ phases of CdS, from Ref. [22] for ZB CdSe, from Ref. [23] for WZ phase of CdSe, from Ref. [19] for ZB CdTe and from Ref. [20] for WZ CdTe.

Compounds	WZ					ZB
	a (Å)	c/a	u	$\Delta(c/a)$	Δu	a (Å)
CdS	4.121	1.621	0.377	-0.012	0.002	5.811
CdSe	4.299	1.631	0.376	-0.002	0.001	6.077
CdTe	4.57	1.637	0.375	0.004	0.000	6.492

It shows that the deviation $\Delta(c/a)$ [$\Delta(c/a) = c/a - 1.633$] is negative and largest for CdS, while it is positive for CdTe. The deviation from the ideal c/a ratio is tiny for CdSe. The deviation Δu is found to be opposite in sign to that of $\Delta(c/a)$. A part of the deviation Δu is expected to come due to nearest neighbour bond bending or bond stretching caused by $\Delta(c/a)$. The limits on this part, as calculated by Keffer and Portis [7] for AlN, are $u = 0.380$ to maintain equal nearest neighbour bond lengths and $u = 0.372$ to maintain equal four tetrahedral angles. However, the measured value of u for AlN is 0.385 [7]. This means there must be additional contribution in the distortion of u from ideal value, which is coming from the long-range Coulomb interaction. The NMTO technique based on full self-consistent DFT calculations includes both the effect of short-range as well as long-range interaction in providing a complete understanding.

3.3 Total energy calculations

In order to check the relative stability of the ZB and WZ structures of the CdS, CdSe and CdTe, we carried out total energy calculations using the energetically accurate pseudo-potential basis set. The calculations have been performed with PAW pseudopotential [24] and GGA exchange-correlation functionals as implemented in VASP package. The wavefunctions are expanded in the plane wave basis set with a kinetic energy cut-off of 280 eV which gives convergence of total energy sufficient to discuss the relative stability of various phases. The calculations have been carried out with a k -space grid of $11 \times 11 \times 11$. The obtained total energies and the band gaps are listed in Table 3.2. As found, the total energy differences are indeed very tiny; of the order of few meV. Our calculations correctly show that CdS to be stable in WZ phase and CdTe to be stable in ZB phase. CdSe, which is considered as a borderline case, is found to be stable in ZB phase in agreement with the published results [16]. The band gaps in WZ and ZB structures, both being direct band gaps for CdS, CdSe and CdTe are similar for a given compound. As expected, the calculated band gaps are underestimated due to the overbinding problem related with local density approximation of exchange-correlation functional. It is found that the band gap decreases monotonically in moving from CdS to CdTe in both ZB and WZ symmetries. This monotonic decrease in band gap indicates the enhanced metallicity across the CdS-CdSe-CdTe series which points to CdTe being more covalent compared to CdS.

3.4 Calculation of ionicity

As already pointed out, the relative stability between ZB and WZ phases of $A^N B^{8-N}$ semiconductors is dictated by the competition between the covalent bonding and the electrostatic energy given by the difference between the cation and anion energy levels. For a homopolar semiconductors like Si, it is only the first term that survives. For a tetrahedrally coordinated semiconductor, it is most natural to think in terms of sp^3 hybrids. Considering the sp^3 hybrid energy as $E_{sp^3} = (E_s + 3E_p)/4$ the energy level separation between cation and anion is given by $\Delta E_{sp^3} = E_{sp^3}^c - E_{sp^3}^a$; where c and a denote cation and anion respectively. The hybridization contribution on the other hand

Table 3.2: Total energy per formula, energy difference $\Delta E = E(ZB) - E(WZ)$ and band gaps. + ve sign of ΔE indicates WZ is more stable than ZB and vice versa. The numbers within the parenthesis in the columns of band gap, correspond to their experimental values taken from Ref. [25].

Compounds	Energy(eV/formula)		ΔE (meV)	Band gap(eV)	
	ZB	WZ		ZB	WZ
CdS	-5.2930	-5.2972	4.2	1.15 (2.55)	1.24 (2.58)
CdSe	-4.7630	-4.7601	-2.9	0.97(1.90)	0.99(1.83)
CdTe	-4.1934	-4.1729	-20.5	0.75(1.60)	0.83(1.60)

is related to the hopping integral between the cation and anion sp^3 hybrids. It is given by $h = \frac{1}{4} \langle s^a + p_x^a + p_y^a + p_z^a | H | s^c - p_x^c - p_y^c - p_z^c \rangle$ considering the [111] bond of ZB structure and $h = \frac{1}{2} \langle s^a + p_z^a | H | s^c - p_z^c \rangle$ considering the [001] bond of WZ structure where H is the tight binding Hamiltonian in the sp basis of cation and anion. The ionicity is then defined as [15]

$$f_i = \frac{(\Delta E_{sp^3})^2}{(\Delta E_{sp^3})^2 + (2h)^2} \quad (3.1)$$

In order to extract the energy level separation and the hopping interaction, we employed the NMTO-downfolding technique. In this method, a basis set of localized orbitals is constructed from the exact scattering solutions (partial waves and Hankel functions) for a superposition of short-ranged spherically-symmetric potential wells, a so called muffin-tin approximation to the potential. The basis set is constructed from the scattering solutions at a mesh of energies, $\epsilon_0, \epsilon_1, \dots, \epsilon_N$. At those energies, the set provides the exact solutions, while at other energies, E , the error is proportional to $(E - \epsilon_0)(E - \epsilon_1) \dots (E - \epsilon_N)$. The basis set of NMTOs is therefore selective in energy. Moreover, each NMTO satisfies a specific boundary condition which gives it a specific orbital character and makes it localized. The NMTO basis set due to its energy selective character is *flexible* and can be chosen as *minimal* via the downfolding procedure. The downfolding procedure is an energy selection procedure which selectively picks up few bands of interest out of the LDA

all band calculation by integrating out degrees of freedom that are not of interest, called the passive channels and retaining few degrees of freedom, called active channels. The downfolded NMTO set spans only the selected set of bands with as few basis functions as there are bands. For the isolated set of selected bands the NMTO set spans the Hilbert space of the Wannier functions, that is, the orthonormalized NMTOs are the Wannier functions. The Wannier orbitals are therefore generated directly in this method, which may be contrasted with the techniques where Wannier functions are generated out of the calculated Bloch functions as a post processing step [26]. The downfolded Hamiltonian in the Wannier basis provides the estimates of on site energies and the hopping integrals.

In order to compute the ionicity parameter defined in Eqn. (3.1), the NMTO calculations have been carried out with Cd(*spd*) and X(*sp*) basis. NMTO calculations being not yet implemented in self-consistent form, the self consistent calculations have been carried out in the LMTO method. The self consistent MT potential out of these LMTO calculations has been used for the constructions of NMTOs, which in the present case is the standard LMTO all-electron CdXEE' atomic spheres potential for the ZB structure and Cd₂X₂E₂E'₂ for the WZ structure. *E* and *E'* are two different empty spheres used to fill the space. The calculated estimates of ΔE_{sp^3} , hopping integral *h* and ionicity parameter f_i for CdX series are listed in Table 3.3. The NMTO approach successfully brings out the right trend within the CdX series both for the ZB and the WZ structures, *i.e.* CdS has the maximum ionicity and CdTe has the least. For comparison, the results of previous calculations by Christensen *et al* [15] using the tight-binding LMTO approach and that by Phillips [4] using dielectric theory are also listed. As it is found, while NMTO could bring out the right trend within the fine differences, the two previous approaches could not capture it properly. For example, both in Ref. [15] and in Ref. [4] (see Table 3.3) the ionicity of CdSe turned out to be higher than that in CdS. Ref. [4] gets CdTe to be of even higher ionicity. We have also compared our results with the Pauling ionicities which are based on empirical heats of formation and are calculated for $A^N B^{8-N}$ compounds from the electronegativity difference via

$$f_i(Pa) = 1 - \frac{N}{M} \exp\left(-\frac{|X_A - X_B|^2}{4}\right)$$

where $|X_A - X_B|$ is the electronegativity difference between elements *A* and *B*, and *M*

is the coordination number. Pauling ionicities have right trend and these values are comparable with our calculated values.

Table 3.3: Covalent gap ΔE_{sp^3} , hopping term $E_h = -2h$ and ionicity f_i for the CdX series in ZB and WZ structure. $f_i(C)$ means calculated value of ionicity by Christensen *et al* from Ref. [15], $f_i(Ph)$ that of Phillips taken from Ref. [4] and $f_i(Pa)$ that of Pauling taken from Ref. [5].

Compounds	ΔE_{sp^3} (eV)		$E_h = -2h$ (eV)		f_i		$f_i(C)$	$f_i(Ph)$	$f_i(Pa)$
	ZB	WZ	ZB	WZ	ZB	WZ			
CdS	7.13	7.17	6.37	6.29	0.556	0.565	0.794	0.685	0.59
CdSe	6.70	6.69	6.16	6.04	0.542	0.551	0.841	0.699	0.58
CdTe	5.36	5.45	5.79	5.74	0.462	0.475	0.739	0.717	0.52

3.5 Microscopic understanding in terms of calculated Wannier functions

In order to gain further insights, we went a step ahead and constructed the truly *minimal* NMTO sets with the *sp*-orbitals placed exclusively on the anion (X) site and downfolded all the orbitals at the cation (Cd) site, except the cation *d* orbitals. This gives rise to the basis with only 4 *sp*-orbitals out of 8 *sp*-orbitals in the ZB unit cell and 8 *sp*-orbitals out of 16 *sp*-orbitals in the WZ unit cell. The energy points are chosen in the way so as to span only the valence bands. The comparison of the downfolded valence-only bands and the full band structure can be made as good as possible by making the energy mesh finer and finer. The plot shown in Fig. 3.2 for CdS with the choice of 4 energy points already shows the downfolded bands to be indistinguishable from the full band structure in the scale of the plot. Similar agreements are found also for CdSe and CdTe.

Fig. 3.3 shows the plot of the orthonormalized *p*-NMTO ($N = 3$) centred at the anion site and pointing to the neighbouring Cd site along the [111] direction for the ZB structure and [001] direction for the WZ structure. As it is clearly seen, the red lobe at the

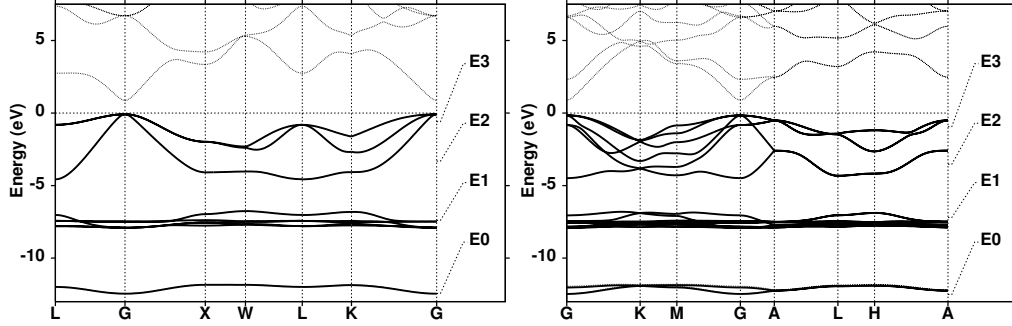


Figure 3.2: Downfolded bands (thick line) with the basis sets where sp -MTOs are on S atom and d -MTOs are on Cd atom, are compared with NMTO all bands (thin line) both in ZB (left) and WZ (right) structure of CdS. The energy mesh for downfolding have also been shown.

left-hand side which is a mark of the covalency effect, systematically increases in moving from S to Se to Te. Had it been plotted for the case of homopolar system like Si which is a perfectly covalent compound, the plot would have been perfectly symmetric with the red lobes being symmetric between the left hand side and the right hand side. These plots reconfirm the conclusion that the ionicity decreases and the covalency increases across the CdX series.

Fig. 3.4 shows the plots of directed p -NMTO same as in Fig. 3.3 but for four different tetrahedral bond directions of WZ and ZB structure for CdS. While the four bond-centred p -NMTOs look identical for ZB structure, the bond-centred p -NMTO directed along the $[001]$ direction of the WZ structure, looks different from the rest of the three. The difference primarily comes from the tail sitting at Cd position at $c(1-u)$ measured from the central anion position at $X(0,0,0)$ along the $[001]$ axis (see Fig. 3.5). There is no equivalent neighbouring atom along the other three directions.

In order to understand this effect, we have carried out model calculations where $\Delta(c/a)$ ratios have been made -0.1, -0.05 and 0.1. The corresponding u parameter in each case has been obtained by total energy minimization, fixing the lattice parameters. The deviation in u , Δu is found to roughly obey the relationship with $\Delta(c/a)$ as $\Delta u = -\sqrt{\frac{3}{128}}\xi\Delta(c/a)$ where ξ , the bond-bending parameter, is 2.0, as given by Lawaetz [10]. We computed the ionicity parameter f_i for each of the model systems by NMTO downfolding technique. In

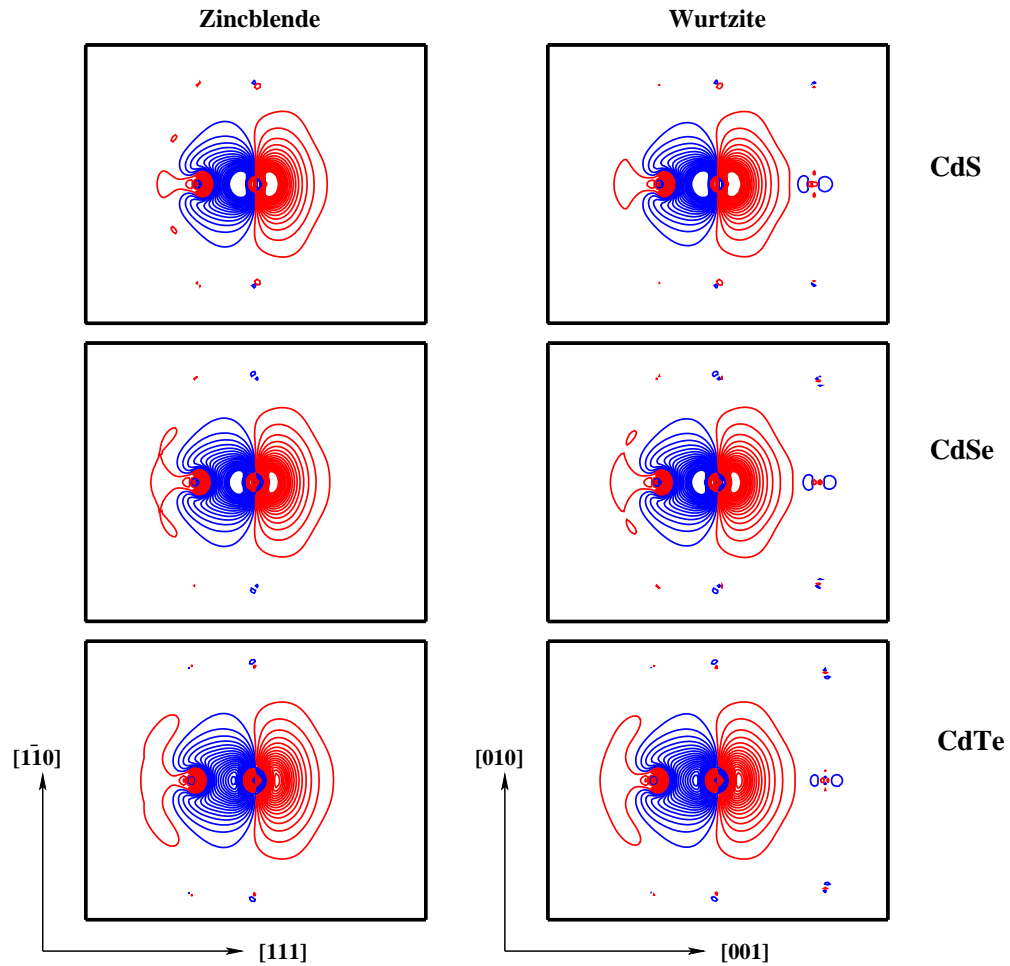


Figure 3.3: The contour plots show the anion $p[111]$ MTO in ZB structure (left panels) and anion $p[001]$ MTO in WZ structure (right panels) of CdX (X = S, Se, Te). The top most panels correspond to CdS and the bottom most to CdTe. In each case, 35 contours have been drawn in the range -0.15 to 0.15 electrons/Bohr³. From top to bottom, the ionicity decreases and the covalency increases.

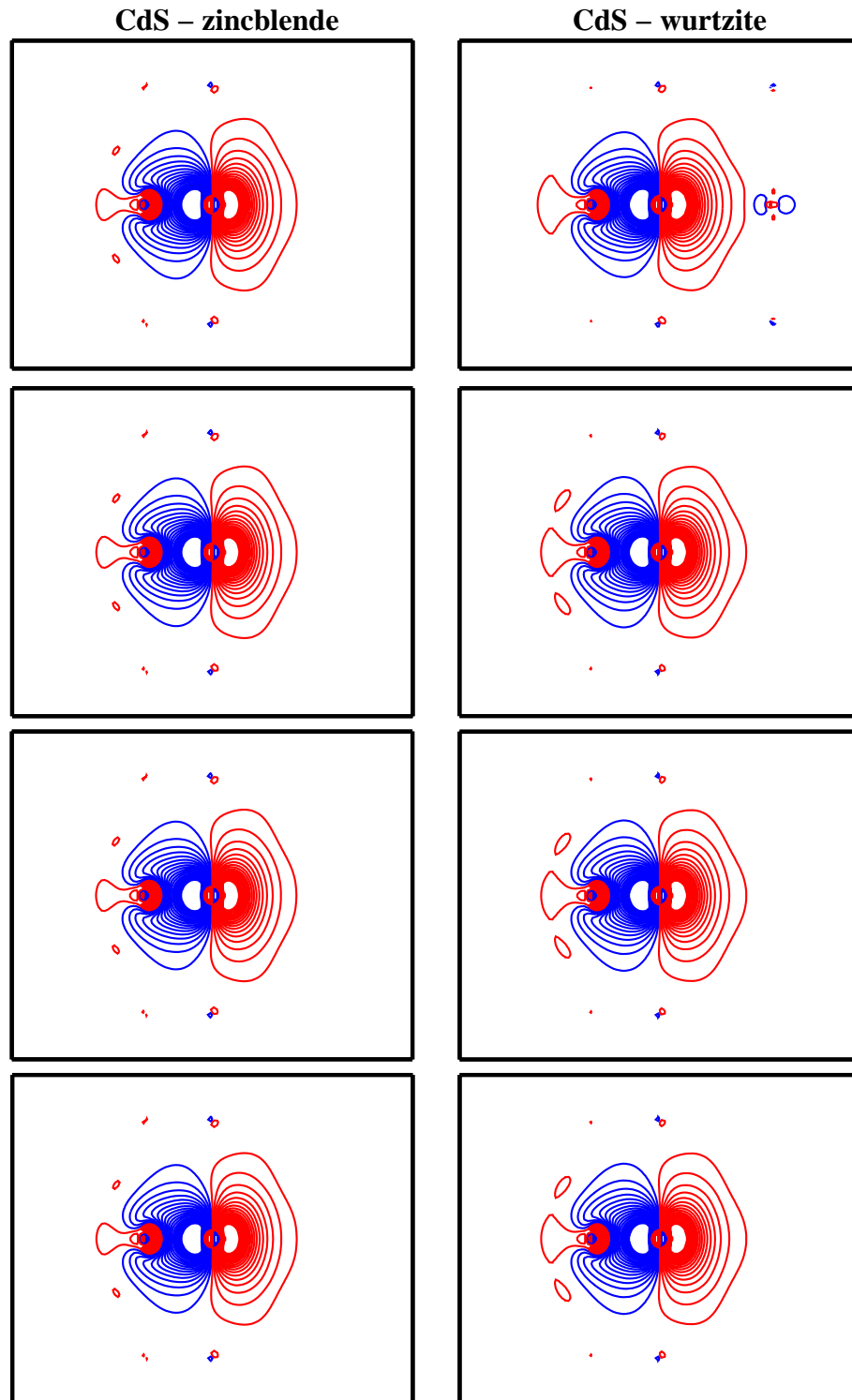


Figure 3.4: The contour plots show the p -MTO of S along the four nearest neighbour tetrahedral directions in ZB structure (left panels; from top to bottom they are $p[111]$, $p[1\bar{1}\bar{1}]$, $p[\bar{1}\bar{1}\bar{1}]$, $p[\bar{1}\bar{1}\bar{1}]$) and in WZ structure (right panels; from top to bottom they are $p[001]$, $p[1, 0, \frac{u}{\sqrt{3}}c/a]$, $p[\frac{1}{2}, -\frac{\sqrt{3}}{2}, -\frac{2}{\sqrt{3}}uc/a]$, $p[\frac{1}{2}, \frac{\sqrt{3}}{2}, -\frac{2}{\sqrt{3}}uc/a]$) of CdS. The contours chosen are same as in Fig. 3.3.

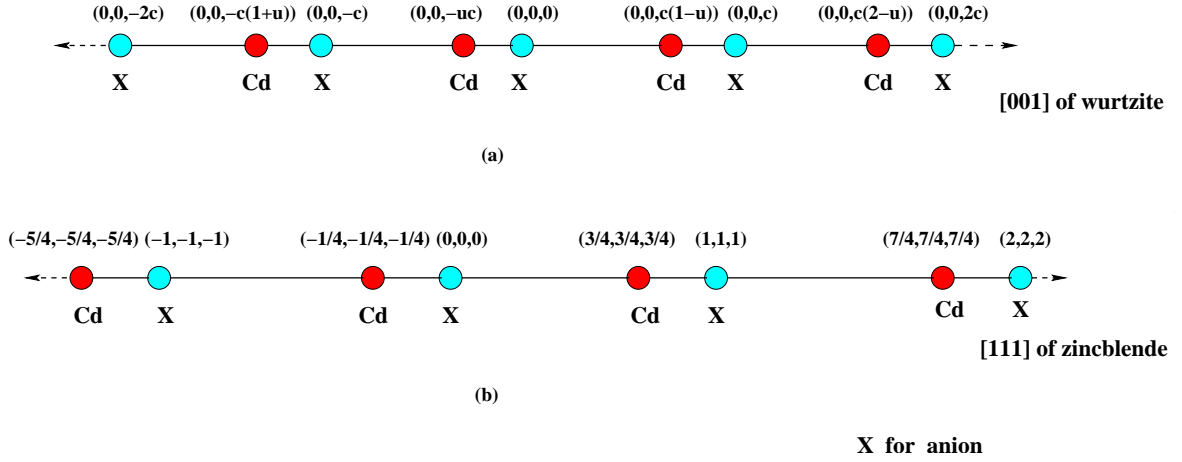


Figure 3.5: (a) Positions of atoms along [001] direction of wurtzite structure, (b) positions of atoms in unit of lattice constant along [111] direction of zinc-blende structure.

Table 3.4 we list the ionicity parameter for the model WZ systems, together with actual CdTe case. Evidently, the negative deviation from ideal (c/a) ratio makes the compound more ionic as pointed out previously. Changing $\Delta(c/a)$ ratio from negative to positive passing through the ideal $\Delta(c/a)$ ratio, the ionicity decreases and covalency increases. This is in agreement with the structural parameters of CdS, CdSe and CdTe. CdS being the most ionic among the three, shows the largest negative deviation in (c/a). (c/a) ratio for CdSe is close to ideal, while deviation in (c/a) ratio for CdTe becomes positive.

Table 3.4: Covalent gap ΔE_{sp^3} , hopping term $E_h = -2h$ and ionicity f_i for model CdTe in WZ structure, with $\Delta(c/a)$ and u as given in the first column.

CdTe	ΔE_{sp^3} (eV)	$E_h = -2h$ (eV)	f_i
$\Delta(c/a) = -0.100$ and $u = 0.4044$	5.49	5.33	0.515
$\Delta(c/a) = -0.050$ and $u = 0.3903$	5.48	5.57	0.491
$\Delta(c/a) = +0.004$ and $u = 0.375$	5.45	5.73	0.475
$\Delta(c/a) = +0.100$ and $u = 0.3432$	5.45	6.13	0.441

In Fig. 3.6, we show the downfolded p -NMTO for the model WZ systems together with actual WZ CdTe system along [001] direction and one of the three other directions,

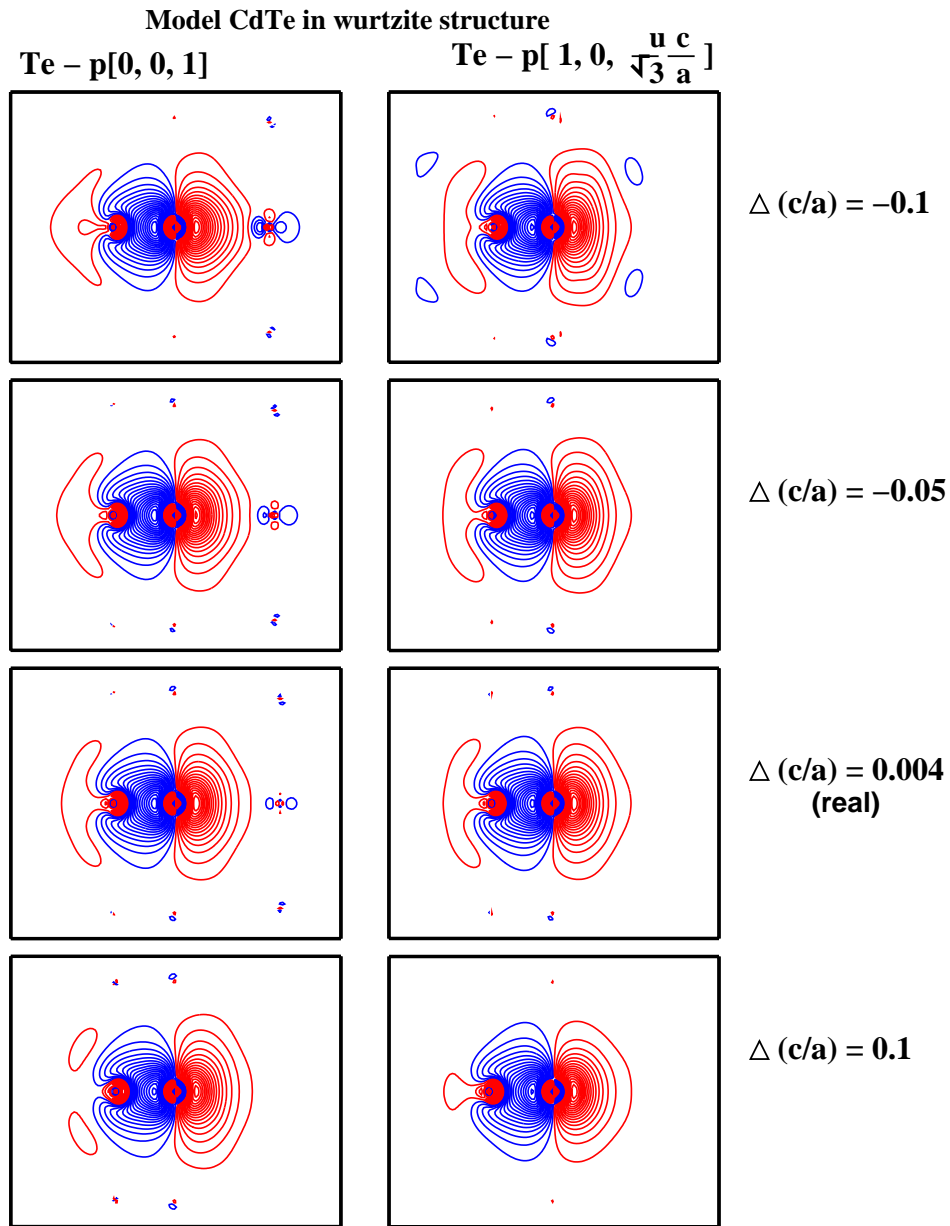


Figure 3.6: The above contour plots show the p -MTO of Te in WZ structure of model CdTe. The left panels correspond to $p[001]$ and right panels correspond to $p[1, 0, (u/\sqrt{3})c/a]$. From top to bottom ionicity decreases and covalency increases and distribution becomes more isotropic. The contours chosen are same as in Fig. 3.3.

namely $[1, 0, (u/\sqrt{3})(c/a)]$. As it is evident, changing $\Delta(c/a)$ from negative to positive makes the two p -NMTOs directed along the vertical $[001]$ bond and one of the other directions, looking alike, diminishing the tail effect sitting at Cd $[0, 0, c(1 - u)]$ site. This is driven by the covalency effect which prefers an isotropic arrangement. However, it cannot be completely achieved within a hexagonal symmetry, a compound with nearly ideal (c/a) or positive $\Delta(c/a)$ ratio therefore prefers to stabilize in ZB symmetry, satisfying the isotropic distribution completely.

In order to have quantitative estimates of ionicity based on truly *minimal* Wannier functions, we have also computed the shift of the centre of gravity of the Wannier function from the bond centre, introduced by Abu-Farsakh *et al* [27] as $\beta = r/d$; where r is the distance between the centre of the Wannier function and the position of the cation of the associated bond, and d is the bond length. Table 3.5 contains our calculated values of bond ionicities β for the CdX series in both ZB and WZ structures. The calculated bond ionicity gradually decreases and shows the right trend in the CdX series, as obtained using Eqn. (3.1). We have also compared our results with those of Abu-Farsakh *et al* [27] calculated for ZB structures. However, their calculated β fails to prove CdS to be more ionic than $CdSe$.

Table 3.5: Bond ionicity β for CdX series in both ZB and WZ structure. Previously reported values of β by Abu-Farsakh *et al* [27] for ZB structure of CdS and $CdSe$ are also listed.

Compounds	Present		Previous (ZB)
	ZB	WZ	
CdS	0.745	0.745	0.740
CdSe	0.739	0.743	0.743
CdTe	0.708	0.714	...

3.6 Summary and Conclusions

Using NMTO-downfolding technique we have revisited the problem of ZB vs WZ symmetry in case of $A^N B^{8-N}$ semiconductors. In particular, we have considered the CdX series with X = S, Se, Te. Our computed ionicity factors using accurate NMTO-downfolding successfully bring out the right trend within the CdX series - CdS being most ionic stabilizes in WZ symmetry while CdSe and CdTe being more covalent stabilizes in ZB symmetry. Bond ionicity measurement from the displacement of the centre of the Wannier function from the bond centre also shows the right trend. Our NMTO constructed Wannier functions corresponding to only valence bands provide nice demonstration of this fact. The tendency towards ZB stability is governed by the covalency which prefers isotropic nature of the tetrahedral bonds.

Bibliography

- [1] *II-VI Semiconductor Compounds*, edited by M. Jain (World Scientific, Singapore, 1993).
- [2] R. W. Birkmire and E. Eser, *Annu. Rev. Mater. Sci.* **27**, 625 (1997).
- [3] W. A. Harrison, *Electronic Structure and the Properties of Solids* (Freeman, San Francisco, 1980).
- [4] J. C. Phillips, *Bonds and Bands in Semiconductors* (Academic, New York, 1973).
- [5] S. Adachi, *Properties of Group-IV, III-V and II-VI Semiconductors* (John Wiley and Sons, Ltd., 2005).
- [6] G. A. Jeffrey, G. S. Parry and R. L. Mozzi, *J. Chem. Phys.* **25**, 1024 (1956).
- [7] F. Keffer and A. M. Portis, *J. Chem. Phys.* **27**, 675 (1957).
- [8] J. C. Phillips and Van Vechten, *Phys. Rev. Lett.* **22**, 705 (1969).
- [9] J. C. Phillips, *Rev. Mod. Phys.* **42**, 317(1970); J. A. Van Vechten, *Phys. Rev.* **187**, 1007 (1969).
- [10] P. Lawaetz, *Phys. Rev. B* **5**, 4039 (1972).
- [11] J. S. John and A. N. Bloch, *Phys. Rev. Lett.* **33**, 1095 (1974).
- [12] A. Zunger and M. L. Cohen, *Phys. Rev. Lett.* **41**, 53 (1978).
- [13] A. Zunger, *Phys. Rev. Lett.* **44**, 582(1980); A. Zunger, *Phys. Rev. B* **22**, 5839 (1980).
- [14] T. Ito, *Jpn. J. Appl. Phys.* **37**, L1217-L1220 (1998).

- [15] N. E. Christensen, S. Satpathy and Z. Pawlowska, *Phys. Rev. B* **36**, 1032 (1987).
- [16] C.-Y. Yeh, Z. W. Lu, S. Froyen and A. Zunger, *Phys. Rev. B* **45**, 12130 (1992); C.-Y. Yeh, Z. W. Lu, S. Froyen and A. Zunger, *Phys. Rev. B* **46**, 10086 (1992).
- [17] E. S. Rittner and J. H. Schulman, *J. Phys. Chem.* **47**, 537 (1943).
- [18] V. A. Fedorov, V. A. Ganshin and Yu. N. Korkishko, *Phys. Stat. Sol.* **126**, K5 (1991).
- [19] M. Kh. Rabadanov, I. A. Verin, Yu. M. Ivanov and V. I. Simonov, *Kristallografiya* **46**, 703 (2001).
- [20] S. A. Semiletov, *Trudy Inst. Kristallogr. Acad. Nauk SSSR* **11**, 121 - 123 (1955) (from ICSD).
- [21] O.K. Andersen and T. Saha-Dasgupta, *Phys. Rev. B* **62**, R16219 (2000) and references there in.
- [22] P. D. Lao, Y. Guo, G. G. Siu and S. C. Shen, *Phys. Rev. B* **48**, 11701 (1993).
- [23] A. W. Stevenson and Z. Barnea, *Acta Cryst.* **B40**, 530 (1984).
- [24] P. E. Blöchl, *Phys. Rev. B* **50**, 17953 (1994).
- [25] *Numerical Data and Functional relationships in Science and Technology*, edited by K. -H. Hellwege and O. Madelung, Landolt-Börnstein, New series, Group III, Vols. 17a and 22a (Springer, New York, 1982).
- [26] N. Marzari and D. Vanderbilt, *Phys. Rev. B* **56**, 12847 (1997).
- [27] H. Abu-Farsakh and A. Qteish, *Phys. Rev. B* **75**, 085201 (2007).

Chapter 4

First principles study of structural stability and electronic structure of CdS nano-clusters

While the structural stability of binary octet semiconductors in bulk phase is well studied (see chapter 3), the situation as the system size is reduced to nano regime is very controversial. The interesting fact about semiconductor nano-particles is that their properties are very much dependent on their size, shape, stoichiometry, nature of passivator used etc. In this chapter, we have carried out a systematic first principles study to investigate the influence of each of the above mentioned factors on structural stability and optical band gap of CdS nano-clusters, for which a number of experimental study are available.¹

4.1 Introduction

In the context of semiconducting nano-clusters, it has been observed that the band gap can be systematically changed over a wide range by tuning the particle size. This tunability of the band gap has opened up immense technological possibilities in diverse fields such as solar cells [1], electroluminescent devices [2] and possible electronic devices. The situation,

¹This chapter is based on the following papers:

- **Soumendu Datta**, Mukul Kabir, Tanusri Saha-Dasgupta and D. D. Sarma, *First principle study of structural stability and electronic structure of CdS nano-clusters*, J. Phys. Chem. C, **112**, 8206 (2008)
- **Soumendu Datta**, Mukul Kabir, Tanusri Saha-Dasgupta and D. D. Sarma, *Study of structural stability and electronic structure of non-stoichiometric CdS nano clusters from first principles*, J. Nanosci. and Nanotechnol., **9**, 1-4 (2009)

however, is complicated by the fact that the reduction in particle size seems to influence the stable crystalline structure of one phase over the other, in a way that is very little understood so far. Among various semiconductor nano-clusters, II-VI semiconductor CdS has received a lot of attention, primarily due to the following facts : (i) CdS is a direct gap semiconductor with rather large band gap of about 2.5 eV [3], (ii) quantum confinement effect can be reached quite easily because of the large excitonic Bohr radius ≈ 3 nm [4], (iii) CdS can be synthesized experimentally rather easily in the size range required for quantum confinement. Though WZ phase is slightly more stable than ZB for bulk CdS, in nano regime, the reported experimental results are quite contradictory : few indicates ZB as stable phase [5] while others in favour of WZ [6, 7] or admixture of WZ and ZB [8]. The structural similarity between WZ and ZB and the associated small differences in cohesive energies on the order of few tens of meV/atom make the situation even more complex and also interesting. This is a crucial issue as band gap, effective mass and other spectroscopic properties are very much dependent on its crystalline phase. However, very little is known about the details of the experimental situation, *e.g.* the stability of non-stoichiometric versus stoichiometric clusters, the role of passivator and their influence on structural stability. Most of the theoretical works in this connection involved studying band gap variation with size of the clusters, using efficient but less accurate parametrized tight-binding approach [9]-[11]. Fig. 4.1 collects together the experimental data [7],[12]-[19] as well as the theoretical results [11] based on tight-binding calculation for band gap variation with size of CdS, CdSe and CdTe nano-clusters. It is interesting to note from this figure that experimental data for CdSe and CdTe nano-clusters shows monotonic variation with size, while they are quite scattered for CdS nano-clusters, specially for smaller sizes which hints towards clusters having different structures at different size regime. While such an interesting issue of relative stability has drawn attention in past and have lead to theoretical analysis based on parametrized tight-binding models [20, 21], to our knowledge no rigorous first-principles study exists to address this issue. In absence of detail knowledge of the experimental scenario which may also vary in different experimental conditions like synthesis route, we considered in this chapter, the *ab-initio* theoretical study of stability of both stoichiometric and non-stoichiometric clusters, naked as well as passivated. Our study shows that the relative

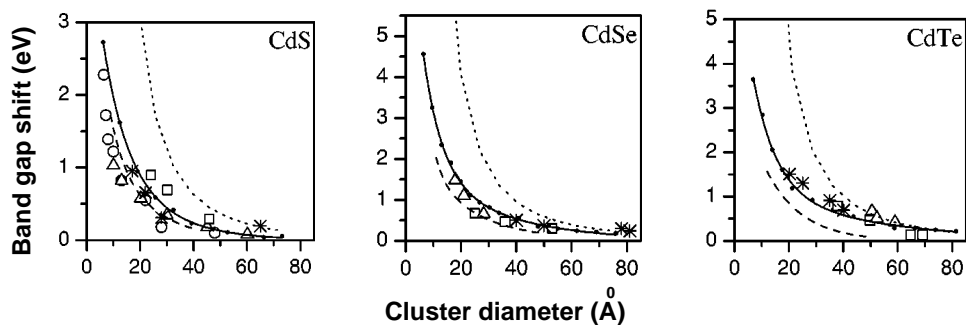


Figure 4.1: Band gap shift as a function of cluster diameter (taken from Ref. [11]). Solid dots fitted with solid line are results for sp^3d^5 TB model with cation-anion and anion-anion interactions, dashed line for sp^3s^* nearest-neighbour TB-model and the dotted line from the effective mass-approximation. Experimental data points:- CdS: open circles from Ref. [7], open triangles from Ref. [12], stars from Ref. [13], open squares from Ref. [8]; CdSe: open squares from Ref. [14], open triangles from Ref. [15], stars from Ref. [16]; CdTe: open squares from Ref. [17], open triangles from Ref. [18], stars from Ref. [19]

stability between WZ-structured and ZB-structured clusters are governed by the details of surface geometry and surface chemistry. In case of passivated clusters, we have also studied the associated band gap as a function of cluster size which depending on specific case also shows highly non-monotonic behaviour.

4.2 Building up of clusters

It is important to note that the stable phase seems to depend on the shape of the nanocrystal [22], with majority of the experimental results being for spherical nano-clusters. So we will focus on only spherical nano-particles. To generate nano-cluster of geometry closest to spherical shape, we have built up the cluster shell by shell. To generate non-stoichiometric clusters, we have taken the cluster centre on a Cd atom or S atom. In both ZB and WZ structures, each Cd(S) atom is tetrahedrally surrounded by S(Cd) atoms in its immediate neighbourhood [23]. Therefore, the surface of a non-stoichiometric cluster, generated via above-mentioned prescription contains only single species of atoms : a non-stoichiometric nano-cluster of even number of shells has same kind of atoms at the surface and at the centre, while a non-stoichiometric nano-crystal with an odd number of

Table 4.1: Number of atoms and diameters of both stoichiometric and non-stoichiometric CdS clusters listed in order of increasing shell sizes for wurtzite structure. The corresponding values for the zincblende structure are shown within parenthesis.

Shell no.	Stoichiometric		Non-stoichiometric	
	N	diameter(Å)	N	diameter(Å)
1	8 (8)	7.57 (7.21)	5 (5)	6.47 (6.16)
2	26 (26)	11.21 (10.68)	17 (17)	9.73 (9.27)
3	58 (56)	14.65 (13.79)	42 (41)	13.15 (12.43)
4	114 (110)	18.35 (17.27)	86 (83)	16.70 (15.72)
5	192(184)	21.83(20.50)	153(147)	20.24(19.02)
6	306(294)	25.50(23.97)	249(239)	23.80(22.37)

shells has two dissimilar types of atoms at the centre and at the surface. On the other hand, stoichiometric clusters are generated by putting the centre of the cluster on the midpoint of Cd-S bond. In this case, each shell contains equal number of Cd atoms and S atoms. Assuming spherical shapes, the diameters of ZB and WZ clusters of N atoms are given by, $d_{ZB} = \left[\frac{3N}{4\pi}\right]^{\frac{1}{3}} a_{ZB}$ and $d_{WZ} = \left[\frac{3N}{2\pi}a^2c\right]^{\frac{1}{3}}$ where a and c are the lattice constants for wurtzite structure in the ab -plane and along the c -axis, respectively. In Table 4.1, we list the cluster sizes in order of increasing shell numbers for both stoichiometric and non-stoichiometric clusters.

4.3 Computational Details

We have carried out first principles electronic structure calculation within the framework of DFT for the constructed nano-clusters. We have used PAW pseudopotential with plane-wave basis and LDA for the exchange-correlation functional as implemented in VASP code. The kinetic energy cut-off of the plane waves used in the calculations is 280 eV which gives convergence of total energy sufficient to discuss the relative stability of various phases. One useful parameter for comparing the stability of clusters is the cohesive energy per

atom, defined as

$$E_c = \frac{\sum_{\beta} n_{\beta} E_{\beta} - E_{tot}}{\sum_{\beta} n_{\beta}} \quad (4.1)$$

E_{tot} being the total energy of the cluster, E_{β} being the energy of an isolated β atom ($\beta = \text{Cd}, \text{S}$) and $n_{\beta} =$ number of either type of atoms in the cluster. To check the validity of our calculations, we computed the cohesive energy of bulk WZ and ZB CdS. Our computed values of 2.653 eV/atom for the cohesive energy of WZ CdS and 9.7 meV/atom for ZB - WZ energy difference agree well with published results [24]. Finite size cluster calculations were carried out using the super-cell technique where a finite sized cluster is positioned within a cubic super-cell. The cell dimension is set by the condition that each repeated cluster in the periodic lattice is separated by a vacuum layer of at least 12 Å, large enough so as to avoid the interaction between the clusters. To check the effect of optimization of geometry in certain specific cases, we relaxed the surface atoms keeping the core of the cluster fixed at ZB or WZ symmetry. This is a reasonable approach, considering the fact that previous studies where relaxation has been carried out for the entire cluster [20], showed that the structural relaxation was mostly confined to the surface layer. Relaxations are performed using conjugate gradient and quasi-Newtonian methods until all the force components are less than a threshold value 0.01 eV/Å. The reciprocal space integration in all cases have been carried out with Γ point which is justified by the large dimension of the cubic super-cell.

In order to study the role of passivator on the structural stability problem and the band gap problem we have also considered *ab-initio* calculations in presence of passivators. The surface of a naked semiconductor nano-particle often contains electronically active states because of unsaturated surface bonds or dangling bond states. Surface passivation aims to rebond these dangling bonds with some passivating agent while maintaining the local charge neutrality of the whole system. In experiment, organic molecules are often used to passivate nano-clusters. Owing to the complexities and the numerous degrees of freedom of these passivation agents, it is not easy to do calculation with such passivators. To mimic the role of passivator in *ab-initio* calculation, several simpler atomistic models have been proposed [25, 26]. We will follow the recipe by Huang *et al* [26], which is applicable for both stoichiometric as well as non-stoichiometric clusters. The proposed recipe requires the use of two different kind of fictitious hydrogen atoms, H^* , to passivate the dangling

bonds of CdS nano-clusters. To keep the passivated cluster neutral, one species of the fictitious atoms is chosen to have a nuclear charge of $1+\eta$ and valance electron charge of $-(1+\eta)$, where η is a positive number. These atoms are bonded with Cd atoms. The other species of atoms is chosen to have a nuclear charge of $1-\eta$ and a valance electron charge of $-(1-\eta)$. These atoms are bonded to the S atoms. One needs to choose a value of the fractional charge, η , that will optimally passivate the clusters, *i.e.*, for all considered sizes of the nano-clusters, the chosen η has to be same. This is found to be satisfied when the gap becomes a maximum, as pointed out in Ref. [26]. The value of η for which gap is maximum in the curve of gap vs η , is found to be 0.5 for II-VI semiconductor nanoparticles [26]. The bond lengths of H^* -Cd and H^* -S were determined from two model systems, CdH_4^* and SH_4^* , in which bond lengths are fully optimized. The orientation of H^* around Cd and S is fixed in the same tetrahedral orientation as it is in ZB or WZ structure.

4.4 Results

4.4.1 Energy stability

Unpassivated stoichiometric clusters

Fig. 4.2a shows the plot of the computed cohesive energy for unpassivated stoichiometric clusters as a function of growing cluster size. The cohesive energy shows an overall increase with the increase of cluster size for both the ZB and WZ structures due to the reduction in the ratio of surface atoms to bulk atoms upon increasing cluster size. However, the variation of cohesive energy is found to be non-monotonic with increasing size. Connecting the cohesive energies of all the even shell clusters and that of odd shell clusters separately, we find that the even shell clusters show higher cohesive energy (and therefore better binding) than the odd shell clusters. Further to study the relative stability between the ZB and WZ symmetry, we show in Fig. 4.2b, the cohesive energy difference between WZ and ZB structures at each shell size. Whenever the quantity plotted is negative, it implies that the cubic structure is more stable, while a positive value signals the hexagonal structure as the stable phase. Our results, as plotted in Fig. 4.2b, show a general trend

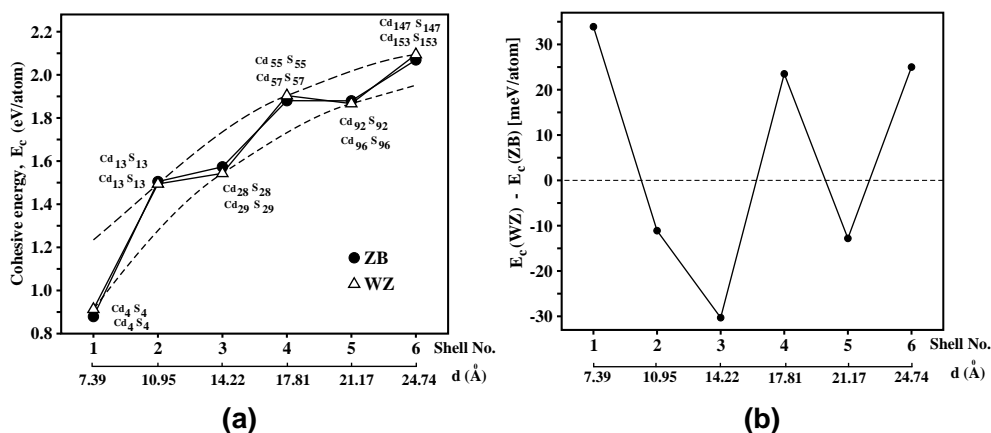


Figure 4.2: (a) Variation of cohesive energy with size for unpassivated stoichiometric clusters shown by solid dots in ZB structure and by open triangles in WZ structure. Chemical formula for each shell is given both in ZB (upper) and WZ (lower) structures. (b) The cohesive energy difference between WZ and ZB structures for each shell size in the case of unpassivated stoichiometric clusters. For a particular shell number, the diameter of the ZB and WZ structured cluster differ a bit (cf. Table 4.1), therefore the average diameter is shown in the x -axis of the plot. Same convention is followed in all the following plots wherever applicable.

that from 3 shell onwards, the odd shell clusters stabilize in cubic ZB structure, while all even shell clusters prefer to form in hexagonal WZ structure. To check the robustness of our result with respect to structural relaxations of the surface atoms, we have also carried out structural relaxation of the surface atoms for 3-shell and 4-shell stoichiometric nanoclusters, keeping the position of core atoms fixed in ZB or WZ geometry, as explained in section 4.3. Although the quantitative values change somewhat (by about 4-10 meV), the trend remains the same, *i.e.* cluster with odd number of shells like 3-shell stabilizes in cubic ZB structure and with even number of shells like 4-shell stabilizes in WZ structure. This is in accordance with the finding by Joswig *et al* [20] that total energy upon relaxation of such clusters reduces only little.

In order to understand the oscillating stability of the WZ and ZB structures and also the higher stability of the even shell clusters compared to odd shell clusters in general, we have analyzed the different contributions to the total energy. For finite sized cluster, surface effect is important and the surface energy contribution to the total free energy

plays the dominant role in determining the stable phases. In Fig. 4.3 we show the surface energy variation as a function of the cluster size, where the surface energy per atom is defined as,

$$\frac{N\epsilon^{bulk} - E^{clus}}{N_s}$$

E^{clus} being the total cohesive energy of the cluster, N being the total number of atoms in the cluster, N_s being the number of surface atoms, and ϵ^{bulk} being the bulk cohesive energy per atom. We find that even shell clusters have lower surface energy and hence more binding compared to odd shell clusters. The inset of Fig. 4.3 shows the surface energy difference between WZ and ZB structures for each shell size. The positive (negative) value of surface energy difference means WZ structure has higher (lower) surface energy contribution than ZB structure and therefore WZ structure is less (more) stable. This trend in surface energy variation and that of its difference is in accordance with the trend found in the cohesive energy and its difference. Furthermore, to understand the

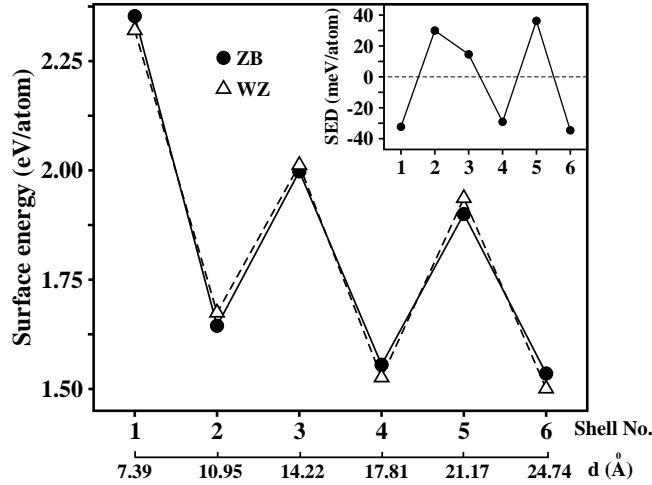


Figure 4.3: Variation of surface energy with cluster size for ZB (solid dots) and WZ (open triangles) structures for stoichiometric clusters. The inset shows the surface energy difference (SED) between WZ and ZB structures.

non-monotonic behaviour in surface energy or cohesive energy as a function of cluster size, we calculated the average number of dangling bonds per surface atom. The number

of dangling bonds are the total number of unsaturated bonds, defined as $\sum_i(4 - z_i)$, where z_i is the coordination of i -th surface atom and the summation over i involves summation over all surface atoms for a particular cluster size. We find that the average number of dangling bonds are larger for odd shell clusters, giving rise to increased surface states and hence larger surface energy contribution, thereby explaining the non-monotonic behaviour of cohesive energy. While non-monotonic behaviour of cohesive energy has been reported in theoretical calculations in past [20], such systematic behaviour and its analysis by application of accurate first-principles calculations, to our knowledge has not been demonstrated before. The analysis in terms of dangling bonds not only explains the higher stability of the even shelled clusters, but also explains the relative stability of WZ and ZB structured clusters since the difference of average number of dangling bonds per surface atom between WZ and ZB structured clusters oscillates between positive and negative values, being positive for odd shelled clusters and negative for even shelled clusters. The difference is zero for 1 and 2-shelled clusters since the local co-ordination of immediate neighbours is identical between ZB and WZ clusters and the difference shows up only beyond 2nd nearest neighbour.

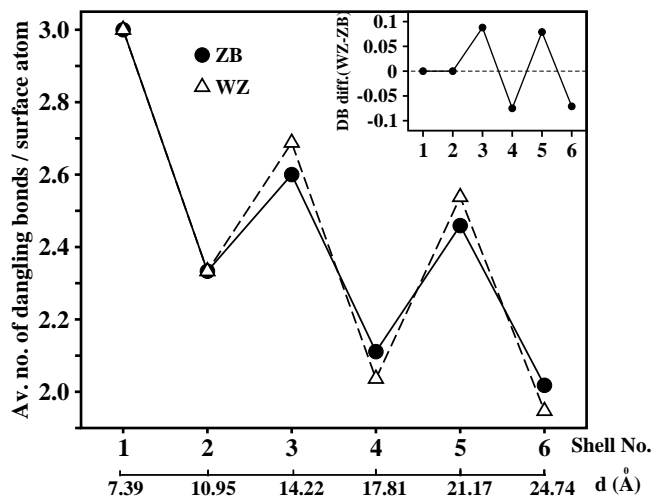


Figure 4.4: Average number of dangling bonds (DB) per surface atom for unpassivated stoichiometric clusters in ZB (solid dots) and WZ (open triangles) structures. The inset shows difference between WZ and ZB structures.

Unpassivated non-stoichiometric clusters

Most experimental condition favours synthesise of clusters of non-stoichiometric nature. It is therefore important to consider clusters having non-stoichiometric composition. This however leads to complication due to the fact that different cluster sizes have very different Cd to S ratio, making the comparison of corresponding total energies a difficult task for which no obvious way exists. However, for a given shell, the Cd to S ratio between ZB and WZ structured clusters remains almost same [27] making the comparison of their cohesive energy meaningful. In Fig. 4.5 we plot the difference in cohesive energy between the WZ and ZB structured non-stoichiometric clusters as a function of increasing cluster size. Fig. 4.5a exhibits the cohesive energy differences for Cd centred clusters and Fig. 4.5b that of S centred clusters. We note that unlike the case of stoichiometric clusters where the surface

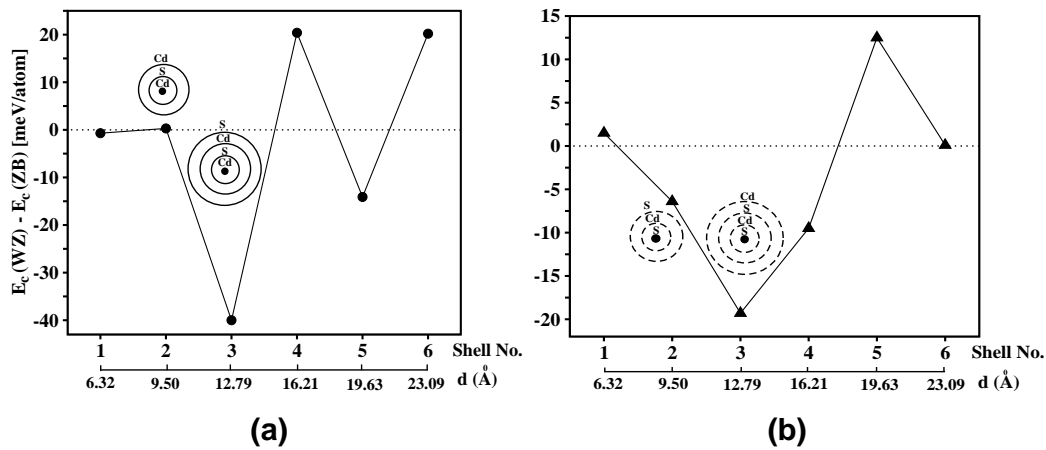


Figure 4.5: Cohesive energy difference between WZ and ZB structures for each shell size in case of unpassivated non-stoichiometric clusters. (a) Solid dots connected with solid line represent the results for Cd-centred clusters, while (b) the solid triangles connected with solid line correspond to results for S-centred clusters. The consecutive layers of atoms for 2 shell and 3 shell clusters have been shown for both Cd-centred case (spheres with solid line) and S-centred case (spheres with dashed line). Note, by construction even shell Cd(S)-centred cluster is Cd(S) terminated and odd shell Cd(S)-centred cluster is S(Cd) terminated (see text).

composition always consists of equal number of S and Cd, for non-stoichiometric clusters

the surface is formed exclusively by either S or Cd atoms. For Cd-centred clusters, the even (odd) shell clusters are Cd (S) terminated, while it is reversed for S-centred clusters. From the plot in Fig. 4.5, we find that non-monotonic behaviour of the relative stability between WZ and ZB phase persists, on top it shows additional interesting aspect in the sense that whether an even or odd shell cluster is formed in WZ or ZB symmetry depends on the terminating layer. Focusing on clusters with shell numbers 4 and 5 in Fig. 4.5a, 4 shell cluster is found to be WZ structured and 5 shell clusters is found to be ZB structured for Cd-centred cluster while moving to the Fig. 4.5b, the reverse trend is found for the S-centred clusters. We note that a 4 (5) shell cluster is Cd (S) terminated in the former cases and S (Cd) terminated in the latter cases. As expected this is driven by the oscillating behaviour of the surface energy difference between WZ and ZB structures (shown in Fig. 4.6), which shows the similar trend as observed in case of the cohesive energy difference. However unlike the case of stoichiometric clusters, this trend is not explained by the

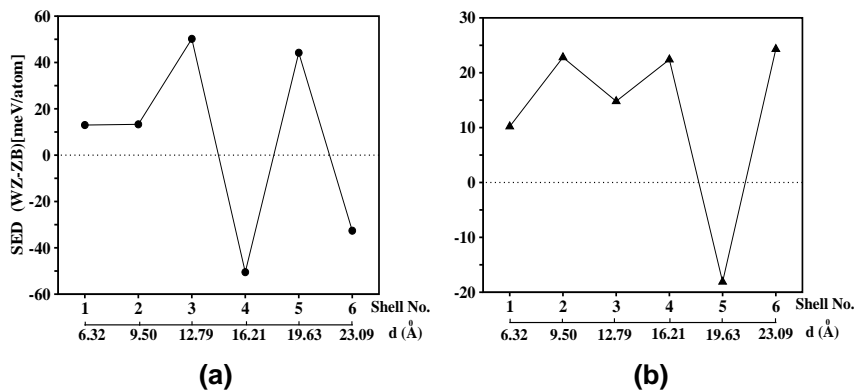


Figure 4.6: Variation of surface energy difference (SED) between WZ and ZB structures, with increasing shell sizes in (a) Cd-centred (represented by solid dots) and (b) S-centred (represented by solid triangles) non-stoichiometric clusters.

difference in the average number of dangling bonds per surface atom between WZ and ZB structured clusters (shown in Fig. 4.7). The difference in average number of dangling bonds predicts that the surface energy of a 4-shell ZB structured cluster to be higher than that of a WZ structured cluster, hence a 4 shell cluster must form in WZ structure which is indeed the case for 4 shell Cd-centred cluster but not for 4 shell S-centred cluster. We therefore conclude that an additional effect is operative in case of non-stoichiometric

cluster, namely the surface chemistry effect. The surface chemistry effect adds on the surface geometry effect in case of Cd centred clusters, while it acts in an opposite way to that of surface geometry effect in case of S centred clusters, thereby reversing the trend in the sense odd shell clusters are now stabilized in WZ structure and even shell clusters are stabilized in ZB structure. The relative stability between WZ and ZB structures in case of non-stoichiometric clusters, is driven dominantly by the surface chemistry rather than the surface geometry as has been found in case of stoichiometric clusters.

In order to investigate the microscopic reasons associated with the surface that drives

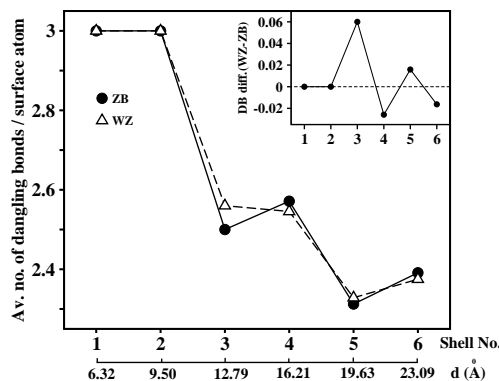


Figure 4.7: Average number of dangling bonds per surface atom (DB) for non-stoichiometric CdS clusters in ZB and WZ structures. The inset shows the difference between WZ and ZB structures. Plot is independent of whether the clusters are Cd-centred or S-centred.

this effect, we have computed the average charge enclosed within a sphere around a Cd atom and that around an S atom within a given cluster. There is no unique way to divide space in an AB compound into A and B regions. Therefore, two choices of sphere radius have been made : in one case, the spheres were taken to be equal sized with radius as half the Cd-S bond length, in another case the choice of sphere radius was guided by the Hartree plot of the potential. We carried out calculations for Cd-terminated nano-clusters and S-terminated nano-clusters as well as for that of the bulk with both ZB and WZ structures in every case. The following results emerge from these calculations independent of the structure type. While the Cd-terminated clusters show similar charge distributions as those of bulk, S-terminated clusters show about 0.2 fraction

of less electronic charge enclosed within the spheres. This is found to be true for both choices of sphere radii. This, in turn, would indicate covalency to be stronger in case of S-terminated clusters resulting into significant amount of charge residing in the interstitial region between Cd and S-centred spheres. This is illustrated in Fig. 4.8, which shows the charge density distribution ($\delta\rho$) around a surface S atom, and that around a surface Cd atom for a 4-shell non-stoichiometric cluster, after subtracting the charge density of the isolated atom (ρ_a) and that of the system without the chosen atom (ρ_s) from the actual system (ρ_t). While Cd terminated cluster shows hardly any change in the region of Cd-S bond, there is a significant accumulation of charge around the Cd-S bond in case of S-terminated cluster. This provides a clear evidence for an enhanced covalency and, therefore, reduced ionicity in case of S-terminated cluster resulting into increased stability of ZB phase over the WZ phase. In this context, it is interesting to point out from our work of chapter 3 that the stability of the two competing crystal phases, namely ZB and WZ, changes systematically for the bulk systems, CdS, CdSe and CdTe. While CdS has the WZ structure, CdTe is known to have the ZB form which has indeed been explained in terms of increased covalency. This is consistent with the present observation of ZB structure for CdS nano-crystal being stabilized in presence of a S-terminating layer which is also substantially more covalent.

Passivated stoichiometric clusters

In realistic situation, the clusters are grown in presence of some passivating agent. Although ideally the role of the passivator is to restrict the growth of the cluster by saturating the unpassivated dangling bonds, which opens up a clear gap in the energy spectrum without supposedly changing the intrinsic properties of the clusters, it may also influence the energy stability of the cluster itself. This is however very complicated and rather unexplored issue due to the complexity of various passivating agents used in experiments. A good understanding of the atomic structure of such complex passivating agents like triethylphosphine (TOP) or triethylphosphine oxide (TOPO) in many cases is unavailable and it is almost impossible to deal with such large complexes within an accurate first-principles approach. Very often, therefore fictitious H atoms are used in theoretical calculations for the purpose of passivation. In absence of any other well-defined procedure

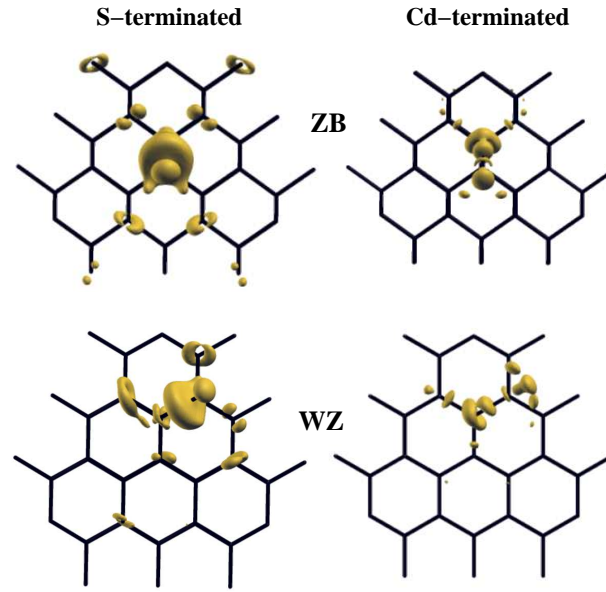


Figure 4.8: Charge density contribution ($\delta\rho = \rho_t - \rho_a - \rho_s$) around a surface atom of 4-shell non-stoichiometric CdS nano-clusters. The isosurface is chosen at $.007 e^- / (\text{\AA}^3)$.

we have therefore considered the passivation by fictitious H atoms as explained in section 4.3 and in the following have studied the effect of the passivation on both stoichiometric and non-stoichiometric clusters. In Fig. 4.9, we show the computed density of states of a representative stoichiometric CdS cluster with 4 shell and ZB structure in absence and presence of passivation. We note that assumed passivation could successfully remove the states close to Fermi energy, opening up a gap of about 1.5 eV. Similar results are obtained for clusters with other different shell structures and also with WZ symmetry. Having been convinced about the proper functioning of the passivator, in Fig. 4.10 we show the variation of the cohesive energy differences between the WZ and ZB structured stoichiometric CdS nano-clusters as a function of increasing cluster size. Interestingly we note, that the oscillating behaviour of the relative stability between WZ and ZB structured clusters observed for naked stoichiometric clusters survives even in presence of passivation, in the sense the even shelled clusters favour the WZ structure and the odd shell clusters favour the ZB structure. This presumably is driven by the fact that the difference in number of bonds with fictitious H atoms between WZ and ZB structures oscillates as a function

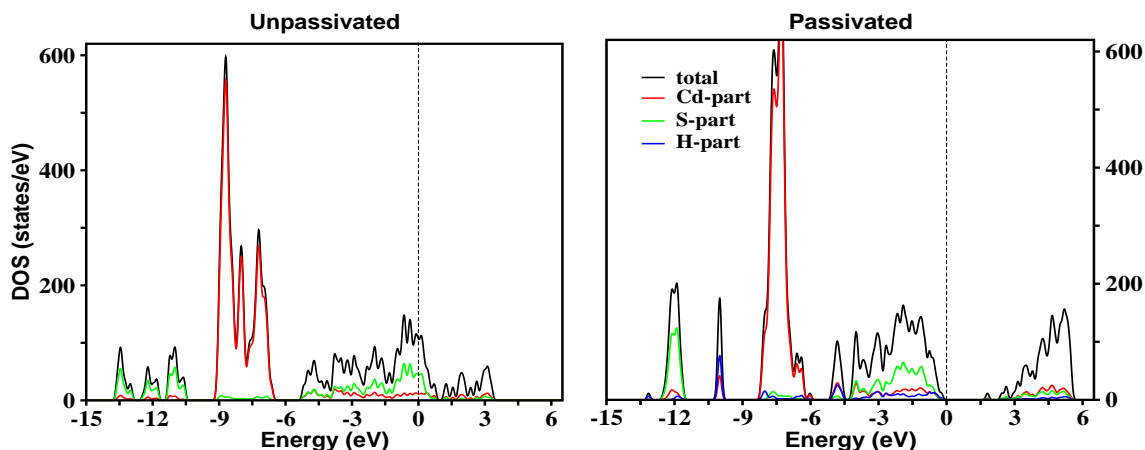


Figure 4.9: Density of states for 4 shell ZB structured stoichiometric cluster. Left panel shows the DOS for unpassivated cluster while the right panel shows the DOS for passivated cluster. Black, red, green and blue lines correspond to total DOS, Cd-contribution, S-contribution and that of H-contribution (in case of passivated cluster only) respectively.

of increasing cluster size. As already stated, we have followed in the above a simplified treatment of passivating agent, the situation in presence of realistic passivators need to be explored, which however is beyond the scope of our present study.

Passivated non-stoichiometric clusters

In this section, we focus on non-stoichiometric clusters and the role of passivation in this class of clusters. The passivation has been done following the same prescription as in case of stoichiometric clusters. Fig. 4.11 shows the density of states plot for a representative non-stoichiometric cluster in absence and presence of passivator. As found in case of stoichiometric clusters, the passivator removes the surface states appearing close to Fermi energy in the unpassivated case and shifts them away from Fermi energy, thereby opening up a clear gap at the Fermi energy. The corresponding variation in the relative stability of the WZ and ZB structures for the passivated non-stoichiometric clusters are shown in Fig. 4.12.

The left panel shows the data for Cd-centred clusters while the right panel shows the data for S-centred clusters. The chosen scheme of passivation seems to have a pronounced

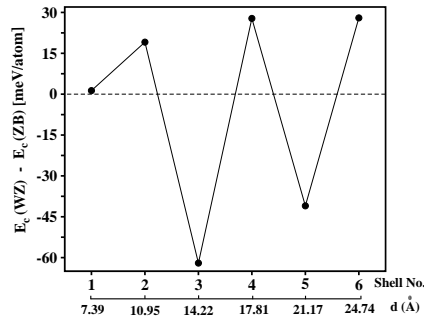


Figure 4.10: Variation of cohesive energy difference between WZ and ZB structures with size for passivated stoichiometric clusters.

effect for the non-stoichiometric clusters in the sense apart from very small clusters, the tendency towards formation in ZB phase seemingly is found to be higher than that in WZ phase in general, irrespective of even or odd number of shell, and terminating layer, although in some cases the energy difference is indeed tiny (within 1-2 meV) and is within the calculational accuracy. For the non-stoichiometric clusters, study of realistic passivators will be even more interesting since in many cases the passivating agent itself may have S/Cd content, giving rise to preferential S or Cd termination of the synthesized clusters.

4.4.2 Band Gap Variation with cluster size

The study of CdS clusters in presence of passivator also allows us to investigate the variation of the band gap as a function of increasing cluster size. In Figs. 4.13 and 4.14, we show the computed band gaps of the ground state structures of passivated clusters at each shell size, for stoichiometric and non-stoichiometric clusters, respectively. The insets show the corresponding individual variations of the highest occupied molecular orbital (HOMO) and lowest unoccupied molecular orbital (LUMO). It is to be noted that CdS being a direct gap semiconductor, the band gaps of WZ and ZB phases are expected to be similar [28], irrespective of stable phase as ZB or WZ. As expected, the calculated band gap shows an overall decrease as a function of increasing cluster size due to the well known quantum confinement effect, asymptotically approaching the bulk band gap value in the

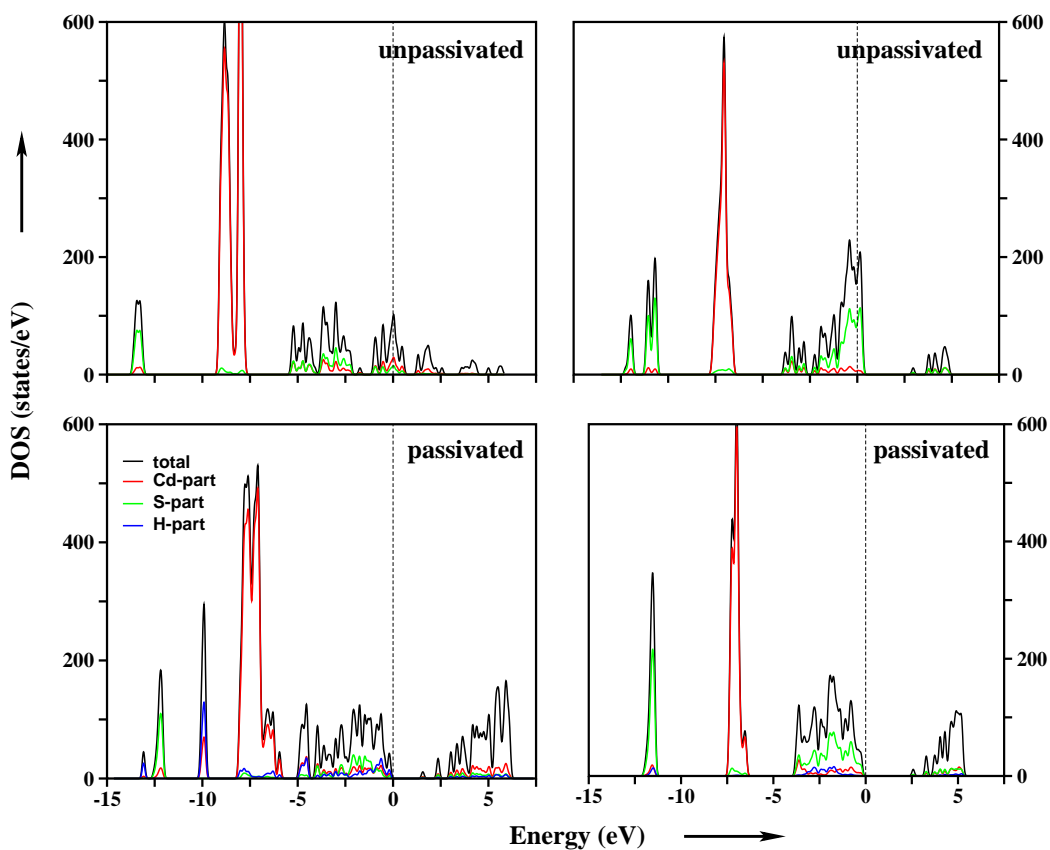


Figure 4.11: DOS for 4 shell Cd-centred (left panels) and S-centred (right panels) ZB non-stoichiometric cluster. Upper panels correspond to unpassivated case while bottom panels correspond to passivated case. Black, red, green and blue lines correspond to total DOS, Cd-contribution, S-contribution and that of H-contribution (in case of passivated cluster only) respectively.

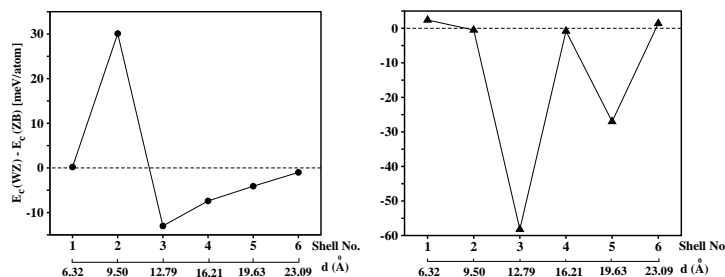


Figure 4.12: Variation of cohesive energy difference between WZ and ZB structures with size for passivated Cd-centred (left panel) and S-centred (right panel) non-stoichiometric clusters.

limit of the infinite cluster size. The calculated band gap for the clusters are systematically underestimated due to the over-binding problem related with LDA treatment of exchange-correlation functional. For non-stoichiometric clusters, the band gap variation is found to be highly non-monotonic. The scattered experimental data for CdS nano-clusters in Fig. 4.1 may be suggestive of this effect. The odd shell clusters for Cd-centred clusters and the even shell clusters for S-centred clusters show significantly higher value of band gap compared to their respective counterparts. We therefore conclude that the S-terminated clusters in general show larger band gap compared to Cd-terminated clusters. As is evident from the variation of HOMO and LUMO energies shown in the inset, this oscillation is primarily contributed by the oscillation in the LUMO. The origin of such a behaviour lies in the density of states of the unpassivated cluster itself. Comparing the density of states of Cd-terminated and S-terminated non-stoichiometric clusters as shown in left and right panels of Fig. 4.11, we found that while for S-terminated DOS, there exists a well-defined gap in the unoccupied part of the spectrum, the situation is very different in case of Cd-terminated cluster. The spectrum is practically gap less or with very small gap in the unoccupied region. Inclusion of passivating atom, changes the unoccupied spectra drastically in case of Cd-terminated cluster, while the unoccupied spectra apart from the removal of the states very close to Fermi energy changes only modestly in case of S-terminated clusters. We note that, for a non-stoichiometric Cd-rich CdS cluster, the nominal valences of Cd and S deviate from that in bulk, which results in the formation of fewer CdS anti-bonds compared to that of bulk. The pushing up of Cd dominated

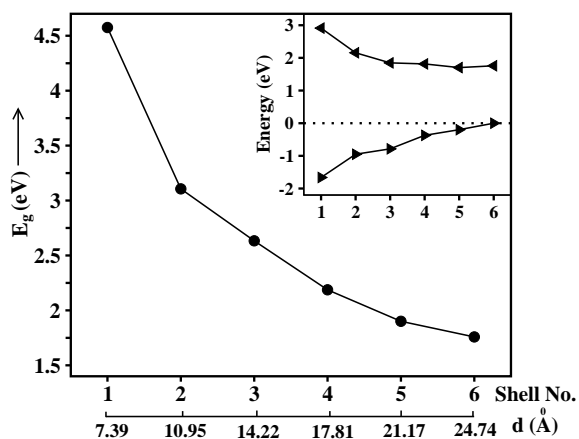


Figure 4.13: Calculated band gaps of the ground state structures at each shell size for stoichiometric clusters. Inset shows the positions of HOMO (solid right triangles) and LUMO (solid left triangles) with respect to HOMO of 6th shell cluster, as a function of cluster size.

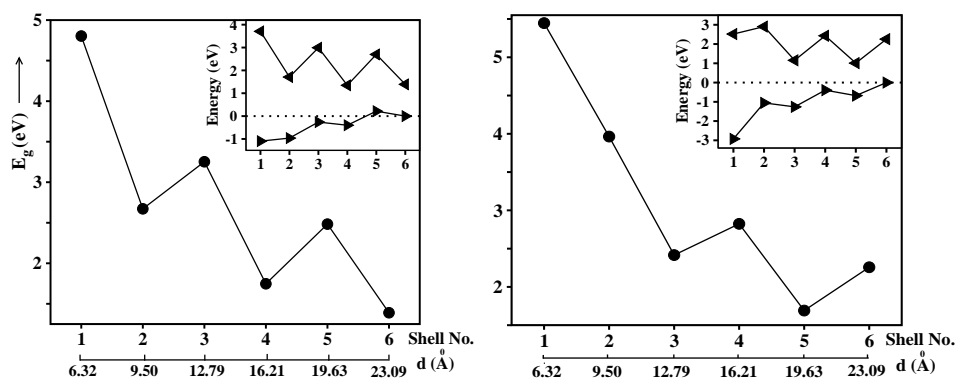


Figure 4.14: Calculated band gaps of the ground state structures at each shell size for non-stoichiometric clusters. Left and right panels show the results for Cd-centred and S-centred clusters respectively. Insets show the positions of HOMO (solid right triangles) and LUMO (solid left triangles) with respect to HOMO of 6th shell cluster, as a function of cluster size.

bands due to formation of anti-bonds therefore does not happen, thereby aligning the Cd-dominated bands about the same energy position as that of elemental Cd.

4.5 Summary and Conclusions

Using first-principles density functional based calculations employing plane wave basis set we present an extensive study of the energy stability and the band gap variation in CdS clusters. In particular, we have considered the relative stability between ZB and WZ structures. In order to explore the varied experimental conditions, we have considered non-stoichiometric as well as stoichiometric clusters, in absence and presence of passivating atoms. Our study shows that the relative stability depends crucially on the surface structure, both geometry and chemistry depending on the specific cases. This may give rise to highly non-monotonic behaviour of the relative stability as a function of the growing cluster size. The band gap variation for the non-stoichiometric clusters is also found to exhibit strong oscillation.

Bibliography

- [1] R. J. Ellingson, M. C. Beard, J. C. Johnson, P. Yu, O. I. Micic, A. J. Nozik, A. Shabaev, and A. L. Efros, *Nano Lett.* **5**, 865 (2005).
- [2] S. Coe, W.-K. Woo, M. G. Bawendi, and V. Bulovic, *Nature (London)* **420**, 800 (2002).
- [3] B. S. Zou, R. B. Little, J. P. Wang and M. A. El-Sayed, *Int. J. Quantum Chem.* **72**, 439 (1999).
- [4] L. R. Brus, *Chem. Phys.* **80**, 4403 (1984).
- [5] R. Rossetti, J. L. Ellison, J. M. Gibson, and L. E. Brus, *J. Chem. Phys.* **80**, 4464 (1984); Y. Wang, A. Suna, and J. McHugh, *J. Chem. Phys.* **92**, 6927 (1990); N. Herron, Y. Wang, and H. Eckert, *J. Am. Chem. Soc.* **112**, 1322 (1990); R.J. Bandaranayake, G. W. Wen, J. Y. Lin, H. X. Jiang and C. M. Sorensen, *Appl. Phys. Lett* **67**, 831 (1995); C. Ricolleau, L. Audinet, M. Gandais, and T. Gacoin, *Eur. Phys. J. D* **9**, 565 (1999); R. Banerjee, R. Jayakrishnan and P. Ayyub, *J. Phys.: Condens Matt.* **12**, 10647 (2000); G. Z. Wang, W. Chen, C. H. Liang, Y. W. Wang, G. W. Meng and L. D. Zhang, *Inorg. Chem. Commun.* **4**, 208 (2001); Y. Charles Cao and J. Wang, *J. Am. Chem. Soc.* **126**, 14336 (2004).
- [6] C.B. Murray, D. J. Norris and M. G. Bawendi, *J. Am. Chem. Soc.* **115**, 8706 (1993); T. Vossmeier, L. Katsikas, M. Giersig, I. G. Popovic, K. Diesner, A. Chemseddine, A. Eychmueller, H. Weller, *J. Phys. Chem.* **98**, 7665(1994); W. Vogel, and J. Urban, *Langmuir* **13**, 827 (1997).

- [7] T. Vossmeier, L. Katsikas, M. Giersig, I. G. Popovic, K. Diesner, A. Chemseddine, A. Eychmuller, and H. Weller, *J. Phys. Chem.* **98**, 7665 (1994).
- [8] J. Nanda, B. A. Kuruvilla, and D. D. Sarma, *Phys. Rev. B* **59**, 7473 (1999).
- [9] P. E. Lippens and M. Lannoo, *Matter. Sci. Eng.* **B9**, 485 (1991).
- [10] R. Viswanatha, S. Sapra, T. Saha-Dasgupta, and D. D. Sarma, *Phys. Rev. B* **72**, 045333 (2005) and references therein.
- [11] S. Sapra, and D. D. Sarma, *Phys. Rev. B* **69**, 125304 (2004).
- [12] Y. Wang, and N. Herron, *Phys. Rev. B* **42**, 7253 (1990).
- [13] T. Torimoto, H. Kontani, Y. Shibusaki, S. Kuwabata, T. Sakata, H. Mori, and H. Yoneyama, *J. Phys. Chem. B* **105**, 6838 (2001).
- [14] B. O. Dabbousi, C. B. Murray, M. F. Rubner, and M. G. Bawendi, *Chem. Mater.* **6**, 216 (1994).
- [15] A. L. Rogach, A. Kornowski, M. Gao, A. Eychmuller, and H. Weller, *J. Phys. Chem. B* **103**, 3065 (1999).
- [16] S. Gorer, and G. Hodes, *J. Phys. Chem.* **98**, 5338 (1994).
- [17] Y. Mastai, and G. Hodes, *J. Phys. Chem. B* **101**, 2685 (1997).
- [18] Y. Masumoto, and K. Sonobe, *Phys. Rev. B* **56**, 9734 (1997).
- [19] H. Arizpe-Chrez, R. Ramirez-Bon, F. J. Espinoza-Betn, O. Zelaya-Angel, J. L. Marn, and R. Riera, *J. Phys. Chem. Solids.* **61**, 511 (2000).
- [20] J.-O. Joswig, M. Springborg, and G. Seifert, *J. Phys. Chem. B* **104**, 2617 (2000); J.-O. Joswig, S. Roy, P. Sarkar, and M. Springborg, *Chem. Phys. Lett.* **365**, 75 (2002).
- [21] B. Goswami, S. Pal, P. Sarkar, G. Seifert, and M. Springborg, *Phys. Rev. B* **73**, 205312 (2006); P. Sarkar, and M. Springborg, *Phys. Rev. B* **68**, 235409 (2003); S. Roy and M. Springborg, *J. Phys. Chem. B* **107**, 2771 (2003).

- [22] B. A. Simmons, S. Li, V. T. John, G. L. McPherson, A. Bose, W. Zhou, and J. He, *Nano Lett.* **2**, 263 (2002).
- [23] In case of WZ structure, due to different values of in-plane and out-of-plane lattice constants, a and c , one of the nearest neighbours has slightly different distance compared to rest three.
- [24] C.-Y. Yeh, Z.W.Lu, S.Froyen and Alex Zunger, *Phys.Rev. B* **46**, 10086 (1992).
- [25] L.-W. Wang and A. Zunger, *Phys. Rev. B* **53**, 9579 (1996); E. Rabani, B. Hetenyi, B. J. Berne, and L. E. Brus, *J. Chem. Phys.* **110**, 5355 (1999); K. Shiraishi, *J. Phys. Soc. Jpn.* **59**, 3455 (1990); L.-W. Li and J. Li, *Phys. Rev. B* **69**, 153302 (2004).
- [26] X. Huang, E. Lindgren and J. R. Chelikowsky, *Phys.Rev. B* **71**, 165328 (2005).
- [27] For a given shell, the Cd to S ratio being same for both the ZB and WZ structures, the degree of non-stoichiometry is also same for both the structures. Only for 3 shell clusters, the Cd to S ratio differs by 3% between ZB and WZ structures.
- [28] C.-Y. Yeh, S.-H. Wei and A. Zunger, *Phys. Rev. B* **50**, 2715 (1994).

Chapter 5

Interplay of structure and magnetism in pure cobalt clusters Co_n ($n = 2-20$)

In this chapter we study the structural, electronic and magnetic properties of Co_n clusters ($n = 2-20$) using DFT within the pseudopotential plane wave method. The cobalt atoms are ferromagnetically ordered and the calculated magnetic moments are found to be higher than that of corresponding hcp bulk value, which are in good agreement with the recent Stern-Gerlach experiments. An unusual hexagonal growth pattern has been observed in the ground state structures, unlike the clusters of other two $3d$ transition metals Mn and Fe which prefer icosahedral growth pattern. ¹

5.1 Introduction

With the advance of modern technology, it is now possible to produce and to do measurements on *small* metal clusters of a few atoms. Magnetic moment measurements on small clusters of transition metal elements have already shown several unexpected behaviours. For example, Cox and co-workers found non-zero magnetic moment in the bare Rh clusters for sizes less than 60 atoms [1], though the bulk Rh is a Pauli paramagnet at all temperatures. Clusters of ferromagnetic materials show enhancement of magnetic moment as compared to their bulk values [2]-[7]. Finite magnetic moments have been

¹This chapter is based on the following paper:

Soumendu Datta, M. Kabir, S. Ganguly, B. Sanyal, T. Saha-Dasgupta and A. Mookerjee; *Structure, bonding and magnetism of cobalt clusters from first-principles calculations*, Phys. Rev. B, **76**, 014429 (2007).

observed in the atomic clusters of Cr and Mn, which are antiferromagnetic in bulk [8, 9]. Two recent Stern-Gerlach experiments [10, 11] on the measurement of magnetic moment in Co clusters have reported magnetic moments in clusters of sizes as small as of 7 atoms. The intrinsic per-atom magnetic moment was found to be substantially larger than the bulk value and generally decreased with increasing cluster size. The enhancement in the magnetic moment in *small* clusters has been attributed to the lower coordination of the surface atoms resulting in a narrowing of the *d*-bands and hence greater spin polarization. Therefore, magnetic properties of transition metal clusters are very sensitive to local atomic environment and the first step in calculating any electronic property using theoretical approach is to determine the ground state structures of the clusters. In this chapter, we will study the interplay of structure and magnetism of pure Co_n clusters ($n = 2-20$), as they grow atom by atom, using first-principles DFT based calculations. Below we summarize the previous experimental and theoretical works on Co_n clusters.

The magnetic properties of bare Co_n clusters were first investigated via SG molecular beam deflection experiment by Bloomfield and co-workers for Co_{20} - Co_{215} clusters [3, 4] and by de Heer and co-workers for Co_{30} - Co_{300} clusters [5]-[7]. These studies showed that in the temperature range of 77-300 K, the Co_n clusters display high-field deflections, which are characteristic of superparamagnetic behaviour. On the other hand, information on the ground state geometry of the transition metal clusters is usually obtained from the experiments involving chemical probe methods and photoelectron spectroscopy. Such studies for the Co_n clusters are very limited and not definitive. Reactions of Co_n clusters with NH_3 and H_2O [12] indicate icosahedral structures for the bare and ammoniated clusters in the size range $n = 50-120$ and nonicosahedral packing for *small* (around 19 atoms) Co_n clusters. Although the structures of ammoniated Fe_n , Co_n and Ni_n clusters in the size range of $n = 19-34$ atoms have been found to be poly-icosahedral [13], it has been proposed that bare clusters probably adopt a variety of structures. The photoionization experiment [14] indicated icosahedral atomic shell structures for large Ni_n and Co_n clusters of 50-800 atoms. However, structures were not well identified for *small* Co_n clusters ($n \leq 50$) because atomic sub-shell closings in different symmetry based clusters occur in close sequences. These experimental results put together indicate that the icosahedral growth pattern for *small* sized Co_n clusters is less evident.

Theoretical work on Co clusters are limited and the available results are contradictory. Li and Gu [15] performed first-principles calculation of *small* Co_n clusters ($4 \leq n \leq 19$) using spin-polarized discrete variational method within DFT. However, they had not optimized the structures and considered only some special structures with lattice parameters same as the bulk Co. Guevara *et al* [16] used an unrestricted Hartree-Fock tight-binding formalism, starting from *spd*-bulk parameterization, but they only considered fixed body-centred cubic (bcc) and fcc geometries for a maximum of 177 atoms without structural relaxation. Andriotis and Menon [17] have used a tight-binding molecular dynamics scheme to study Co clusters for some selected cluster sizes. Castro *et al* [18] performed all-electron density functional calculations using both local density and generalized gradient approximations. However, the size of the clusters were limited only up to 5 atoms. Recently, Lopez *et al* [19] studied Co_n clusters ($4 \leq n \leq 60$), where minimization was done using an evolutive algorithm based on a many-body Gupta potential [20] and magnetic properties have been studied by a *spd* tight-binding method. As compared to *ab-initio* methods, the parametrized tight-binding Hamiltonian reduces the computational cost drastically, but its main problem is the lack of transferability of its parameters. In particular, because of the lack of DFT like self-consistency the charge transfer effects are not properly accounted for and hence magnetic moment results are not fully reliable.

5.2 Computational Details

The calculations were performed using density functional theory, within the pseudopotential plane wave method as implemented in VASP code. We have used PAW method and PBE exchange-correlation functionals for spin-polarized GGA. The *3d* and *4s* electrons were treated as valence electrons and the wave functions were expanded in the plane wave basis set with the kinetic energy cut-off of 335 eV. Reciprocal space integrations were carried out at the Γ point. Symmetry unrestricted geometry and spin optimizations are performed using conjugate gradient and quasi-Newtonian methods until all the force components were less than a threshold value of 0.005 eV/Å. Simple cubic super-cells were used with the periodic boundary conditions, where two neighbouring clusters were kept separated by at least 12 Å vacuum space. This essentially made the interaction

between the cluster images negligible. For each size, several initial geometrical structures have been considered. To get the ground state structures, we have explicitly considered *all possible* spin multiplicities for each geometrical structure in each cluster size. The cohesive energy per atom was calculated as,

$$E_c(\text{Co}_n) = \frac{1}{n} [n E(\text{Co}) - E(\text{Co}_n)], \quad (5.1)$$

where n is the size of the cluster. $E(\text{Co})$ and $E(\text{Co}_n)$ are the total energies of isolated Co-atom and n -atom Co_n cluster, respectively. For such a definition, a positive sign in E_c corresponds to binding.

5.3 Results and discussions

5.3.1 Trends in structure and magnetism

Co₂ - Co₁₂ clusters

Our calculated ground state structures of Co_n clusters for $n = 2-12$ have been shown in Fig. 5.1. Below we discuss briefly the trend in structure and magnetism for each of these clusters. The experimental estimation of bond length and cohesive energy of Co_2 dimer was first made by mass spectroscopy [21], which are 2.31 Å and 1.72 eV, respectively. Our present calculation gives dimer cohesive energy as 1.45 eV/atom and a bond length of 1.96 Å. This calculated dimer bond length is about 78% of the bulk hcp Co. We found the Co atoms in dimer have bonding configuration closer to $3d^84s^1$ than that of the isolated Co atom, $3d^74s^2$ and in addition to the highly delocalized $4s$ electrons, the more localized $3d$ electrons also contribute strongly to the bonding (similar conclusion was also made in Ref. [22]), which consequently, produces a shorter bond length for the dimer. Total magnetic moment of the Co_2 dimer is $4 \mu_B$, which is also consistent with mass spectroscopic measurement [21] and with the previous first-principles calculations [18],[23]-[25].

The linear and triangular structures are the probable starting structures for Co_3 cluster. Upon relaxation, an isosceles triangle (having each of the equal side length of 2.19 Å and other one of 2.10 Å) with total magnetic moment $5 \mu_B$ is found to be the ground

state with cohesive energy 1.78 eV/atom. Another isosceles triangle with two long and one short bond lengths of 2.25 and 2.06 Å, respectively, is found to be nearly degenerate with the ground state structure (energy difference is only 3 meV). According to the present calculation, the optimal linear structure has a total magnetic moment of $7 \mu_B$ and lies 0.43 eV higher than the ground state. Present result is consistent with the spin resonance spectra of Co_3 in Ar/Kr matrix, which indicated a triangular structure with a total moment of 5 or $7 \mu_B$ to be the ground state [26]. Previous all-electron density functional calculation [18] also predicted an isosceles triangle (2.12, 2.12, 2.24 Å) with a magnetic moment of $1.7 \mu_B$ /atom as the ground state for Co_3 , while tight-binding study [17] predicted an isosceles triangle of much higher bond lengths and magnetic moment.

Out of tetrahedral, rectangular and linear structures as the initial geometries for Co_4 cluster, a distorted tetrahedron with a total magnetic moment of $10 \mu_B$ appears to be the most stable structure. Its cohesive energy is 2.27 eV/atom and average bond length is 2.34 Å. Among the six sides of this tetrahedral ground state, two pairs have equal lengths of 2.14 Å, closer to the bond length of dimer (these are always on opposite TM–TM sides), while the third pair is much larger, 2.72 Å. These short bonds have high $3d$ electron contributions and they are, therefore, the major source of increase of the bonding in the distorted structure. Castro *et al* [18] predicted a strong *Jahn-Teller* distorted tetrahedral ground state with bond lengths almost equal to the present values. Yoshida *et al* [27] also predicted a tetrahedral structure with a bond length of 2.25 ± 0.2 Å as the ground state for Co_4^- anion. The initial rectangular structure, after optimization, becomes a rhombus with each side of length 2.14 Å and two diagonals of 2.67 Å and 3.35 Å and appears as the first isomer with total magnetic moment of $10 \mu_B$, being 0.11 eV higher in energy from the ground state. The optimal linear structure is at a much higher energy than the ground state.

We took trigonal bi-pyramid, square pyramid and two planar structures: (i) two triangles connected through a common vertex and (ii) a pentagon, as the initial structures for Co_5 cluster. The trigonal bi-pyramid with total magnetic moment $13 \mu_B$ is found to be the most stable structure. This structure has 2.55 eV/atom cohesive energy and 2.34 Å average bond length. In this ground state, there are two types of bond lengths: all the sides of the upper and lower triangular pyramids are of same length and are smaller

(2.18 Å), while those of the interfacing planar triangle are much larger, 2.65 Å. Another triangular bi-pyramid and a square pyramid with equal magnetic moments of $11 \mu_B$ are found to be the degenerate first isomer. They lie 125 meV higher in energy. The optimal planar pentagon with $11 \mu_B$ magnetic moment lies much, 1.04 eV, higher and the double triangle structure lies even higher in energy from the ground state. Present results are in agreement with the previous AE-GGA calculation [18], where they predicted the same geometric structure with 2.28 Å average bond length and $2 \mu_B/\text{atom}$ magnetic moment as the ground state. On the other hand, the prediction [19] of average bond length and magnetic moment using Gupta potential is much higher, though it predicted the same geometry.

We have studied the capped trigonal bi-pyramid, octahedron and pentagonal pyramid to search the ground state for Co_6 cluster. From now on for the larger sized clusters, the planar structures have been discarded by intuition. After relaxation, we found an octahedral structure with $14 \mu_B$ total magnetic moment as the ground state. Each side of this octahedral ground state is about 2.27 Å and has a cohesive energy of 2.93 eV/atom. Another slightly distorted octahedron with $12 \mu_B$ moment appears as the first isomer. However, it is 0.87 eV higher compared to the ground state. Our prediction of octahedral ground state is in agreement with previous theoretical studies [19, 15, 28, 24]. The octahedral structure for Co_6 is so stable that even the starting capped triangular bi-pyramidal structure, after relaxation, transforms to the octahedral ground state. In the present calculation, the optimal pentagonal pyramid having $12 \mu_B$ magnetic moment, lies much higher (1.7 eV) in energy compared to the ground state.

It is to be noted that for clusters having more than six atoms, the ground state structures, most often have a octahedral fragment (cf. Fig. 5.1). For Co_7 cluster, we considered capped octahedron, pentagonal bi-pyramid and bi-capped triangular bi-pyramid as the starting guess. After simultaneous relaxation of both geometrical and magnetic structure, the capped octahedron with total magnetic moment $15 \mu_B$ appears as the most stable structure. The experimentally measured magnetic moment, $2.36 \pm 0.25 \mu_B/\text{atom}$ [11], is little higher than our result. The optimal pentagonal bi-pyramid, which is a building block of icosahedral structure, has a total magnetic moment of $15 \mu_B$, and is the first isomer, being 0.19 eV higher in energy. However, using Gupta potential, Lopez *et al* [19]

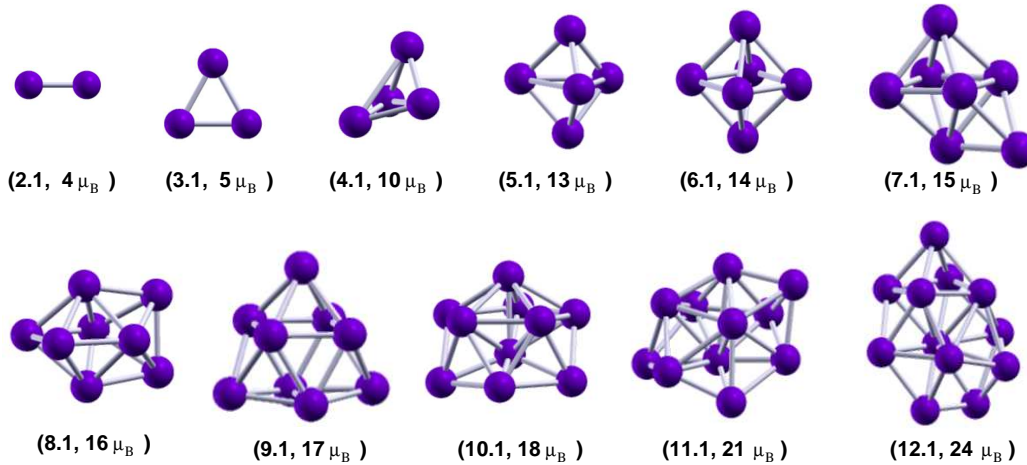


Figure 5.1: Ground state structures of Co_n clusters for $n = 2-12$ obtained by our DFT calculation. Numbers in the parenthesis represent number of atoms in the cluster (followed by .1 indicates ground state) and total magnetic moment, respectively.

predicted a pentagonal bi-pyramidal structure as the ground state, and a capped octahedra as the first isomer. According to our calculation, the optimal bi-capped triangular bi-pyramid has a total magnetic moment of $15 \mu_B$ and lies 0.42 eV higher.

As expected, the most probable starting structures for Co_8 cluster are bi-capped octahedron, capped pentagonal bi-pyramid and tri-capped triangular bi-pyramid. However, the bi-capped octahedron with $16 \mu_B$ magnetic moment is found to be the most stable structure. The experimentally measured magnetic moment, $2.51 \pm 0.15 \mu_B/\text{atom}$ [11], is higher than the present value. The ground state has 3.07 eV/atom cohesive energy and an average bond length of 2.30 \AA . The optimal tri-capped triangular bi-pyramid and the optimal capped pentagonal bi-pyramid have an equal magnetic moment of $16 \mu_B$ but lie 0.4 and 0.48 eV higher in energy respectively. They are the first and second isomers.

Similarly, for the Co_9 cluster, we considered tri-capped octahedron and bi-capped pentagonal bi-pyramid as initial configurations. A distorted tri-capped octahedron with total magnetic moment of $17 \mu_B$ is found to be the most stable structure with 3.14 eV/atom cohesive energy, while experimental magnetic moment is much higher, $2.38 \pm 0.11 \mu_B/\text{atom}$. The optimal bi-capped pentagonal bi-pyramid has $17 \mu_B$ magnetic moment and lies 0.53 eV higher in energy. This structure is found to be the first isomer. However,

calculation by semi-empirical molecular dynamic technique [19] predicted the bi-capped pentagonal bi-pyramid as the ground state with a relatively high magnetic moment.

Different tri-capped pentagonal bi-pyramid (TCPBP) structures along with different tetra-capped octahedral structures were taken as initial structures for Co_{10} cluster. Interestingly, a TCPBP structure with $18 \mu_B$ total magnetic moment is found to be the ground state. The calculated magnetic moment in the ground state is smaller as compared to the neighbouring sizes, which is indeed the case in experiment (cf. Fig. 5.8 and will be discussed later). This is because of the fact that TCPBP is an icosahedral fragment based on pentagonal bi-pyramid. This is different from the structural growth seen for Co_6 - Co_9 clusters, where the ground state structures are all octahedral based. For this TCPBP ground state, average coordination and average bond lengths are slightly higher and the competing effect of these two makes the magnetic moment smaller than its neighbouring clusters. Another TCPBP with total magnetic moment $20 \mu_B$ lies 0.08 eV higher in energy compared to ground state and is found to be the first isomer. The experimental magnetic moment ($2.07 \pm 0.10 \mu_B/\text{atom}$ [11]) is larger compared to the predicted ground state but very close to the first isomer, which is energetically very close to the ground state.

For 11 and 12 atom clusters, the initial structures are derived from 13-atom hcp, icosahedron or cub-octahedral clusters, removing 2 or 1 atoms. Interestingly, after relaxation, the minimal energy structures for both Co_{11} and Co_{12} clusters, have a distorted octahedron as a building block with magnetic moments $21 \mu_B$ and $24 \mu_B$ respectively. The experimentally determined magnetic moments for these two clusters are $2.42 \pm 0.09 \mu_B/\text{atom}$ [11] and $2.26 \pm 0.08 \mu_B/\text{atom}$ [11] respectively, slightly higher than our calculated values.

Co_{13} - Co_{20} clusters

We considered the icosahedral, hcp, cub-octahedral and fcc based geometries as initial structures for Co_{13} cluster. 13-atom icosahedral structure is the first closed shell icosahedron having two pentagonal rings, two apex atoms and a centre atom. We are calling it $\langle 1,5,1,5,1 \rangle$ stacking. A 13-atom hexagonal close packed structure consists of a hexagonal ring around a central atom and two triangular planes above and below it. We are calling

it $\langle 3,7,3 \rangle$ stacking. Upon relaxation of both geometry and spin degrees of freedom, the hcp structure is distorted heavily compared to others having different symmetries. The minimum energy structure is a distorted hcp structure with total magnetic moment $25 \mu_B$ and cohesive energy 3.28 eV/atom. The structure has 22 triangular faces and 33 edges (cf. Fig. 5.2). Knickelbein found the experimental magnetic moment to be $2.30 \pm 0.07 \mu_B/\text{atom}$ [11], which is slightly higher than the present value. However, this calculated value is in good agreement with another recent SG experiment by Xu *et al* [10, 30], which measured $2.00 \pm 0.06 \mu_B/\text{atom}$ moment. Another distorted hcp with total magnetic moment of $27 \mu_B$ and 0.14 eV above the minimum energy state, is the first isomer. The optimal icosahedral structure of total spin $31 \mu_B$ (structure having 20 triangular faces and 30 edges) is 0.17 eV higher than the minimum energy state and emerges as second isomer. Third isomer is a distorted cub-octahedron with total magnetic moment $25 \mu_B$ and it is 0.22 eV above the minimum energy state.

With the increase in the number of atoms in the cluster, the determination of the ground state becomes a difficult task as the number of local minima in the potential energy surface increases very rapidly with the number of atoms in the cluster. For clusters having more than 13 atoms, we have, therefore, considered different initial structures derived from two most competing symmetries: hcp and icosahedral and allow them to relax considering all possible spin configurations to find the minimum energy structure. The predicted minimum energy structure along with an higher energetic isomer for each cluster in the size range $n = 13-20$ have been shown in Fig. 5.2, while table 5.1 and table 5.2 contain the details of the cohesive energy and magnetic moments of ground states and several isomers.

For Co_{14} cluster, the optimal capped icosahedra with total magnetic moment $28 \mu_B$ and the optimal hcp structure (having $\langle 3,7,4 \rangle$ stacking) of same magnetic moment are found to be degenerate. The energy separation is only 4 meV (see Fig. 5.2). We also found several isomers which lie very close to these structures : an icosahedral structure ($24 \mu_B$), a hcp structure ($26 \mu_B$) and another icosahedron ($30 \mu_B$) lie only 5, 7 and 8 meV above the minimum energy state, respectively (see Table 5.1). The very recent SG experimental predictions of magnetic moment range from $2.11 \pm 0.02 \mu_B/\text{atom}$ [10, 30] to $2.29 \pm 0.06 \mu_B/\text{atom}$ [11, 29] for Co_{14} cluster, which are in good agreement with the

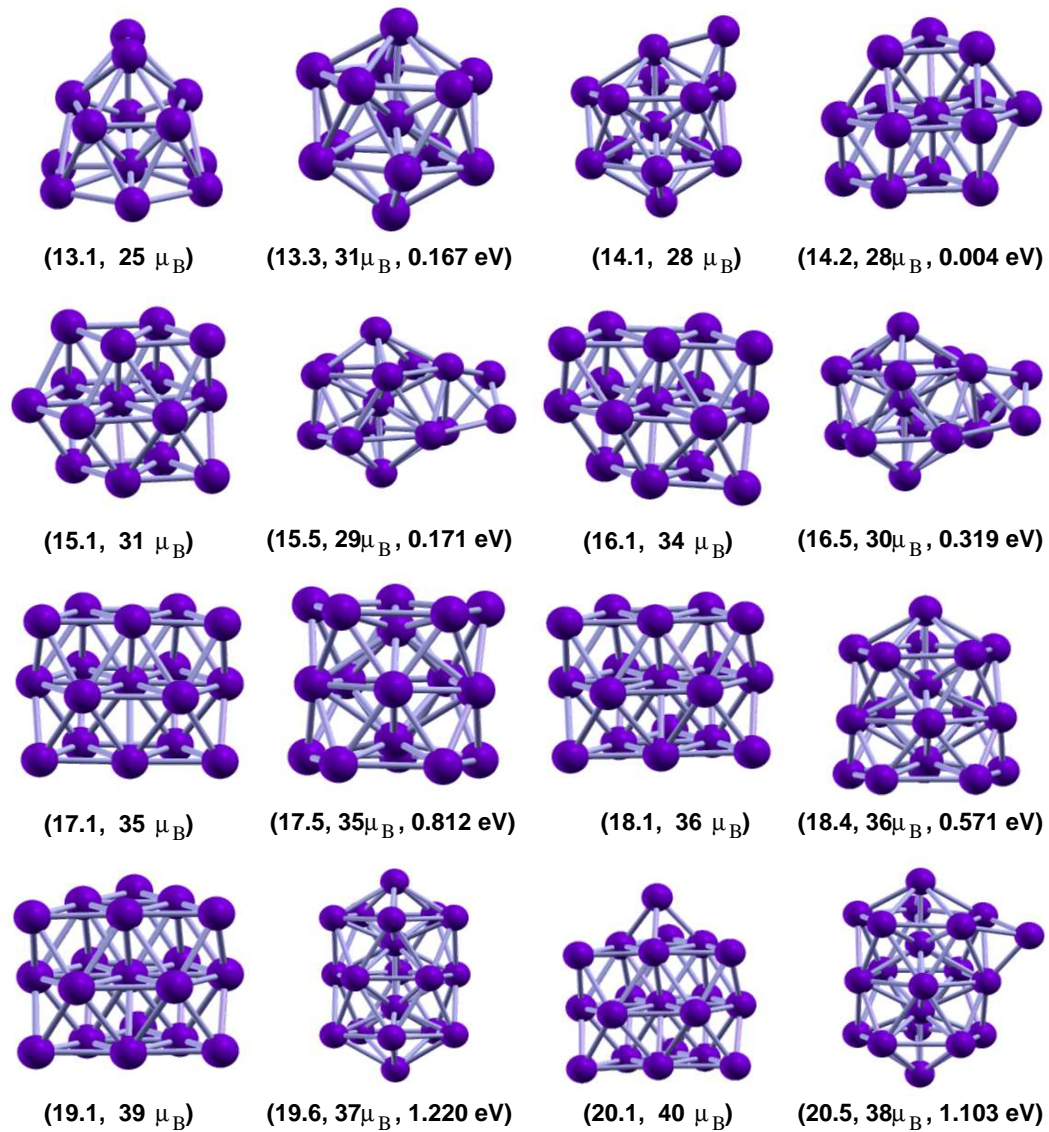


Figure 5.2: The minimum energy state and a higher energy isomer of Co_n clusters ($n = 13$ -20). For $n = 14$, the hcp and icosahedral structures are almost degenerate. For $n = 13$ and 15-20, the minimum energy structure has hcp symmetry and we have shown the optimal icosahedral structure as the higher isomer. The first entry in the parenthesis gives the cluster size as well as isomeric position, second entry corresponds to total magnetic moment and the third entry in the alternate parentheses indicates the relative energy to the minimum energy state.

present result.

The minimum energy structure for Co_{15} has hcp symmetry with $\langle 4,7,4 \rangle$ atomic staking and with total magnetic moment $31 \mu_B$. This calculated magnetic moment is in agreement with the SG experiment of Xu *et al*, which is $2.09 \pm 0.04 \mu_B/\text{atom}$ [10, 30]. However, Knickelbein predicted a larger value [11, 29]. The other hcp structures with total magnetic moments of 29, 33 and $27 \mu_B$ lie ~ 0.05 , 0.12 and 0.17 eV higher than the minimum energy state, being the 1st, 2nd and 3rd isomers respectively. The optimal bicapped icosahedral structure with $29 \mu_B$ magnetic moment is the fourth isomer, which lies 0.17 eV above the lowest energy state.

The same kind of structural growth is observed in the case of Co_{16} cluster. The hcp structure (having $\langle 4,7,5 \rangle$ stacking) with total magnetic moment of $34 \mu_B$ is found to be the lowest in energy and has cohesive energy of 3.46 eV/atom. This structure is nearly degenerate (5 meV lower) with another hcp structure, which has $32 \mu_B$ magnetic moment. The next two isomers are also of same hcp motif, which have 30 and $36 \mu_B$ magnetic moment and they lie 0.21 and 0.31 eV higher in energy with respect to the lowest energy state, respectively. The optimal tricapped icosahedral structures with magnetic moments of 30 and $32 \mu_B$ lie 0.32 and 0.36 eV higher, respectively. The optimal hcp and icosahedral structures are shown in Fig. 5.2. The other icosahedral structure with $\langle 5,1,5,1,4 \rangle$ stacking (*i.e* one less atom in the third pentagonal ring) is found to be much higher in energy.

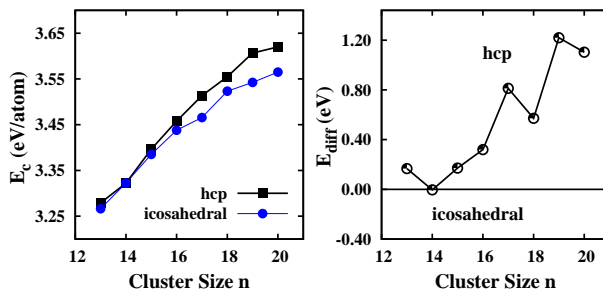


Figure 5.3: Plot of cohesive energy per atom (E_c) for optimal hcp and optimal icosahedral structures (left) and plot of total energy difference between these optimal structures, $E_{\text{diff}} = -[E(\text{hcp}) - E(\text{icosahedral})]$, (right) for the size range $n = 13-20$. E_{diff} increases with cluster size.

The hcp structure (having $\langle 5,7,5 \rangle$ stacking) and with total magnetic moment of 35

μ_B is the lowest energy state for Co_{17} cluster. The calculated magnetic moment, $2.06 \mu_B/\text{atom}$, is slightly smaller than that predicted by both the recent experiments [10, 11] (see Table 5.2). The next three isomers also have hcp symmetry. They have 37, 33 and $31 \mu_B$ magnetic moments and lie 0.12, 0.17 and 0.41 eV higher than the lowest energy state, respectively. The optimal icosahedral structure (Fig. 5.2) has $\langle 5,1,5,1,5 \rangle$ stacking (*i.e.* a double icosahedral structure without two opposite apex atoms) and appears as 4-*th* isomer, being 0.81 eV higher in energy from the minimum energy state.

A $\langle 6,7,5 \rangle$ -stacked hcp structure (Fig. 5.2), which has a total magnetic moment of $36 \mu_B$ is found to be the lowest energy state for Co_{18} cluster. This structure has a cohesive energy of 3.61 eV/atom. The magnetic moment is in agreement with Knickelbein, $2.07 \pm 0.04 \mu_B/\text{atom}$ [11, 29]. However, Xu *et al* predicted a higher value, $2.37 \pm 0.07 \mu_B/\text{atom}$ [10, 30]. Another two hcp structures with total magnetic moments 38 and $34 \mu_B$ lie 0.02 and 0.19 eV higher in energy, respectively and are the first and second isomers. The optimal icosahedral structure (a double icosahedra without one apex atom) has a total magnetic moment of $36 \mu_B$, and lies much higher (0.57 eV) in energy, being the third isomer.

The minimum energy structure for Co_{19} cluster is a hcp based structure with $\langle 6,7,6 \rangle$ stacking and with $39 \mu_B$ magnetic moment. The calculated magnetic moment, $2.05 \mu_B/\text{atom}$, is closer to the value of Knickelbein, $2.21 \pm 0.03 \mu_B/\text{atom}$ [11, 29] than that of the value predicted by Xu *et al*, $2.48 \pm 0.04 \mu_B/\text{atom}$ [10, 30]. The next four isomers are also found to be of same hcp packing. These isomers with total magnetic moments 37, 35, 33 and $41 \mu_B$ lie 0.17, 0.48, 0.90 and 1.16 eV higher than the minimum energy state, respectively. On the other hand, the optimal double icosahedral structure (Fig. 5.2) has $37 \mu_B$ magnetic moment and lies 1.22 eV higher from the ground state. The fcc and hcp fragments have also been proposed as ground state structures in the previous theoretical calculations [15, 16]. Also some calculations [17, 19] predicted icosahedral ground state for Co_{19} .

Among all the considered structures the capped 19-atom hcp geometry (Fig. 5.2) is found to be the lowest energy state for Co_{20} cluster. The calculated magnetic moment is found to be $2 \mu_B/\text{atom}$ for this structure, which is in agreement with the value measured by Knickelbein [11] ($2.04 \pm 0.05 \mu_B/\text{atom}$). However, the moment measured by Xu *et al* is much higher ($2.36 \pm 0.02 \mu_B/\text{atom}$ [10]). Similar to what we have seen for Co_{15} – Co_{19}

clusters, the next few isomers are also of hcp motif. The hcp structures with total magnetic moments 38, 36, and 42 μ_B , which are 0.26, 0.63 and 0.89 eV higher are found to be the first, second and third isomers, respectively. The optimal capped double icosahedral structure has a total magnetic moment of 38 μ_B and appears as the fourth isomer (Fig. 5.2). However, this structure lies much higher in energy (1.10 eV).

In order to distinctly point out the preference of hcp structures over the icosahedral structures in this size range $n = 13-20$ of Co clusters, we have plotted in Fig. 5.3 the cohesive energies for the optimal hcp and optimal icosahedral structures (see Fig. 5.2 for the optimal geometries) and the corresponding energy difference (E_{diff}) between them. The optimal hexagonal structures are always found to be the ground state for this size range except for Co_{14} , where the optimal hexagonal and icosahedral structures are found to be degenerate. Moreover, few isomers next to the ground state are also of hcp motif and the optimal icosahedral structures appear as higher energy (third, fourth or fifth) isomers for $n = 15-20$. The energy difference between the hcp ground state and optimal icosahedral structures increases with increasing cluster size making icosahedral structures more and more unfavourable. We plot the energy variation as a function of cluster magnetic moment for icosahedral and hcp Co_{13} , Co_{15} , Co_{17} , and Co_{19} clusters in Fig. 5.4. Both the structures show similar qualitative behaviour for all the clusters and they have hcp minima around $\sim 2 \mu_B/\text{atom}$ moment.

5.3.2 Understanding structural stability

Calculated cohesive energies are plotted in Fig. 5.5 for the ground states of Co_n clusters in the size range $n = 2-20$. Since the coordination number increases with the number of atoms in the cluster, the cohesive energy increases monotonically. The cohesive energy of the largest cluster studied here (Co_{20}) is 3.62 eV/atom, which is about 82% of the experimental bulk value, 4.4 eV/atom [31] for hcp Co. Upon extrapolation of the linear fit of the cohesive energy per atom data towards $n^{-1/3} \rightarrow 0$ [Fig. 5.5(a)], we can estimate the cohesive energy of the infinitely large cluster. This is found to be 5.0 eV/atom, which is larger than the experimental value for hcp bulk Co. However, within the same level of theory we found the hcp bulk cohesive energy to be 5.11 eV/atom, which is close to the

Table 5.1: Cohesive energy, relative energy to the theoretically computed minimum energy state ($\Delta E = E - E_{\min}$) and magnetic moment for Co_n ($n = 2-14$) clusters. The entry in the first column “ $n.i$ ” indicates ground state for $i = 1$ and isomers for $i > 1$ of n atoms cluster. Recent SG experimental results (Refs. [10, 11, 29, 30]) of the magnetic moment are shown for comparison.

Cluster	E_c (eV/atom)	ΔE (eV)	Magnetic Moment (μ_B/atom)	
			Theory	SG Exp.
2.1	1.452	0.000	2.00	—
3.1	1.783	0.000	1.67	—
3.2	1.783	0.003	2.33	—
4.1	2.274	0.000	2.50	—
4.2	2.248	0.106	2.50	—
5.1	2.553	0.000	2.60	—
5.2	2.528	0.125	2.20	—
6.1	2.929	0.000	2.33	—
6.2	2.784	0.869	2.00	—
7.1	2.971	0.000	2.14	2.36±0.25 [11, 29]
7.2	2.944	0.192	2.14	—
8.1	3.074	0.000	2.00	2.51±0.15 [11, 29]
8.2	3.024	0.400	2.00	—
8.3	3.013	0.484	2.00	—
9.1	3.143	0.000	1.89	2.38±0.11 [11, 29]
9.2	3.084	0.527	1.89	—
10.1	3.137	0.000	1.80	2.07±0.10 [11, 29]
10.2	3.128	0.085	2.00	—
11.1	3.205	0.000	1.91	2.42±0.09 [11, 29]
11.2	3.203	0.016	1.91	—
12.1	3.252	0.000	2.00	2.26±0.08 [11, 29](2.21±0.01) [10, 30]
12.2	3.243	0.103	1.89	—
13.1	3.279	0.000	1.92	2.30±0.07 [11, 29] (2.00±0.06) [10, 30]
13.2	3.268	0.140	2.08	—
13.3	3.266	0.167	2.38	—
14.1	3.323	0.000	2.00	2.29±0.06 [11, 29] (2.11±0.02) [10, 30]
14.2	3.322	0.004	2.00	—
14.3	3.322	0.005	1.71	—
14.4	3.322	0.007	1.86	—
14.5	3.320	0.008	2.14	—

Table 5.2: Cohesive energy, relative energy to the theoretically computed minimum energy state ($\Delta E = E - E_{\min}$) and magnetic moment for Co_n ($n = 15-20$) clusters. Recent SG experimental results (Refs. [10, 11, 29, 30]) of the magnetic moment are shown for comparison.

Cluster	E_c (eV/atom)	ΔE (eV)	Magnetic Moment (μ_B /atom)	
			Theory	SG Exp.
15.1	3.397	0.000	2.07	2.38±0.03 [11, 29] (2.09±0.04) [10, 30]
15.2	3.393	0.046	1.93	
15.3	3.388	0.125	2.20	
15.4	3.385	0.169	1.80	
15.5	3.385	0.171	1.93	
16.1	3.458	0.000	2.13	2.53±0.04 [11, 29] (2.32±0.01) [10, 30]
16.2	3.458	0.005	2.00	
16.3	3.445	0.208	1.88	
16.4	3.439	0.308	2.25	
16.5	3.438	0.319	1.88	
17.1	3.514	0.000	2.06	2.24±0.04 [11, 29] (2.19±0.02) [10, 30]
17.2	3.506	0.123	2.18	
17.3	3.504	0.167	1.94	
17.4	3.490	0.407	1.82	
17.5	3.466	0.812	2.06	
18.1	3.555	0.000	2.00	2.07±0.04 [11, 29] (2.37±0.07) [10, 30]
18.2	3.554	0.024	2.11	
18.3	3.544	0.194	1.89	
18.4	3.523	0.571	2.00	
19.1	3.607	0.000	2.05	2.21±0.03 [11, 29] (2.48±0.04) [10, 30]
19.2	3.597	0.174	1.95	
19.3	3.581	0.478	1.84	
19.4	3.559	0.901	1.74	
19.5	3.546	1.158	2.16	
19.6	3.542	1.220	1.95	
20.1	3.620	0.000	2.00	2.04±0.05 [11, 29] (2.36±0.02) [10, 30]
20.2	3.607	0.262	1.90	
20.3	3.588	0.634	1.80	
20.4	3.576	0.891	2.10	
20.5	3.565	1.103	1.90	

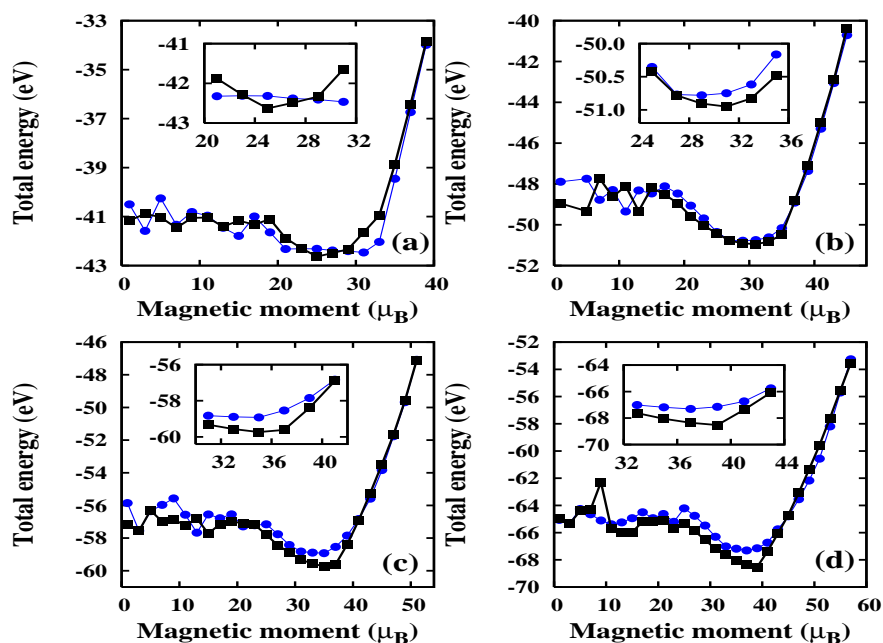


Figure 5.4: Plot of total energy as a function of magnetic moment for (a) Co_{13} , (b) Co_{15} , (c) Co_{17} and (d) Co_{19} clusters. The dot (square) represents icosahedral (hcp) structure. Insets represent magnification around the minima.

extrapolated value but again larger than the experimental value. This overestimation is consistent with the DFT calculation [32].

We calculate the second difference in the total energy as :

$$\Delta_2 E(n) = E(n+1) + E(n-1) - 2E(n), \quad (5.2)$$

where $E(n)$ represents the total energy of an n -atom cluster. Calculated $\Delta_2 E$ has been plotted in Fig. 5.5(b), where we see the peaks at $n = 6$ and 9 , *i.e.*, the clusters with 6 and 9 atoms are particularly more stable than their neighbouring clusters. The stable structure for Co_6 is an octahedron and for Co_9 , it is a distorted tri-capped octahedron. The collision-induced dissociation experiment (CID) [33] has also been indicated a maximum at $n = 6$ in the measured dissociation energy, which indicates a higher stability of the hexamer. The extra stability of hexamer indicates that the octahedral structure can act as a building block for larger size clusters and, indeed, for Co_{15} – Co_{20} clusters, we have found a distinct hcp growth pattern and an octahedron is just a fragment of a hcp structure.

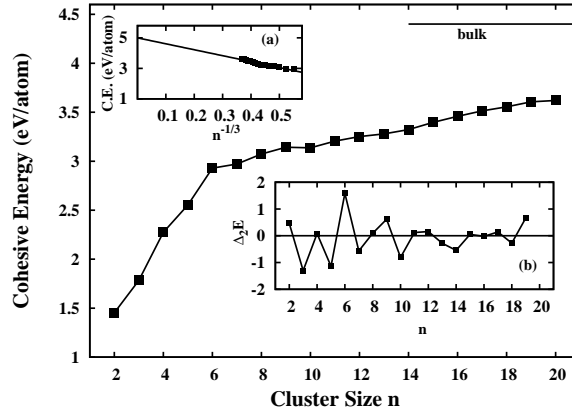


Figure 5.5: Plot of cohesive energy per atom as a function of cluster size n for the ground state structures of the entire size range $2 \leq n \leq 20$. (a) Plot of cohesive energy per atom (C.E.) as a function of $n^{-1/3}$ for the clusters Co_n , $6 \leq n \leq 20$ and a linear fit ($-3.90 n^{-1/3} + 5.00$) to the data. (b) Plot of second difference in total energy ($\Delta_2 E$), which represents the relative stability.

The calculated stability (Fig. 5.5 (b)) shows minima at $n = 3, 5, 7, 10$ and 14 , which are related to their weak bonding.

This can be further demonstrated by studying the dissociation energies as an n -atom cluster fragments into m and $(n - m)$ -atom clusters. The m -channel dissociation energy can be calculated as,

$$D_m(n) = E(m) + E(n - m) - E(n), \quad (5.3)$$

where $E(n)$, $E(m)$ and $E(n - m)$ are the total energies of n , m and $(n - m)$ atom clusters, respectively. We have plotted the calculated single channel (D_1) and dimer channel (D_2) dissociation energies in Fig. 5.6 and D_1 is compared with the CID experiment by Hales *et al* [33]. However, they have estimated this dissociation energy through an indirect method : actually, they measured the single channel dissociation energy of Co_n^+ cation cluster and derived the same for the neutral one by using the ionization energies (IE) of the neutral clusters measured by Yang and Knickelbein [34] and Parks *et al* [35], *i.e.*,

$$D_1^{\text{exp}} = D_1(\text{Co}_n^+) + \text{IE}(\text{Co}_n) - \text{IE}(\text{Co}_{n-1}). \quad (5.4)$$

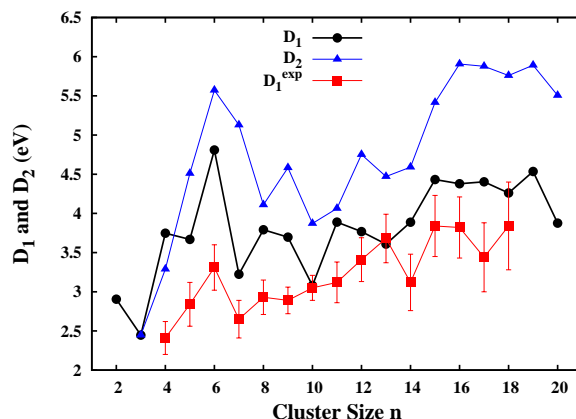


Figure 5.6: Plot of single channel, D_1 and dimer channel, D_2 , dissociation energies as a function of cluster size n for the GS configurations. We compare our calculated single channel dissociation with the CID experimental result in Ref. [33].

The calculated single channel dissociation energy, D_1 , shows a high peak at $n = 6$ and dips at $n = 5, 7$ and 10 , which are consistent with our stability analysis. However, we do not find any dip in the calculated dissociation energy at $n = 14$, as has been seen in the CID experiment. Generally, the single channel dissociation energy is the most favourable except for $n = 4$, where the dimer dissociation ($\text{Co}_4 \rightarrow \text{Co}_2 + \text{Co}_2$) is more favourable than the single channel ($\text{Co}_4 \rightarrow \text{Co}_3 + \text{Co}$) dissociation. Table 5.3 shows the theoretically computed single channel bond dissociation energy compared to the experimentally measured values [33] for the entire range of clusters having sizes 2 to 20.

To understand the optimized structures further, we calculated the average bond lengths and average coordination number for the ground state geometries and plotted them in Fig. 5.7(a) and Fig. 5.7(b), respectively, as a function of cluster size. These two quantities are closely related to the structure of the cluster. We define the average bond length as $\langle r \rangle = (1/n_b) \sum_{i>j} r_{ij}$, where r_{ij} is the bond distance between the j -th and i -th atoms, and n_b is the number of such bonds. Here we consider that two atoms are bonded if their inter atomic distance is within 2.91 \AA , which is around the average of the first (2.51 \AA) and second (3.54 \AA) nearest-neighbour distances in bulk Co. The average coordination number in a cluster is defined as $\langle n_c \rangle = (1/n) \sum_k n_k$ where n_k is the number of neighbours

Table 5.3: Theoretically calculated single channel bond dissociation energies (BDE) compared with experimentally measured values in Ref. [33] for Co_n ($n = 2-20$). Experimental uncertainties are within parentheses.

Co_n	BDE(eV)		Co_n	BDE(eV)	
	Theory	CID Expt.		Theory	CID Expt.
2	2.90	≤ 1.32	12	3.77	3.41(0.28)
3	2.45	≥ 1.45	13	3.61	3.68(0.31)
4	3.75	2.41(0.21)	14	3.89	3.12(0.36)
5	3.67	2.84(0.28)	15	4.43	3.84(0.39)
6	4.81	3.31(0.29)	16	4.38	3.82(0.39)
7	3.22	2.65(0.24)	17	4.40	3.44(0.44)
8	3.79	2.93(0.22)	18	4.26	3.84(0.56)
9	3.70	2.89(0.17)	19	4.54	
10	3.08	3.05(0.16)	20	3.88	
11	3.89	3.12(0.26)			

within the chosen cut-off of the k -th atom in the cluster of n atoms. The convergence of the average bond length to the bulk value (2.51 Å) is much faster than the convergence of average coordination, which is far below the bulk value (12 for hcp Co). Dips at $n = 6$ and 9 in Fig. 5.7(a) indicate that the atoms in these clusters are closely spaced and strongly bonded compared to the neighbours, and therefore are more stable than the neighbouring structures. While the peaks at $n = 5, 10$ and 14 in Fig. 5.7(a) and at $n = 10$ and 14 in Fig. 5.7(b) indicate that atoms in these clusters are far apart and slightly more coordinated than their neighbours [36], which results in a weak bonding in these clusters compared to their neighbours.

5.3.3 Understanding magnetic moments

The calculated magnetic moments are plotted in Fig. 5.8 as a function of cluster size (n). The Co–Co interaction is always ferromagnetic for the entire size range studied, as it is for hcp bulk Co. However, the magnetic moment (2–2.5 μ_B /atom) is larger than the hcp bulk value, 1.72 μ_B /atom [31]. This enhancement in moment for a few

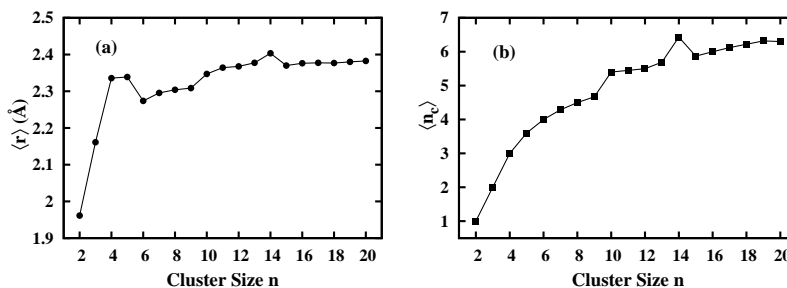


Figure 5.7: Plot of (a) average bond length $\langle r \rangle$ and (b) average coordination $\langle n_c \rangle$, as function of cluster size n for the ground state geometries. Dots and squares represent the data points, while solid line through them is guide to eye.

atom cluster can readily be understood from the more localized d -electrons resulting from the decrease in effective hybridization. The calculated magnetic moments are in fair agreement with the very recent SG experiments by Xu *et al* [10] and Knickelbein [11]. Fig. 5.8 shows a qualitative agreement between the calculated and the experimental values [10, 11, 29, 30] though the calculated moments are always underestimated systematically. However, calculated moments are close to the values predicted by Xu *et al* [10, 30] for the size range $n = 13-17$ and in the size range $n = 18-20$ they are close to the values predicted by Knickelbein [11, 29]. The underestimation of calculated moment may be due to the fact that we did not include spin-orbit interaction in the present calculation. Moreover, one should remember that the magnetic moments in a magnetic deflection measurement are always derived assuming a model, which may influence the outcome. For example, Knickelbein [11] used either superparamagnetic or locked moment model, whether Xu *et al* [10] assumed an adiabatic magnetization model to derive the moments experimentally for cobalt clusters. It is important to note that both experiments show same size evolution in general but there are some systematic differences. However, this is not due to the adoption of different models to calculate the magnetic moment as both the models resemble with the same Curie law for magnetization [10, 11] but may be due to different isomer distribution in the SG beam.

The magnetic moment is strongly correlated with the effective hybridization, which is closely related to the average bond length $\langle r \rangle$ and the average coordination number $\langle n_c \rangle$. As $\langle n_c \rangle$ decreases the magnetic moment should increase through the decrease in

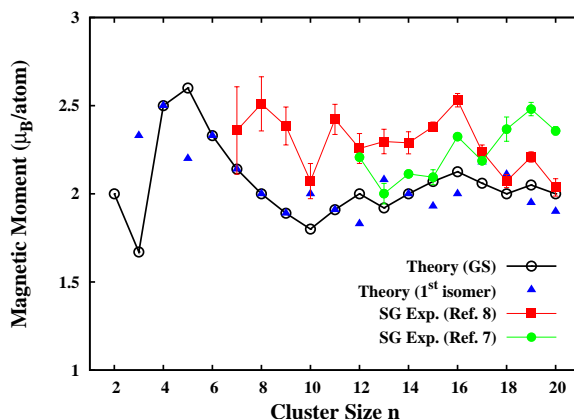


Figure 5.8: Size dependent variation of magnetic moment of the corresponding ground states. Calculated magnetic moments of the first isomers have also been shown. Calculated magnetic moments are compared with experimental results (Ref. [11] and Ref. [10]).

effective hybridization. On the other hand, the dependency of magnetic moment on $\langle r \rangle$ is directly proportional : a decrease in $\langle r \rangle$ results in decrease in magnetic moment through the enhancement in effective bonding. Fig. 5.7(a) and Fig. 5.7(b) show that as we go from $n = 4$ to $n = 10$, both $\langle r \rangle$ and $\langle n_c \rangle$ increase, whereas Fig. 5.8 shows that the magnetic moment per atom decreases. Therefore, between these two competing contributions ($\langle r \rangle$ and $\langle n_c \rangle$) to the magnetic moment, the average coordination number dominates over the average bond length in the size range $n = 4-10$. In the size range, $n = 11-20$, the variation of $\langle r \rangle$ (Fig. 5.7a) and $\langle n_c \rangle$ (Fig. 5.7b) is much slower with n , and therefore, the magnetic moment per atom does not vary rapidly. It is around $2 \mu_B/\text{atom}$ for all the clusters in this size range. So, in this size range, it is hard to predict the dominant parameter for magnetism. To illustrate the effect of $\langle r \rangle$ and $\langle n_c \rangle$ on the magnetism in this size range, we compare these two quantities for the optimal hcp and icosahedral structures (see insets (a) and (b) of Fig. 5.9). It is seen that for a hcp structure, both the $\langle r \rangle$ and $\langle n_c \rangle$ are smaller than those of corresponding icosahedral structure for a particular n -atom cluster. In addition the magnetic moments of optimal hcp clusters are always larger than or equal to that of the corresponding optimal icosahedral clusters (see Fig. 5.9), which again demonstrates that in this size range also the coordination dominates over the average

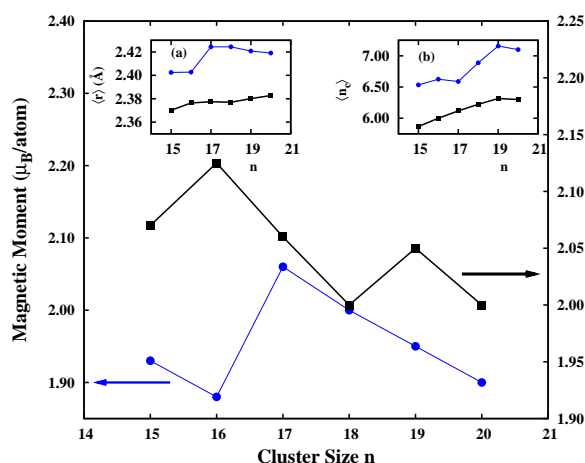


Figure 5.9: Comparison of magnetic moment between optimized hcp and optimized icosahedral structures for Co_n in the size range $n = 15-20$. The filled squares and filled circles correspond to results for hcp and icosahedral structures, respectively. The insets show the corresponding comparisons for (a) average bond length and (b) average coordination number.

bond length in deciding magnetism.

5.3.4 Comparison with other $3d$ transition metal clusters

For Co_n clusters, we have seen a clear trend in the optimized structures : it prefers hcp-like symmetry over icosahedral symmetry in the size range $n = 13-20$. It is a very unusual feature as the *small* clusters of other $3d$ transition metal elements generally prefer the icosahedral growth pattern. For example, self-consistent pseudopotential calculation on Mn_n clusters ($n = 2 - 20$) by Kabir *et al* [37] showed a clear icosahedral growth in the size range $n = 11 - 20$. Same trend has also been reported by Briere *et al* [38]. Icosahedron or bcc rhombic dodecahedron structure for Fe clusters have been indicated previously [39, 40]. Nayak *et al* [41] reported icosahedral packing for Ni_n ($n \leq 23$) clusters while Lathiotakis *et al* [42, 43] showed icosahedral or fcc-like ground states for Ni_n with $n \leq 55$. Copper having closed d shell and a single valance s electron, behaves like alkali metals and the icosahedral packing in *small* Cu_n clusters is, therefore, more probable, which is supported by the work of Kabir *et al* [44] using molecular dynamic method and by Winter

et al [45] from experimental study with exception of the study by Guvelioglu *et al* [46] which predicts somewhat different type of packing for the ground state structures of Cu_n ($n = 12-15$).

In order to understand why cobalt clusters prefer the hcp structure even at cluster size $n < 20$, while the clusters of other $3d$ late transition metal elements apparently prefer icosahedral structures, we have repeated the same calculation for Fe_n clusters in the size range $n = 13-20$. That means we have considered the different hcp and icosahedral symmetry based initial structures for each size and allow them to relax for all possible spin configurations to determine the minimum energy structures. In the following we present the results of our preliminary investigation. Fe_n clusters have reportedly larger magnetic moment than that of the same sized Co_n clusters [47], as it is in bulk. We also find larger magnetic moments of the minimum energy Fe clusters than that of Co clusters, but the interesting point of our structural relaxation calculation is that unlike Co_n clusters, Fe_n clusters prefer to adapt icosahedral growth pattern for each of the minimum energy structures in the size range of our interest. Table 5.4 contains the cohesive energy of the

Table 5.4: Cohesive energies of the optimal hcp and optimal icosahedral structures for both Co_n and Fe_n clusters ($n = 13-20$) in the spin-polarized calculation. It is clearly seen that while Co_n clusters prefer hcp-like symmetry, Fe_n clusters favor icosahedral growth pattern. Number in the parenthesis is the total magnetic moment of the optimal structure.

Magnetic Co_n clusters			Magnetic Fe_n clusters		
Cluster size	Cohesive energy (eV)		Cluster size	Cohesive energy (eV)	
	hcp	icosa		hcp	icosa
Co_{13}	42.630 (25)	42.460 (31)	Fe_{13}	41.509 (42)	42.789 (44)
Co_{14}	46.515 (28)	46.520 (28)	Fe_{14}	45.058 (42)	46.133 (46)
Co_{15}	50.950 (31)	50.780 (29)	Fe_{15}	50.228 (46)	50.278 (48)
Co_{16}	55.330 (34)	55.010 (30)	Fe_{16}	53.280 (50)	54.152 (50)
Co_{17}	59.730 (35)	58.920 (35)	Fe_{17}	57.144 (54)	58.037 (52)
Co_{18}	63.990 (36)	63.420 (36)	Fe_{18}	61.891 (56)	62.161 (56)
Co_{19}	68.530 (39)	67.310 (37)	Fe_{19}	64.356 (58)	66.256 (58)
Co_{20}	72.410 (40)	71.300 (38)	Fe_{20}	68.210 (60)	69.610 (60)

optimal hcp and optimal icosahedral structures for both Co_n clusters and Fe_n clusters

Table 5.5: *rms distortions* of the optimal hcp and optimal icosahedral structures for both Co_n and Fe_n clusters ($n = 13-20$) in the spin-polarized calculation. Less distorted structures appear as more stable.

Magnetic Co_n clusters			Magnetic Fe_n clusters		
Cluster	<i>rms distortions</i>		Cluster	<i>rms distortion</i>	
size	hcp	icosa	size	hcp	icosa
Co_{13}	0.070	0.057	Fe_{13}	0.101	0.080
Co_{14}	0.068	0.079	Fe_{14}	0.107	0.084
Co_{15}	0.036	0.073	Fe_{15}	0.100	0.075
Co_{16}	0.058	0.077	Fe_{16}	0.125	0.083
Co_{17}	0.054	0.110	Fe_{17}	0.129	0.076
Co_{18}	0.046	0.118	Fe_{18}	0.113	0.089
Co_{19}	0.043	0.073	Fe_{19}	0.121	0.096
Co_{20}	0.072	0.087	Fe_{20}	0.123	0.095

($n = 13-20$). In order to understand the optimal structures and the distortions imparted to them after relaxation, we have calculated the average *rms distortion* of the bond lengths and the results are listed in table 5.5. We find that less distorted structures appear to be more stable. Nevertheless, the fact remains that Fe and Co clusters show different types of structural preference. Fe atom has one more unpaired electron than Co atom, consequently magnetism of Fe clusters, in general, is larger than that of Co clusters. To investigate the role of magnetism, we have therefore carried out nonmagnetic calculation as well by optimizing the hcp and icosahedral structures. The cohesive energies of the optimal hcp and optimal icosahedron in the nonmagnetic phase for each cluster size have been listed in table 5.6 for both Co_n and Fe_n clusters. Surprisingly, we have found that all Fe-clusters in this size range, now stabilize in hcp phase, while few Co-clusters (Co_{17} - Co_{20}) stabilize in hcp phase and few (Co_{13} - Co_{16}) prefer to stabilize in icosahedral phase. This means that switching on of the magnetism changes the stable phase of Fe_n clusters from hcp to icosahedral symmetry, while it enhances the possibility of stabilizing the hcp phase in case of Co_n clusters. It is therefore indicating that higher value of magnetism of Fe-clusters is somehow playing the role in stabilizing the icosahedral pattern in magnetic phase.

Table 5.6: Cohesive energies of the optimal hcp and optimal icosahedral structures for both Co_n and Fe_n clusters ($n = 13-20$) in non-magnetic calculation.

Nonmagnetic Co_n clusters			Nonmagnetic Fe_n clusters		
Cluster size	Cohesive energy (eV)		Cluster size	Cohesive energy (eV)	
	hcp	icosa		hcp	icosa
Co_{13}	36.480	37.250	Fe_{13}	33.439	32.339
Co_{14}	40.400	40.810	Fe_{14}	36.653	35.703
Co_{15}	44.400	44.510	Fe_{15}	40.368	39.108
Co_{16}	47.997	48.120	Fe_{16}	43.752	42.672
Co_{17}	52.010	51.760	Fe_{17}	47.247	46.614
Co_{18}	55.880	55.460	Fe_{18}	51.161	49.537
Co_{19}	59.830	59.370	Fe_{19}	54.856	52.796
Co_{20}	63.060	63.020	Fe_{20}	57.690	56.080

Our calculated density of states also points to the same signature which we got from energetics. Fig. 5.10 shows the calculated density of states of the optimal hcp and optimal icosahedral structures of 19-atom Co and Fe clusters, both in nonmagnetic as well as magnetic phases. First of all, each cluster shows finite DOS at the Fermi energy. Nonmagnetic DOSs have peaks at Fermi energy showing the instability towards magnetic solution according to Stonor's criteria. It is also seen that nonmagnetic icosahedral DOS has two peaks around Fermi energy and peak height is larger than that of hcp DOS, for both Co_{19} and Fe_{19} . This may be the possible reason behind the preference of hcp-like structure over the icosahedron-like structure of Co_{19} and Fe_{19} clusters in nonmagnetic phase. In magnetic calculation, DOS is much more illustrative for comparison of relative stability between the two structures. For Co_{19} cluster, magnetic icosahedral DOS has large peaks at the Fermi energy compared to peaks in magnetic hcp DOS, indicating less stability of icosahedral structure. On the other hand, both icosahedral and hcp DOSs of magnetic Fe_{19} cluster have dips at the Fermi energy. However, curvature of icosahedral dip is higher and shifted towards lower energy. This indicates the higher stability of icosahedral structure over the hcp structure for magnetic Fe_{19} cluster.

We have also repeated the same calculation for other three $3d$ transition metal ele-

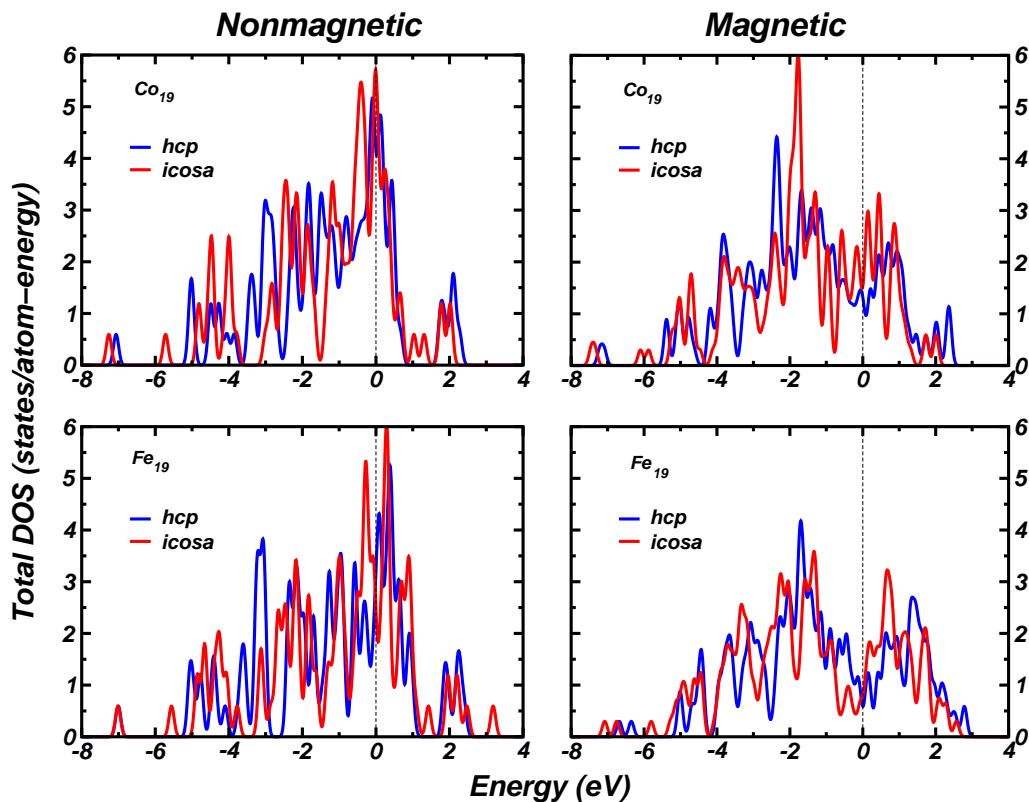


Figure 5.10: Plot of density of states (DOS) (with half-width = 0.1 eV) of the optimal hcp and optimal icosahedral structures of Co_{19} and Fe_{19} clusters, both in nonmagnetic phase (left panel) and magnetic phase (right panel). Energy along x -axis is with respect to Fermi energy of the corresponding system. Magnetic DOS is averaged out between majority and minority channels.

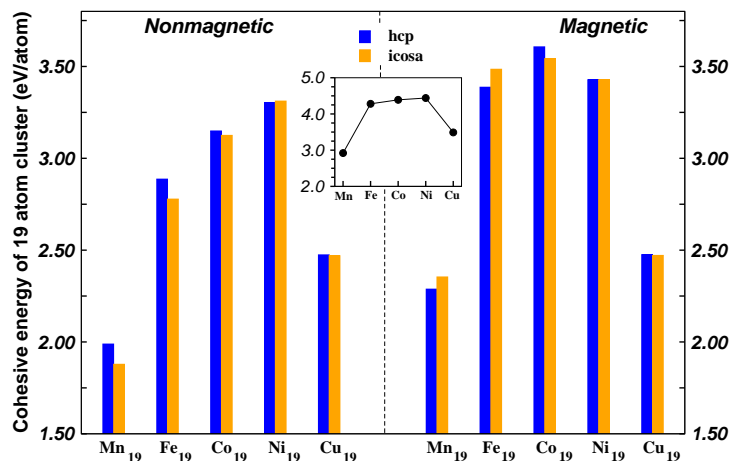


Figure 5.11: Plot of cohesive energy per atom for X_{19} [$X = \text{Mn}, \text{Fe}, \text{Co}, \text{Ni}, \text{Cu}$] in both nonmagnetic phase(left) and magnetic phase(right). The blue vertical bars correspond to hcp structure and orange bars correspond to icosahedral structure. The inset shows the trend in bulk cohesive energy for Mn, Fe, Co, Ni and Cu.

ments: Mn, Ni and Cu, only for 19 atom cluster size. In Mn_{19} cluster, Mn-atoms have very large local magnetic moments [37], while Ni clusters are known to have very fragile magnetic moment [41, 48] and Cu clusters are almost nonmagnetic [46, 49, 50]. It is to be noted that ground states of Mn-clusters are reported to have non-collinear magnetic distribution [51], while our calculation is purely collinear. Fig. 5.11 shows the cohesive energies of the optimal hcp and optimal icosahedral structures for Mn_{19} , Ni_{19} and Cu_{19} along with Fe_{19} and Co_{19} , both in nonmagnetic and magnetic phases. Again we see that nonmagnetic Mn_{19} stabilizes in hcp structure, while switching on of magnetism stabilizes the icosahedral structure over hcp structure. For Ni_{19} and Cu_{19} , the magnetism has almost no role and hcp and icosahedral structures are energetically almost degenerate.

5.4 Summary and Conclusions

Two recent SG experiments on magnetic moment measurement of smaller size cobalt clusters [10, 11] have motivated us to carry out a detail first-principles study on pure Co_n clusters ($n = 2-20$). As geometrical structure of clusters is an integral part in explaining

any electronic property like magnetism, we have firstly carried out an exhaustive study to determine the actual ground state structures for each cluster size. The calculated magnetic moments of the ground state structures are found to be higher than that of the corresponding hcp bulk value and follow the same trend as found in the S-G experiments. An unusual hcp growth pattern has been observed in the ground state structures of Co-clusters, unlike *small* clusters of other 3d transition metals, for example Mn and Fe, usually adopt icosahedral growth pattern. However, in nonmagnetic phase, all of them have a tendency to adapt hcp-like structure. Therefore, the magnetism is supposedly playing a key role in deciding the favorable structural pattern.

Bibliography

- [1] A. J. Cox, J. G. Louderback and L. A. Bloomfield, *Phys. Rev. Lett.* **71**, 923 (1993); A. J. Cox, J. G. Louderback, S. E. Apsel and L. A. Bloomfield, *Phys. Rev. B* **49**, 12295 (1994).
- [2] I. M. L. Billas, J. A. Becker, A. Chatelain and W. A. de Heer, *Phys. Rev. Lett.* **71**, 4067 (1993); D. M. Cox, D. J. Trevor, R. L. Wheetten, E. A. Rohlfing and A. Kaldor, *Phys. Rev. B* **32**, 7290 (1985).
- [3] J. P. Bucher, D. C. Douglass and L. A. Bloomfield, *Phys. Rev. Lett.* **66**, 3052 (1991).
- [4] D. C. Douglass, A. J. Cox, J. P. Bucher and L. A. Bloomfield, *Phys. Rev. B* **47**, 12874 (1993).
- [5] I. M. L. Billas, A. Chatelain, and W. A. de Heer, *Science* **265**, 1682 (1994).
- [6] I. M. L. Billas, A. Chatelain, and W. A. de Heer, *J. Magn. Magn. Mater.* **168**, 64 (1997).
- [7] D. Gerion, A. Hirt, I. M. L. Billas, A. Chatelain, and W. A. de Heer, *Phys. Rev. B* **62**, 7491 (2000).
- [8] L. A. Bloomfield, J. Deng, H. Zhang and J. W. Emmert, in Proceedings of the International Symposium on Cluster and Nanostructure Interfaces, edited by P. Jena, S. N. Khanna and B. K. Rao (World Publishers, Singapore, 2000), p.131
- [9] M. B. Knickelbein, *Phys. Rev. Lett.* **86**, 5255 (2001); M. B. Knickelbein, *Phys. Rev. B* **70**, 14424 (2004).
- [10] X. Xu, S. Yin, R. Moro and W. A. de Heer, *Phys. Rev. Lett.* **95**, 237209 (2005).

- [11] M. B. Knickelbein, *J. Chem. Phys.* **125**, 044308 (2006).
- [12] E. K. Parks, T. D. Klots, B. J. Winter, and S. J. Riley, *J. Chem. Phys.* **99**, 5831 (1993).
- [13] E. K. Parks, B. J. Winter, T. D. Klots, and S. J. Riley, *J. Chem. Phys.* **96**, 8267 (1992).
- [14] M. Pellarin, B. Baguenard, J. L. Vialle, J. Lerme, M. Broyer, J. Miller, and A. Perez, *Chem. Phys. Lett.* **217**, 349 (1994).
- [15] Z.-Q. Li and B L. Gu, *Phys. Rev. B* **47**, 13611 (1993).
- [16] J. Guevara, F. Parisi, A. M. Llois, and M. Weissmann, *Phys. Rev. B* **55**, 13283 (1997).
- [17] A. N. Andriotis, and M. Menon, *Phys. Rev. B* **57**, 10069 (1998).
- [18] M. Castro, C. Jamorski, D. R. Salahub, *Chem. Phys. Lett.* **271**, 133 (1997).
- [19] J. L. Rodriguez-Lopez, F. Aguilera-Granja, K. Michaelian, and A. Vega, *Phys. Rev. B* **67**, 174413 (2003).
- [20] R. P. Gupta, *Phys. Rev. B* **23**, 6265 (1983).
- [21] A. Kant, B. Strauss, *J. Chem. Phys.* **41**, 3806 (1964).
- [22] D. G. Leopold, W. C. Lineberger, *J. Chem. Phys.* **85**, 51 (1986).
- [23] H. Wang, Y. G. Khait and M. R. Hoffmann, *Mol. Phy.* **103**, 263 (2005).
- [24] H.- J. Fan, C.- W. Liu, M.-S. Liao, *Chem. Phys. Lett.* **273**, 353 (1997).
- [25] J. Harris and R. O. Jones, *J. Chem. Phys.* **70**, 830 (1979).
- [26] R. J. Van Zee, Y. M. Hamrick, S. Li, W. Weltner Jr., *Chem. Phys. Lett.* **195**, 214 (1992).
- [27] H. Yoshida, A. Terasaki, K. Kobayashi, M. Tsukada and T. Kondow, *J. Chem. Phys.* **102**, 5960 (1995).

- [28] Q.- M. Ma, Z. Xie, J. Wang, Y. Liu, Y.- C. Li, *Phys. Lett. A* **358**, 289 (2006).
- [29] M. B. Knickelbein (*private communication*).
- [30] X. Xu (*private communication*).
- [31] C. Kittel, *Introduction to Solid State Physics* (Wiley, New York, 1996), 7th ed.
- [32] B. I. Min, T. Oguchi and A. J. Freeman, *Phys. Rev. B* **33**, R7852 (1986).
- [33] D. A. Hales, C. - X. Su, L. Lian, and P. B. Armentrout, *J. Chem. Phys.* **100**, 1049 (1994).
- [34] S. Yang and M. Knickelbein, *J. Chem. Phys.* **93**, 1533 (1990).
- [35] E. K. Parks, T. D. Klots, and S. J. Riley, *J. Chem. Phys.* **92**, 3813 (1990).
- [36] For $n = 14$, two degenerate ground states have been observed: one with icosahedral symmetry and other has hexagonal symmetry. The icosahedral structure is just slightly lower in energy compared to hexagonal structure and for Fig. 5.7, we have taken this icosahedron as the ground state, for which both $\langle r \rangle$ and $\langle n_c \rangle$ are higher than the neighbouring hcp ground states.
- [37] Mukul Kabir, D. G. Kanhere and Abhijit Mookerjee, *Phys. Rev. B* **73**, 224443 (2006).
- [38] T. M. Briere, M. H. F. Sluiter, V. Kumar and Y. Kawazoe, *Phys. Rev. B* **66**, 064412 (2002).
- [39] E. K. Parks, B. H. Weiller, P. S. Bechthold, W. F. Hoffman, G. C. Nieman, L. G. Pobo and S. J. Riley, *J. Chem. Phys.* **88**, 1622 (1988).
- [40] O. Dieguez, M. M. G. Alemany, C. Rey, P. Ordejon and L. J. Gallego, *Phys. Rev. B* **63**, 205407 (2001).
- [41] S. K. Nayak, S. N. Khanna, B. K. Rao and P. Jena, *J. Phys. Chem.* **101**, 1072 (1997).
- [42] N. N. Lathiotakis, A. N. Andriotis, M. Menon and J. Connolly, *J. Chem. Phys.* **104**, 992 (1996).

- [43] N. N. Lathiotakis, A. N. Andriotis, M. Menon and J. Connolly, *Eur. Phys. Lett.* **29**, 135 (1995).
- [44] M. Kabir, A. Mookerjee and A. K. Bhattacharya, *Eur. Phys. J. D* **31**, 477 (2004).
- [45] B. J. Winter, E. K. Parks and S. J. Riley, *J. Chem. Phys.* **94**, 8618 (1991).
- [46] G. H. Guvelioglu, P. Ma and X. He, *Phys. Rev. Lett.* **94**, 026103 (2005).
- [47] M. B. Knickelbein, *Chem. Phys. Lett.* **353**, 221 (2002).
- [48] M. Pellarin, B. Baguenard, J. L. Vialle, J. Lerme, M. Broyer, J. Miller and A. Perez, *Chem. Phys. Lett.* **217**, 349 (1994).
- [49] J. Garcia-Rodeja, C. Rey and L. J. Gallego, *Phys. Rev. B* **49**, 8495 (1994).
- [50] V. G. Grigoryan, D. Alamanova and M. Springborg, *Phys. Rev. B* **73**, 115415 (2006).
- [51] M. Kabir, D. G. Kanhere and A. Mookerjee *Phys. Rev. B* **75**, 214433 (2007).

Chapter 6

Structure, reactivity and electronic properties of V-doped Co clusters

In this chapter, we have carried out a detailed first-principles based study on structures and physico-chemical properties of V doped Co_{13} clusters. Our study nicely demonstrate the anomalous variation in reactivity towards H_2 molecules as reported experimentally. Moreover, it provides useful insight into the cluster chemical reactivity, which may help to design better catalytic processes. ¹

6.1 Introduction

The interest in studies of clusters is largely because of their technological applications as well as the possibilities of developing novel cluster-based materials using the size dependence of their properties. Doping of clusters is an important possibility in this direction. In recent times the fabrication of alloy clusters of different sizes with well defined, controlled properties by varying the composition and atomic ordering, has caught considerable attention. Bimetallic alloy clusters have been known and exploited for last few years in various catalytic reactions [1]. Varying the ratio of the two constituents, the distribution of the compounds at the surface may be altered. In this way, it is possible to tune the chemical reactivity at the surface of an alloyed cluster [2]. Few years before, Nonose *et al* [3] measured the reactivity towards H_2 of bimetallic Co_nV_m ($n > m$) clusters using a laser

¹This chapter is based on the following paper:

Soumendu Datta, M. Kabir, T. Saha-Dasgupta and A. Mookerjee; *Structure, reactivity and electronic properties of V-doped Co clusters* (Under preparation)

vaporization technique and reported strong cluster size and composition dependence of reactivity. Both V and Co are 3d transition metals. As V is located towards the left-hand side of periodic table, the substitution of Co by V atoms, one by one, should increase the reactivity of the alloy cluster towards H_2 molecules, as the left hand element V has a high reactivity towards H_2 in contrast to Co which has relatively low reactivity [4]. Fig. 6.1 shows the change in reactivity of $Co_{n-m}V_m$ ($n = 6, 8, 10, 11, 13$; $m = 1 - 4$) clusters with H_2 molecules as reported in Ref. [3]. It is seen that for Co_6 , Co_8 , Co_{10} and Co_{11} , the reactivity increases gradually as one substitutes the Co atom by V atom one by one, but for Co_{13} , there is a remarkable decrease in reactivity when a single Co atom is substituted by a V atom. However, the reactivity increases as the number of exchange V-atoms increase further upto $m = 3$, while the fourth V-atom substitution does not increase the reactivity any more. This indicates that somehow the geometrical structure of $Co_{12}V$ cluster becomes very rigid. In view of the high reactivity of elemental V, this sudden drop of reactivity of $Co_{12}V$ cluster was rather surprising. The authors speculated a plausible icosahedral structure for $Co_{12}V$ cluster with the active V atom at the cage centre. Therefore, the V atom, being shielded geometrically from H_2 by twelve surface Co atoms, might have less chance to interact with H-atoms. The chemisorption reactivity of cationic $Co_{13-m}V_m^+$ clusters [5] and anionic $Co_{13-m}V_m^-$ clusters [6] also shows similar type of variation as that of neutral $Co_{13-m}V_m$ clusters, which hints towards the dominant effect of geometric structure as compared to electronic structure. For clusters, the ionization potential (IP) depends on the position of the HOMO electronic level and for pure metal clusters, Whetten *et al* [7] have postulated that the reaction rate for cluster - H_2 dissociative chemisorption is determined by the charge transfer from HOMO to LUMO or antibonding orbital of the reactant gas, such as H_2 , in which an anti-correlation between IP and reaction coefficient could be observed. That means lower value of IP corresponds to higher reactivity and vice versa. However, ionization energies of Co_nV_m clusters by Hoshino *et al* [8] using photo-ionization spectroscopy show no such anti-correlation, again demonstrating the importance of geometrical structure. A rigorous first-principles study in terms of geometric and electronic effects is therefore very much needed to understand the anomalous nature of reactivity of $Co_{13-m}V_m$ ($m = 0-4$) clusters. In this chapter, we have carried out an *ab-initio* theoretical study on V doped Co_{13} clusters. Our study

consists of three major parts : first part consists of an exhaustive search for minimum energy structures for cluster of each composition, followed by stability analysis of these minimum energy structures in terms of various physical quantities in the second part, while the final part is an investigation of chemisorbed structures and understanding of cluster reactivity.

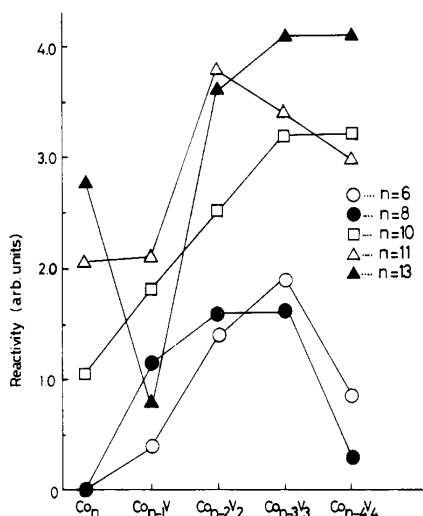


Figure 6.1: The reactivity of $\text{Co}_{n-m}\text{V}_m$ ($n > m$) clusters for reaction with H_2 . Open circles, closed circles, open squares, open triangles, and closed triangles correspond to measured values for $n = 6, 8, 10, 11$ and 13 , respectively. (adopted from Ref. [3])

6.2 Computational Details

The calculations have been performed using density functional theory, within the pseudopotential plane wave method. We have used the PAW pseudopotentials and PBE exchange-correlation functional for spin-polarized generalized gradient approximation. The $3d$ and $4s$ electrons were treated as valence electrons for the transition metal elements and the wave functions were expanded in the plane wave basis set with the kinetic energy cut-off of 335 eV. Reciprocal space integrations were carried out at the Γ point. Symmetry unrestricted geometry and spin optimizations were performed using conjugate gradient and quasi-Newtonian methods until all the force components were less than a

threshold value of 0.005 eV/Å. Simple cubic super-cells were used with the periodic boundary conditions, where two neighbouring clusters were kept separated by at least 12 Å vacuum space to make the interaction between the cluster images negligible. The cohesive energy (E_c) of a Co_nV_m alloy cluster was defined as

$$E_c(\text{Co}_n\text{V}_m) = mE(\text{V}) + nE(\text{Co}) - E(\text{Co}_n\text{V}_m) \quad (6.1)$$

where $E(\text{Co}_n\text{V}_m)$, $E(\text{Co})$ and $E(\text{V})$ were the total energies of Co_nV_m cluster, an isolated Co atom and an isolated V atom respectively. The second difference in energy for fixed size ($n+m = \text{constant}$) and variable composition was defined as

$$\Delta_2 E(\text{Co}_n\text{V}_m) = E(\text{Co}_{n+1}\text{V}_{m-1}) + E(\text{Co}_{n-1}\text{V}_{m+1}) - 2E(\text{Co}_n\text{V}_m) \quad (6.2)$$

It gives the relative stability of alloy clusters having nearby compositions.

6.3 Structure

Since chemical reaction of clusters takes place around the surface, the atomic arrangement and composition on the surface play an important role in chemical reactivity of alloyed clusters. Therefore, the first step towards theoretical modeling of alloy clusters is to determine their ground state structure. For V doped Co clusters ($\text{Co}_{13-m}\text{V}_m$; $m = 1-4$) also, we have followed the same way of structural optimization as we did for pure Co clusters in the previous chapter. That means we have considered several probable starting geometries having closed packed atomic arrangement and allowed each geometry to relax for all possible collinear spin configurations of atoms to determine the ground state structure having optimized geometry as well as optimized magnetic moment. However, the situation for alloy clusters is quite cumbersome as one has to deal with large number of starting geometries because of the presence of *homotops* (the term was first introduced by Jellinek [9, 10]). The *homotops* have the same number of atoms, composition and geometrical structure, but differ in the arrangement of doped atoms. For an Co_nV_m alloy cluster with fixed number of atoms ($N = m + n$) and composition (m/n ratio), a single geometrical structure will give, in principle, $\frac{N!}{m!n!}$ *homotops*. However, many of them may be symmetry equivalent and the number of inequivalent *homotops* will be much less than

the above mentioned value. So the variety of structures in alloy clusters is much richer than that of pure clusters and the potential energy surface of even a small clusters of few tens of atoms is of enormous complexity.

It is found that transition metal clusters prefer compact geometries to maximize the interaction between the rather localized d orbitals [11]. For cluster of 13 atoms, the three most compact and highly coordinated structures are the icosahedron, the cub-octahedron and the hexagonal closed packed geometries and they are usually found to be the ground state structures for pure transition metal clusters (cf. previous chapter). We have therefore considered these three geometries as the most probable starting structures. For pure Co_{13} cluster, the minimum energy state is a distorted hcp structure with total magnetic moment of $25 \mu_B$ and total cohesive energy 42.632 eV as we mentioned in the previous chapter. The structure has 22 triangular faces and 33 edges (cf. Fig. 6.2). Another distorted structure of hcp motif with total magnetic moment of $27 \mu_B$ and 0.14 eV above the minimum energy state, is the first isomer. The optimal icosahedral structure of total spin $31 \mu_B$ (structure having 20 triangular faces and 30 edges) is 0.17 eV higher than the minimum energy state and emerges as second isomer. Third isomer is a distorted cub-octahedron with total magnetic moment $25 \mu_B$ and it is 0.22 eV above the minimum energy state. Ground state, second and third isomers are shown in Fig. 6.2. It is to be noted that for pure Co_{13} cluster, all atomic moments are ferromagnetically coupled.

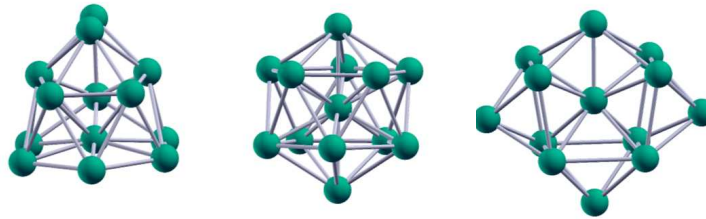


Figure 6.2: Structures of optimal hcp, icosahedron and cub-octahedron of pure Co_{13} cluster (from left to right respectively). Optimal hcp structure is the minimum energy state.

In case of single V atom doped Co_{12}V clusters, we have again considered the starting geometries of icosahedral, hcp and cub-octahedral symmetries, but depending upon the position of the singly doped V-atom at the centre position or on the surface, it can

give rise to several *homotops*. Again for each of the hcp and cub-octahedral geometries, there are two types of surface atoms in terms of orientation of the neighbours, while for icosahedral structure, all surface atoms are equivalent. So we have considered all these possible geometrical structures and for each of them, we have considered all possible collinear spin alignments during relaxation. Upon optimization of geometry and spin degrees of freedom, we found that an icosahedral structure of total magnetic moment $25 \mu_B$, with V atom doped at the centre position, is the minimum energy structure. There are several interesting points to note in this connection. First of all, the cohesive energy of this minimum energy structure is considerably higher (by 1.294 eV) than that of pure Co_{13} clusters, indicating its exceptional stability. V doped Co-clusters are found to prefer icosahedral growth pattern, instead of hcp growth pattern, as we observed in case of pure Co-clusters in the previous chapter. The single V-atom likes to be at the centre of the icosahedron and it is ferrimagnetically coupled with the the surface Co-atoms. The first isomer is also a central V-atom doped icosahedral Co_{12}V cluster, with total magnetic moment $23 \mu_B$ and it is about 0.46 eV above the minimum energy structure. Center V doped cub-octahedral Co_{12}V cluster with $23 \mu_B$ magnetic moment which has energy 0.70 eV higher than minimum energy icosahedral structure, is the second isomer. Third isomer is a centre V doped icosahedron with total magnetic moment of $27 \mu_B$. Center V doping in case of hcp cluster is less favourable and appears as fifth isomer in our calculation with total magnetic moment $25 \mu_B$ and energy 0.80 eV above the minimum energy structure. We also have considered the optimal structure of Co_{13} (distorted hcp) as starting structure and substituted the most coordinated central Co-atom by V-atom. After relaxation considering all possible spin alignments, it is seen that the shape of the optimal structure remains more or less same as that of optimal hcp Co_{13} cluster and energetically, it is the fourth isomer with total magnetic moment $23 \mu_B$. The most probable surface V-doping has a cub-octahedral structure with total magnetic moment $21 \mu_B$, but it is about 1.32 eV above the minimum energy structure. The structure of ground state and few isomers for Co_{12}V cluster are shown in Fig. 6.3.

Because of icosahedral growth preference and as the singly doped V-atom prefers the central site in case of Co_{12}V cluster, for more than one V atom doping, we consider only icosahedral structure and one V atom is definitely at the centre position, while residual

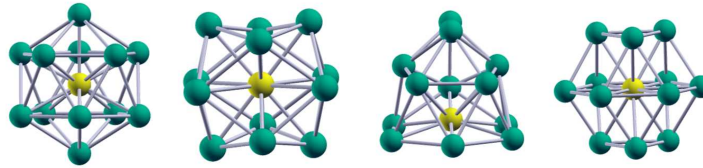


Figure 6.3: Structures of optimal icosahedron (minimum energy state), optimal cuboctahedron (2nd isomer) and hcp (4th and 5th isomers) (from left to right) for Co_{12}V cluster. Green dot represents Co atom, while yellow dot represents V-atom. Same convention is followed in next three figures.

V atoms reside on the surface. For Co_{11}V_2 cluster, the second V atom can replace any of the surface Co atom, as all surface sites of a 13-atom icosahedron, are equivalent. After relaxation for all possible spin configurations, it is found that the minimum energy structure has total magnetic moment $19 \mu_B$ and total cohesive energy 43.217 eV. The first and second isomers have magnetic moments $21 \mu_B$ and $17 \mu_B$ and they are 0.1 eV and 0.25 eV above the minimum energy state respectively. In the minimum energy structure, the centre V-atom is again ferrimagnetically coupled with surface Co atoms and has low magnetic moment like Co_{12}V cluster, while the surface V atom has maximum local magnetic moment and it is also ferrimagnetically coupled with other surface Co atoms.

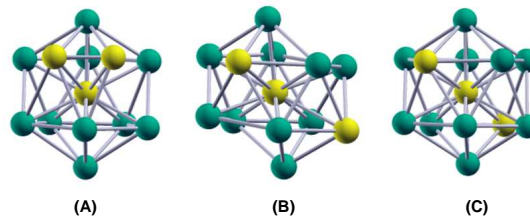


Figure 6.4: A, B, C represent the three inequivalent *homotops* in icosahedral Co_{10}V_3 structure having one V-atom always at the centre. The three structures are the optimal structures for the three types, however, type A is the most probable.

For Co_{10}V_3 cluster, depending upon the different positions of the two surface V atoms, there are three possible icosahedral structures as shown in Fig. 6.4. However, structure of type A where two surface V atoms are closest to each other, is the most favourable. Type A icosahedral structure with total magnetic moment $21 \mu_B$ is the minimum energy

state with ferrimagnetic coupling of central V-atom and ferromagnetic coupling of surface V-atoms with surface Co-atoms. Both central and surface V-atoms have small magnetic moments in this case. There are several closely spaced isomers of type A icosahedron with magnetic moments $19 \mu_B$, $13 \mu_B$, $23 \mu_B$ and $17 \mu_B$ which are just 0.038 eV, 0.079 eV, 0.09 eV and 0.15 eV above the minimum energy structure. The optimal structures of type B and type C are 0.204 eV and 0.313 eV above the minimum energy structure, respectively and both of them have same total magnetic moment of $13 \mu_B$.

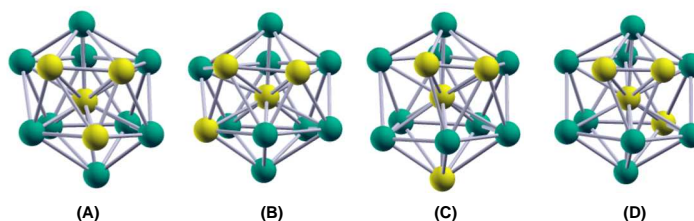


Figure 6.5: A, B, C, D represent the four probable *homotops* in icosahedral Co_9V_4 structure having one V-atom at the centre and two other V-atoms are closest to each other on the surface, while the position of fourth V-atom is varied. The four structures represented above are the optimal structures for the respective four types. However, type A is the most probable.

For Co_9V_4 , there are three V atoms on the surface. Considering two surface V atoms closest to each other (being tempted by the ground state configuration of Co_{10}V_3), different positions of third surface V atom can give rise to the four icosahedral configurations as shown in Fig. 6.5. After optimization, we found that type A is the most favourable structure where all the three surface V atoms are closest to each other and form an octahedron with the central V atom. The optimal structure of type A icosahedron has total magnetic moment $15 \mu_B$ and total cohesive energy 42.350 eV. Another type A icosahedrons with magnetic moments $13 \mu_B$, $19 \mu_B$, $21 \mu_B$ and $17 \mu_B$ are just 0.029 eV, 0.071 eV, 0.094 eV and 0.125 eV away. Optimal type B, type C and type D icosahedrons have total magnetic moments $15 \mu_B$, $13 \mu_B$ and $15 \mu_B$ respectively and they are 0.15 eV, 0.25 eV and 0.33 eV above the minimum energy structure.

It is therefore seen from our structural optimization that unlike hcp growth pattern of pure Co cluster, the V doped Co_{13} clusters prefer to adopt icosahedral packing. In such

clusters, the most coordinated central site is occupied by a V-atom, while the residual V-atoms sit on the surface. The surface V-atoms like to be closer to each other to form group, thereby imparting more distortion to the structure and significantly alter the local surface charge density. The central V-site in the minimum energy structures of all compositions, is always ferrimagnetically coupled and has lower magnetic moment. On the other hand, surface V-atoms can be ferrimagnetically or ferromagnetically coupled with surface Co-atoms and their local magnetic moments can be as low as central V-site or as high as surface Co-site, depending upon the distribution of surface charge density. Our prediction of icosahedral geometry for minimum energy states of V doped Co clusters is in accordance with the speculation of a closed shell geometry around a central site in Ref. [3, 5].

6.4 Stability analysis

The observed atomic arrangement of the minimum energy structures of $\text{Co}_{13-m}\text{V}_m$ clusters as described in the previous section depends critically on the balance of several parameters, like the relative strengths of various kinds of bonds present in the structure (for example, V doped Co clusters have maximum three types of bonds: Co-Co, Co-V and V-V bonds), relative atomic sizes, amount of charge transfer between two different species of atoms, HOMO-LUMO gap, abundance of states near Fermi energy etc. Below, we will try to understand the structural stability of clusters in terms of these parameters.

6.4.1 Cohesive energy

Fig. 6.6 shows the plot of cohesive energy of the minimum energy structures of $\text{Co}_{13-m}\text{V}_m$ clusters with increasing V concentration. With single V atom doping, the binding of the minimum energy cluster has increased considerably compared to optimal Co_{13} cluster. However, cohesive energies decrease sharply for higher concentration of V-atoms. For double and triple V-atom doping, the cohesive energies are above the dashed line indicating their more stability compared to pure Co_{13} , while for fourth V-atom doping, cohesive energy is even lower than that of pure Co_{13} . In order to see the relative stability among the nearby concentrations distinctly, we have plotted the second difference in cohesive energy

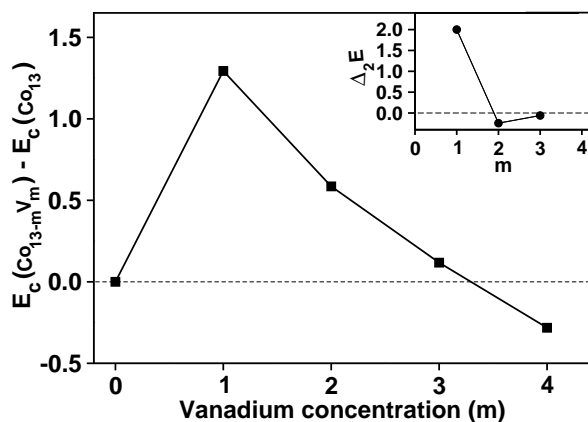


Figure 6.6: Cohesive energy of the minimum energy structures of $\text{Co}_{13-m}\text{V}_m$ clusters with respect to the cohesive energy of optimal Co_{13} cluster. The dashed line is the reference fixed at the cohesive energy of optimal Co_{13} . Inset shows the second difference ($\Delta_2 E$) in cohesive energy [as defined in Eqn. (6.2)] for Co_{12}V , Co_{11}V_2 and Co_{10}V_3 .

in the inset of Fig. 6.6. Again the sharp pick at $m = 1$ signals to the exceptional stability of single V-doped cluster compared to undoped or more than one V-doped clusters.

Table 6.1 shows our calculated cohesive energy and bond length of Co-Co, Co-V and V-V dimers. It is seen that V_2 dimer is the most stable and the bond length of V_2 dimer is also about 14% shorter than that in Co_2 dimer, while the cohesive energy and bond length of Co-V dimer are intermediate of Co_2 and V_2 dimers. For a bimetallic cluster, it is commonly found that if one of the homo-nuclear bonds is the strongest, then that species tends to be at the centre of the cluster. The highest stability of V_2 dimer therefore indicates the natural preference of central site by V-atom in V doped Co clusters. Also, smaller atoms tend to occupy the more sterically confined core, especially in icosahedral clusters. However, the radius of V atom is almost same as that of a Co atom and consequently, the substitution of central Co atom in icosahedral Co_{13} cluster by a V atom leaves the structure almost unaltered. In the optimal icosahedral structure of Co_{13} , the centre to vertex average distance is 2.334 Å and the average distance between two nearby vertices on the surface is 2.45 Å. For optimal Co_{12}V cluster, these values are

Table 6.1: Our calculated cohesive energy and bond length of Co_2 , Co-V and V_2 dimers. For comparison, we have also listed the experimental values for Co_2 dimer (Ref. [12]) and V_2 dimer (Ref. [13]).

Dimer	Cohesive energy (eV/atom)		Bond length (Å)	
	Theory	Expt.	Theory	Expt.
Co_2	1.45	1.72	1.96	2.31
CoV	1.53	...	1.87	...
V_2	1.81	2.47	1.72	1.77

Table 6.2: The average distances in Å between centre to vertex and between two nearby vertices for the minimum energy structures of all the studied clusters. For Co_{13} , the values correspond to the optimal icosahedron.

Bonds	Co_{13}	Co_{12}V	Co_{11}V_2	Co_{10}V_3	Co_9V_4
centre-vertex	2.334	2.344	2.354	2.375	2.398
vertex-vertex	2.455	2.465	2.476	2.499	2.509

2.344 and 2.465 Å respectively. The large gain in cohesive energy in Co_{12}V cluster over that of Co_{13} cluster is therefore due to enhanced cohesive energy of CoV dimer over that of Co_2 dimer. The V atom being at the centre position, there are maximum number of CoV dimers in Co_{12}V cluster.

For clusters having more than one V-atom doping, the central site is always possessed by a V-atom and the other V-atoms lie on the surface. With increasing V concentration on the cluster surface, the local environment of different surface sites becomes different which controls the overall cluster geometry and plays a crucial role in stability. The centre V-atom to surface V-atom distance in the minimum energy structure of Co_{11}V_2 icosahedron is 2.557 Å, however overall average centre to vertex distance is lower, 2.354 Å and average distance between two nearby vertices is 2.476 Å. For Co_{10}V_3 and Co_9V_4 clusters, surfaces have 2 and 3 V-atoms respectively, each having three types of surface bonds: V-V, V-Co and Co-Co. As the number of surface V-atoms increases, bond lengths become highly dispersive and the structures become more and more strained which can be realized from some open bonds in Fig. 6.4 and Fig. 6.5. In the minimum energy

structure of Co_{10}V_3 [cf. Fig. 6.4(A)], the average centre to vertex distance is 2.375 Å and the average distance between two nearby vertices on the surface is 2.499 Å. However, centre to vertex V-V average distance is 2.625 Å and average distance between two surface V-atoms is 1.890 Å. Similar trend has been found for minimum energy structure of Co_9V_4 [cf. Fig. 6.5(A)] where centre to surface V-V average distance is 2.660 Å and the average V-V bond length on the surface is 2.270 Å, while overall centre to vertex and vertex to vertex average distance are 2.398 Å and 2.509 Å respectively. In table 6.2, we have listed the average distances between centre to vertex as well as between two nearby vertices for the minimum energy structures of $\text{Co}_{13-m}\text{V}_m$ ($m = 0-4$). Interestingly, it is found that with the increase of V-concentration, both the distances are increasing, *i.e.* cluster volume increases which decreases the binding. Therefore, though the number of V-V bonds increases, which has better binding compared to Co-Co or Co-V bonds, the overall cohesive energy decreases monotonically as we go from Co_{12}V to Co_9V_4 by successive doping of V-atoms. It is then obvious that cluster geometry and the distribution of atoms on the cluster surface play an important role in deciding the cluster stability.

6.4.2 Spin gap

Analogous to HOMO-LUMO gap of a nonmagnetic cluster, one can define spin gaps for a magnetic cluster as,

$$\begin{aligned}\delta_1 &= - \left[\epsilon_{\text{HOMO}}^{\text{majority}} - \epsilon_{\text{LUMO}}^{\text{minority}} \right] \\ \delta_2 &= - \left[\epsilon_{\text{HOMO}}^{\text{minority}} - \epsilon_{\text{LUMO}}^{\text{majority}} \right]\end{aligned}\tag{6.3}$$

and the system is said to be stable if both δ_1 and δ_2 are positive *i.e.* the LUMO of the majority spin lies above the HOMO of the minority spin and vice versa. These represent the energy required to move an infinitesimal amount of charge from the HOMO of one spin channel to the LUMO of the other. The positions of HOMO and LUMO in both the spin channels and the values of δ_1 and δ_2 for the optimized structures of 13-atoms clusters of all compositions considered here are given in table 6.3. It is seen that both the spin gaps δ_1 and δ_2 are positive for all the clusters. Also Co_{12}V has maximum value of δ 's which again

Table 6.3: Positions of HOMO and LUMO in both the spin channels and the values of δ_1 and δ_2 for the optimized structures of all compositions.

clusters	Majority channel		Minority channel		Spin gaps (eV)	
	HOMO	LUMO	HOMO	LUMO	δ_1	δ_2
Co ₁₃	-3.602	-3.354	-3.480	-3.336	0.266	0.126
Co ₁₂ V	-3.930	-2.610	-3.387	-3.337	0.592	0.777
Co ₁₁ V ₂	-3.712	-2.832	-3.426	-3.321	0.391	0.594
Co ₁₀ V ₃	-3.407	-2.982	-3.336	-3.256	0.151	0.354
Co ₉ V ₄	-3.457	-3.024	-3.325	-3.174	0.283	0.300

indicates the highest stability of Co₁₂V cluster compared to the others. Because of this large spin gap, Co₁₂V has very low reaction tendency towards H₂ molecules. However, gap values decrease with increasing V concentration and therefore reactivity increases as observed experimentally [3].

6.4.3 Density of states

Fig. 6.7 shows the total density of states as well as total Co-contribution and total V-contribution for the minimum energy geometries of Co₁₂V, Co₁₁V₂, Co₁₀V₃ and Co₉V₄ clusters. Total *d*-projected DOS is also shown for each case. Close resemble between total DOS and total *d*-DOS indicates that cluster properties are mostly dominated by *d*-electrons. Structural stability of clusters as discussed in the previous section, is also obvious from the nature of total DOS. Majority spin channel of each cluster has a gap in DOS. This gap is maximum for Co₁₂V and it decreases as number of surface V-atoms increased. In the minority spin channel, there is finite amount of states at the Fermi energy and these are contributed solely by the exterior surface atoms, as the central atom does not have any contribution at the Fermi energy (cf. Fig. 6.8). It is also seen that for Co₁₂V, states are more localized and with increasing V-concentration, total DOS is gradually spreading out and DOS height, specially in the majority spin channel, decreases. This exceptional stability of Co₁₂V cluster towards H-adsorption is analogous to facts observed in case of extended surface : photoemission experiments by El-Batanouny *et al* [14] showed that a *H* atom adsorbed well both on the clean Nb(110) surface as well as on the surface

with a multilayer of Pd, but did not adsorb on Nb(110) surface with a monolayer of Pd and they showed this was due to the decrease of density of states of d -electrons of Pd near the Fermi level. Similar behaviour had been observed also in case of a monolayer of Pd on W(110) surface, in the experiment of CO-adsorption [15]. Equivalently, the central V atom of Co_{12}V corresponds to an early transition metal substrate and the exterior twelve Co atoms correspond to a late transition-metal monolayer.

In order to see the chemical activity of the central V-atom, we have plotted in Fig. 6.8, the total DOS of the central V-atom for each of the $\text{Co}_{13-m}\text{V}_m$ clusters. First of all, there is no finite states at Fermi energy, meaning central V-atom is not chemically active. It is seen that for all clusters, each of the majority and minority spin channels has two large peaks: one is deep below the Fermi energy and another is above Fermi energy. However, peak heights gradually decrease and states are broadened out and shifted towards higher energy with increasing V-concentrations. This means that presence of surface V-atoms induces some sort of chemical activeness to the central atom.

6.5 Chemisorption with H_2 molecules

In order to gain some understanding about the cluster chemical reactivity, we will investigate in this section the chemisorbed structures of $\text{Co}_{13-m}\text{V}_m$ clusters upon H_2 uptake. To check the robustness of our chemisorption calculations involving H-atoms, first we have calculated the cohesive energy, bond length and vibrational frequency of H_2 dimer. Our calculated values have been listed in table 6.4. These values are typical for gradient-corrected calculations of H_2 , which have been done before [16] and they agreed reasonably well with experiment [17].

Table 6.4: Our theoretically calculated cohesive energy, bond length and vibrational frequency for H_2 dimer. Experimental values in Ref. [17] are also given for comparison.

	Cohesive energy (eV)	bond length (Å)	Vibrational frequency (cm^{-1})
Theory	4.520	0.752	4339
Experiment	4.750	0.741	4395

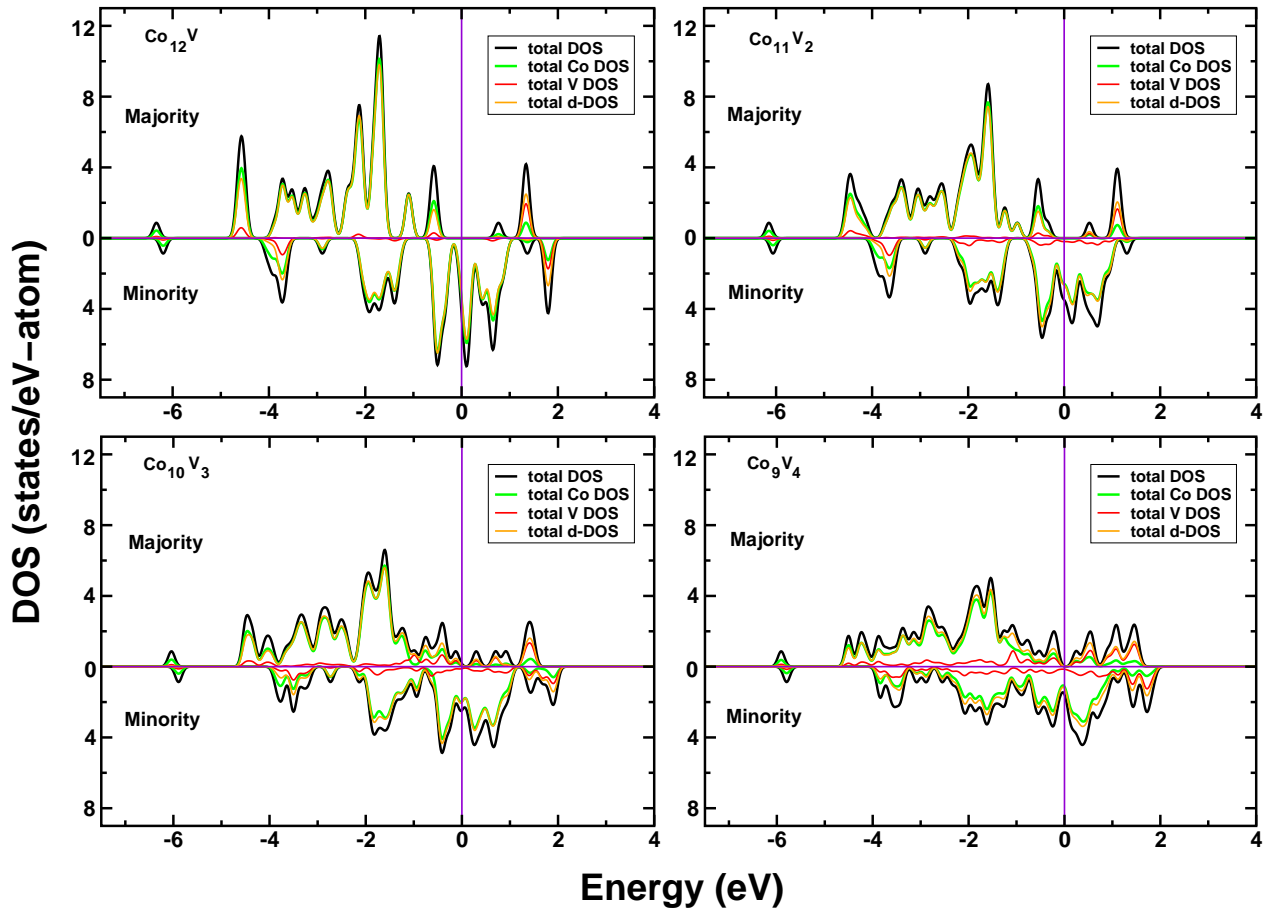


Figure 6.7: Total DOS per atom (black curve), total Co DOS per atom (green curve), total V-DOS per atom (red curve) and total d-projected DOS per atom (orange curve) for the optimal structures of Co_{12}V , Co_{11}V_2 , Co_{10}V_3 and Co_9V_4 . The smearing width is fixed at 0.1 eV. Vertical line through zero is the Fermi energy.

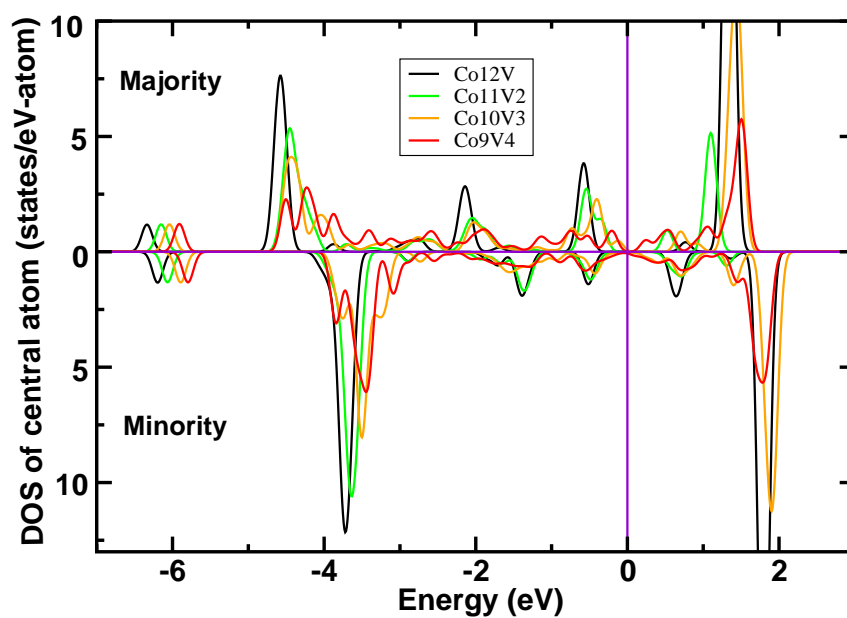


Figure 6.8: Total DOS of the central V atom in the optimal structures of Co₁₂V, Co₁₁V₂, Co₁₀V₃ and Co₉V₄. The Fermi energy is fixed at zero.

We have then performed an exhaustive search for minimum energy structure, taking H_2 at different possible places on the minimum energy structure of the corresponding bare cluster for each composition. Fig. 6.9 shows our calculated lowest energy chemisorption structures with H_2 for all compositions. First thing to notice is that H_2 molecule chemisorbs dissociatively in each case, *i.e* the distance between two H-atoms in the chemisorption structures is much larger than the H-H bond length of isolated H_2 molecule. The chemisorption gives rise to moderate perturbation to the structures and makes them more symmetric (*i.e* surface bonds are now less dispersive) by reducing the centre to surface V-V distance and increasing the surface V-V distance. There are three possible ways for H-atoms to be adsorbed on each cluster : on top of an atom (one fold), at bridge position between two atoms (two fold) and at the hollow site of a triangular plane on the cluster (three fold). Again, as the surface contains two species of atoms for $Co_{11}V_2$, $Co_{10}V_3$ and Co_9V_4 , then the one fold position can be on top of a surface V-atom or on top of a surface Co-atom. Two fold position can be the top of a V-V bond, Co-V bond or Co-Co bond. The Co-Co bond can be nearer to or away from V-site. Similarly, in triangular plane, there are several possibilities : (i) all the three atoms can be V-atoms (only possible for Co_9V_4), (ii) one Co atom and two V-atoms, (iii) two Co-atoms and one V-atom, (iv) all three are Co-atoms. We have considered all these possible combinations during optimization. It is, however, seen that in each optimized structure, H-atoms absorb at the hollow site on the surface and for $m \geq 2$, they prefer the association with local V. For example, in $Co_9V_4H_2$ one V-atom absorbs at the hollow site of V-V-V triangular plane and another on top of a V-V-Co triangular plane. For $Co_{11}V_2H_2$, the H-atoms appear to absorb at the bridge positions, but they are inclined with an angle such that the absorption tends toward a three fold configuration. The preference of more coordinated hollow site is likely due to geometric arrangements. It allows the H-atom to interact more with the V or Co atoms. On the other hand, V-site preference of H-atom is due to formation of stronger *s-d* bond with V-atom compared to that with Co-atom.

Fig. 6.10 shows the plot of chemisorption energy with increasing V-concentration, where the chemisorption energy is defined as

$$D_e(E) = E(Co_{13-m}V_m) + E(H_2) - E(Co_{13-m}V_mH_2) \quad (6.4)$$

It shows a minimum for $Co_{12}VH_2$ indicating lowest binding efficiency of $Co_{12}V$ with H.

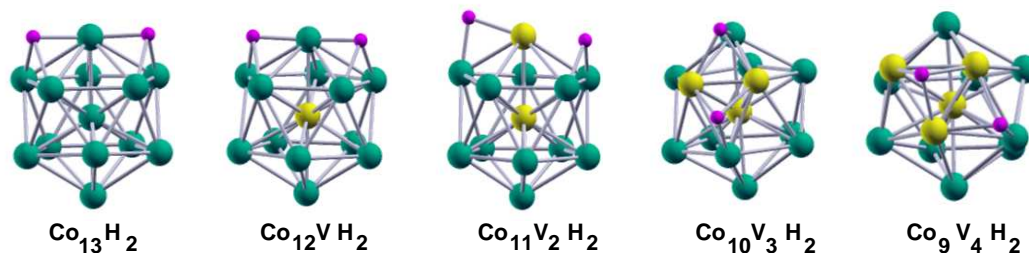


Figure 6.9: The calculated minimum energy chemisorption structures with H_2 on the minimum energy structures of $\text{Co}_{13-m}\text{V}_m$ ($m = 0-4$). It is clearly seen that hollow site on the surface is preferred by chemisorbed hydrogen.

However, chemisorption energy increases with increasing V concentration. The source of this chemisorption energy is the cluster rearrangement energy (*i.e* the energy change due to the geometrical rearrangement of the cluster upon chemisorption) and the efficient cluster-adsorbate bonding in presence of V due to more efficient *s-d* hybridization.

6.6 Summary and Conclusions

To summarize, we have studied the geometric and electronic structures of V doped Co_{13} clusters and their chemisorption towards hydrogen molecules using first principles density functional calculation. The lowest energy structures of all compositions prefer to have icosahedral geometry, unlike hexagonal symmetry preference of pure Co clusters. For Co_{12}V cluster, the single V atom prefers to sit at the central site, thereby guarded by all the surface Co atoms and cannot participate directly in the chemisorption reaction. Consequently reactivity of Co_{12}V becomes very less. On the other hand, for more than one V atom doping, the additional V-atoms reside on the surface and come in direct contact with chemisorbed H-atom and reactivity increases. Our calculated spin gaps and density of states explain nicely the stability of clusters and their trend towards chemisorption. In the chemisorbed structures, H-atoms adsorb dissociatively at the more coordinated hollow sites and they prefer V-site association due to stronger *3d-1s* hybridization. To have better insight into the chemisorption reaction, one needs to study the transition states for the

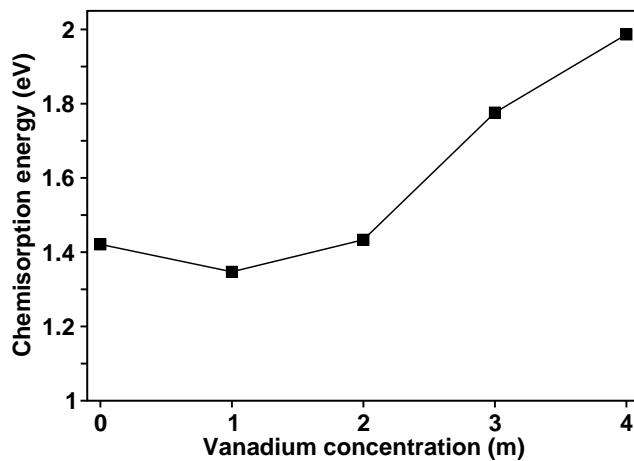


Figure 6.10: The calculated chemisorption energy of $\text{Co}_{13-m}\text{V}_m$.

optimal cluster of each composition and we believe that calculation of activation barriers will lead to same conclusion as we have predicted here.

Bibliography

- [1] J. H. Sinfelt, *Bimetallic Catalysts : Exxon Monograph*, J. Wiley, New York, 1983.
- [2] F. Besenbacher, I. Chorkendorff, B. S. Clausen, B. Hammer, A. M. Molenbroek, J. K. Norskov, I. Stensgaard, *Science* **279**, 1913 (1998).
- [3] S. Nonose, Y. Sone, K. Onodera, S. Sudo and K. Kaya, *J. Phys. Chem.* **94**, 2744 (1990).
- [4] G. C. Bond, *Heterogeneous Catalysis*, 2nd Ed.; Clarendon Press: Oxford, 1987.
- [5] A. Nakajima, T. Kishi, T. Sugioka, Y. Sone and K. Kaya, *J. Phys. Chem.* **95**, 6833 (1991).
- [6] A. Pramann, K. Koyasu and A. Nakajima, *J. Phys. Chem. A* **106**, 2483 (2002).
- [7] R. L. Whetten, D. M. Cox, D. J. Trevor and A. Koldor, *Phys. Rev. Lett.* **54**, 1494 (1985).
- [8] K. Hoshino, T. Naganuma, K. Watanabe, Y. Konishi, A. Nakajima, K. Kaya, *Chem. Phys. Lett.* **239**, 369 (1995).
- [9] *Theory of Atomic and Molecular Clusters*; Ed. J. Jellinek, Springer, Berlin, p. 277 (1999) and references therein.
- [10] J. Jellinek, E. B. Krissinel, *Chem. Phys. Lett.* **258**, 283 (1996); J. Jellinek, E. B. Krissinel, *Chem. Phys. Lett.* **272**, 301 (1997).
- [11] J. Alonso, *Chem. Rev.* **100**, 637 (2000).
- [12] A. Kant, B. Strauss, *J. Chem. Phys.* **41**, 3806 (1964).

- [13] S. P. Walch, C. W. Bauschlicher Jr., B. O. Roos and C. J. Nelin, *Chem. Phys. Lett.* **103**, 175 (1983).
- [14] M. El-Batanouny, M. Stronger, G. P. Williams and J. Colbert, *Phys. Rev. Lett.* **46**, 269 (1981).
- [15] M. V. Ruckman and M. Strongin, *Phys. Rev. B* **29**, 7105 (1984); D. Prigge, W. Schlerk and E. Bauer, *Surf. Sci. Lett.* **123**, L698 (1982).
- [16] G. Kresse and J. Hafner, *Surf. Sc.* **459**, 287 (2000).
- [17] K. P. Huber and G. Hertzberg, *Molecular Structure and Molecular Spectra IV: Constants of Diatomic Molecules* (Van Norstrand Reinhold, New York, 1979).

Chapter 7

Recursive approach to study transport properties of atomic wires

In this chapter, we will deal with 1D monoatomic wires and propose a recursive approach to study their electrical transport properties. The proposed method is based upon a real-space block-recursion technique with Landauer's formula being used to express the conductance as a scattering problem. To illustrate the method, we have applied it on a model system described by a single band tight-binding Hamiltonian. Results of our calculation therefore may be compared with the reported results on Na-atom wire. Upon tuning the tight-binding parameters, we can distinctly identify the controlling parameters responsible to decide the width as well as the phase of odd-even oscillations in the conductance.¹

7.1 Introduction

A mono-atomic quantum wire has a cross-section of one atom and is several atoms long. Such a system can be formed by pulling atomic contacts using a scanning tunneling microscope (STM) or a mechanically controllable break junction (MCBJ). The experimental evidences of formation of such atomic wires have been reported by Yanson *et al* [1] and Ohnishi *et al* [2]. However, issues involving electronic structure, transport properties and the influence of contacts with macroscopic leads or electrodes are still not fully settled.

¹This chapter is based on the following paper:

Soumendu Datta, T. Saha-Dasgupta and A. Mookerjee, *Recursive approach to study transport properties of atomic wire*, Eur. Phys. J. B, **66**, 57 (2008).

The most striking feature of such a mono-atomic wire is the non-monotonic behaviour of its conductance as a function of the number of atoms along its length. Oscillatory behaviour of conductance as a function of the length of the wire has been experimentally observed in Al, Pt and Ir wires by Smit *et al* [3], in Au and Ag wires by Thijssen *et al* [4], in Na wires by Krans *et al* [5] and in wires of atoms of higher valency by Yanson *et al* [1]. This oscillatory behaviour has been attributed to interference effect resulting from the changes in the connection between the wire and the edge of the electrode when new atoms are pulled into the wire.

Theoretically, the conductance of atomic wires can be calculated using the Landauer formalism in which one relates the conductance G in the linear response regime to the transmittance at the Fermi energy, $T(E_F)$, as : $G = (e^2/\pi\hbar)T(E_F)$. There are several numerical methods to calculate transmittance. They may be broadly classified into wavefunction and Green function methods. In wavefunction technique, one solves for scattering wavefunction of the system using methods like transfer matrix method [6]-[10], finite difference method [11] or by solving Lippman-Schwinger equation [12, 13]. All these methods use various level of approximations to describe the electronic structure of the system, starting from semi-empirical models like extended Hückel [6, 7] to fully atomistic descriptions based on DFT of Kohn and Sham. In most of the wave function methods, however, the electronic structure of the scattering region is resolved in detail, while the leads are modeled by a free electron gas [8, 9, 12, 13]. Alternatively, conductance can be calculated by Green's function method which does not require the explicit calculation of the scattering wave function. The main effort in this approach is to calculate the Green function of the central wire in the presence of the coupling to the leads. The effect of coupling to the leads is taken into account through self-energy terms. Various methods based on this approach, mainly differ in the choice of basis set used to represent the Hamiltonian and self-energy matrix, *e.g* Gaussians [14], numerical atomic orbitals [15], wavelets [16] and plane wave basis [17]. Although implementations within the Green function as well as the wavefunction approaches have been carried forward using various different techniques, it can be shown that the approaches are completely equivalent for non-interacting electrons [18]. In this chapter, we propose a combination of the scalar and vector recursion techniques [19]-[21] as a viable and efficient means to study the transport

properties within the general scheme of wavefunction approach of a lead-wire-lead system.

As a first step, starting from the junction point of the leads and the wire, we have used the recursion method of Haydock *et al* [19, 20] to map the quasi-1D semi-infinite leads with finite extensions along lateral directions onto equivalent chains. In the process, the information of the shape of the leads is encoded in the recursion coefficients. The recursion coefficients converge and the asymptotic part of the chains (or terminators) resembles periodic one-dimensional leads. This naturally divides the whole system unambiguously into an effective scattering region and two attached ballistic, periodic chain leads. The initial variation of the recursion coefficients contributes to the scattering region.

In the second step, the scattering matrix has been calculated by solving the Schrödinger equation using the vector or block recursion method of Godin and Haydock [21] and applying the wave-function matching conditions at the lead-wire interfaces. In the final step, we have applied Landauer's formula to express the conductance of the quantum wire.

The advantage of the proposed method is that it is a real space based method. Moreover, to solve the scattering problem, one does not need to calculate the wave function explicitly. By putting the boundary conditions at the lead-wire junctions and at the end of vector chain, one can directly calculate the scattering matrix. The basic inputs in the above described procedure are the TB Hamiltonians for the wire and the leads. In order to illustrate the method, we have applied it to a model system described by a single-band TB Hamiltonian. We demonstrate the validity of this approach by comparing the results obtained out of a simple model system with the reported results on monoatomic Na-wire calculated from first-principles. Moreover, by tuning the TB parameters of the wire and the leads we have provided a detailed understanding of the various features of the problem beyond what has been reported earlier [22]-[30]. The proposed technique being based on recursion, relies on the sparseness of the starting Hamiltonian. The coupling of this method to fully atomistic DFT description of the electronic structure, however, can be easily achieved in terms of Wannier function based Hamiltonian constructed out of DFT calculations [17, 31].

7.2 Method

7.2.1 Converting quasi-1D lead to effective 1D chain and detection of effective scattering region

Each lead with finite lateral dimension of $N_x \times N_y$ is described by a Hamiltonian in a tight-binding basis $\{|i\mu\rangle\}$ where i labels a site and μ a particular channel, *e.g.* in LCAO type formulations, this would be the angular momentum labels (ℓ, m) :

$$\begin{aligned} H_{\text{lead}} &= \sum_{i,\mu} \sum_{j,\mu'} \hat{H}_{ij}^{\mu\mu'} |j, \mu'\rangle \langle i, \mu| \\ \hat{H}_{ij}^{\mu\mu'} &= \epsilon_{\text{lead}}^{i\mu} \delta_{\mu\mu'} \delta_{ij} + t_{\text{lead}}^{i\mu, j\mu'} \delta_{j, i+\chi} \end{aligned} \quad (7.1)$$

where χ are the N_i nearest neighbours of site i on the lattice. To obtain the equivalent ‘chain’ of 3d lead, we use scalar recursion technique. The basic formalism of scalar recursion method has been discussed in section 2.3.2 of chapter 2. This recursion method converts the tight-binding basis $\{|i\mu\rangle\}$ to a new one : $\{|n\rangle\rangle\}$.

Taking $|1\rangle\rangle = |1\mu\rangle$ as the starting state, where 1 labels the site at the middle of the cross-sectional edge of the lead where it is connected to the wire (cf. Fig. 7.1a) and μ is any one of the ‘orbital’ indices, we generate :

$$|n+1\rangle\rangle = H_{\text{lead}}|n\rangle\rangle - \alpha_n^\mu |n\rangle\rangle - \beta_n^{\mu 2} |n-1\rangle\rangle \quad (7.2)$$

and

$$\alpha_n^\mu = \frac{\langle\langle n|H_{\text{lead}}|n\rangle\rangle}{\langle\langle n|n\rangle\rangle} \quad \beta_n^\mu = \frac{\langle\langle n-1|H_{\text{lead}}|n\rangle\rangle}{[\langle\langle n|n\rangle\rangle \langle\langle n-1|n-1\rangle\rangle]^{1/2}} \quad (7.3)$$

The equivalent Hamiltonian in this new basis is tri-diagonal (chain-like) :

$$\bar{H}_{\text{lead}}^\mu = \sum_{n=1}^{\infty} \alpha_n^\mu |n\rangle\rangle \langle\langle n| + \beta_n^\mu (|n\rangle\rangle \langle\langle n+1| + |n+1\rangle\rangle \langle\langle n|) \quad (7.4)$$

where the index n labels the ‘atoms’ of the equivalent linear chain for the μ channel and α_n^μ and β_n^μ signify its on-site and the hopping terms respectively. The sequences $\{\alpha_n^\mu, \beta_n^\mu\}$ converge, so that for a given error tolerance ε , there exists an integer c such that for $n > c$, $|\alpha_n^\mu - \alpha_c^\mu| < \varepsilon$ and $|\beta_n^\mu - \beta_c^\mu| < \varepsilon$. The ‘terminator’ approximation puts $\alpha_n^\mu, \beta_n^\mu = \alpha_c^\mu, \beta_c^\mu$ for all $n > c$. The initial c ‘sites’ of both the equivalent input and output

chain leads, therefore, contribute to the effective scattering region in addition to the wire. The wire of length $2M$ atoms is described by a Hamiltonian in the tight-binding basis as:

$$\begin{aligned} H_{\text{wire}} &= \sum_{i,\mu} \sum_{j,\mu'} \widetilde{H}_{ij}^{\mu\mu'} |j, \mu'\rangle \langle i, \mu| \\ \widetilde{H}_{ij}^{\mu\mu'} &= \epsilon_{\text{wire}}^{i\mu} \delta_{\mu\mu'} \delta_{ij} + t_{\text{wire}}^{i\mu, j\mu'} (\delta_{j, i+1} + \delta_{j, i-1}) \end{aligned} \quad (7.5)$$

The opposite ends of the wire are coupled to the semi-infinite effective 1D leads via hopping matrix element t_c . Note that as the starting states in the old and new basis sets are same in the recursion process, the coupling coefficient t_c remains same during the change of tight-binding basis set. The procedure therefore converts the whole system into an infinite linear chain in which effective scattering region is of extension $2M + 2c$ sites and the rest represents the ballistic parts of the leads which do not participate in the scattering process.

7.2.2 Calculation of the scattering matrix

Let us consider $2M + 2c = 2N$ and for convenience, rename the sites as follows (cf. Fig. 7.1b) :

$$\begin{aligned} H &= \sum_{n,\mu} \sum_{n',\mu'} \widehat{H}_{nn'}^{\mu\mu'} |n', \mu'\rangle \langle n, \mu| \\ \widehat{H}_{nn'}^{\mu\mu'} &= \tilde{\epsilon}_n^{\mu} \delta_{\mu\mu'} \delta_{nn'} + v_n^{\mu\mu'} (\delta_{n', n+1} + \delta_{n', n-1}) \end{aligned} \quad (7.6)$$

with

$$\tilde{\epsilon}_n^{\mu} = \begin{cases} \alpha_c^{\mu} & n \leq n_1 & \text{left ballistic lead} \\ \alpha_{c+1-n}^{\mu} & n_1 < n \leq n_2 & \text{left scattering lead} \\ \epsilon_{\text{wire}}^{\mu} & n_2 < n \leq n_3 & \text{scattering wire} \\ \alpha_{n-(c+2M)}^{\mu} & n_3 < n \leq n_4 & \text{right scattering lead} \\ \alpha_c^{\mu} & n > n_4 & \text{right ballistic lead} \end{cases} \quad (7.7)$$

and

$$v_n^{\mu\mu'} = \begin{cases} \beta_c^\mu & n \leq n_1 & \text{left ballistic lead} \\ \beta_{c-n}^\mu & n_1 < n < n_2 & \text{left scattering lead} \\ t_c^{\mu\mu'} & n = n_2 & \text{left junction} \\ t_{\text{wire}}^{\mu\mu'} & n_2 < n < n_3 & \text{scattering wire} \\ t_c^{\mu\mu'} & n = n_3 & \text{right junction} \\ \beta_{n-(c+2M)}^\mu & n_3 < n \leq n_4 & \text{right scattering lead} \\ \beta_c^\mu & n > n_4 & \text{right ballistic lead} \end{cases} \quad (7.8)$$

where $n_1 = 0$, $n_2 = c$, $n_3 = c + 2M$ and $n_4 = 2c + 2M = 2N$.

We then compute the scattering matrix of the above mentioned system using the block or vector recursion technique introduced by Godin and Haydock [21]. The essence of the vector recursion technique is the block tridiagonalization of the system Hamiltonian by changing to a new orthogonal set of vector basis, with the restriction that the ballistic part of effective 1D lead Hamiltonian remains unchanged. In this last aspect, it differs from the standard Lanczos method [20]. The numerical stability of this method [32] has been established in studying problems related to Anderson localization and quantum percolation model [33] and layering transition in 2D nano-strip [34] previously. Below we describe the method briefly.

Let us consider, for the sake of demonstration, that we have two 1D ballistic leads, one incoming and another outgoing connected to the opposite ends of the scattering region at positions $|1\rangle$ and $|2N\rangle$ (cf. Fig. 7.1b). The leads and the scatterer have $\mu = 1, 2, \dots, L$ scattering channels. The members of the new basis are generated by clubbing the input and output leads together as the vector lead and so is the scattering region (cf. Fig. 7.1c). The lead states are chosen to be

$$|\Phi_n\rangle = \begin{pmatrix} |n, \mu = 1\rangle & |n, \mu = 2\rangle & \dots & |n, \mu = L\rangle \\ |m, \mu = 1\rangle & |m, \mu = 1\rangle & \dots & |m, \mu = L\rangle \end{pmatrix}^\dagger \quad (7.9)$$

with $m = 2N + 1 - n$ and $n = 0, -1, -2, \dots, \infty$. The starting state within the scattering region is chosen to be

$$|\Phi_1\rangle = \begin{pmatrix} |1, \mu = 1\rangle & |1, \mu = 2\rangle & \dots & |1, \mu = L\rangle \\ |2N, \mu = 1\rangle & |2N, \mu = 2\rangle & \dots & |2N, \mu = L\rangle \end{pmatrix}^\dagger$$

The subsequent members of the basis are generated from

$$B_2^\dagger |\Phi_2\rangle = (H - A_1) |\Phi_1\rangle,$$

$$B_{n+1}^\dagger |\Phi_{n+1}\rangle = (H - A_n) |\Phi_n\rangle - B_n |\Phi_{n-1}\rangle \quad \text{for } n \geq 2 \quad (7.10)$$

The matrix inner product is defined as the $2L \times 2L$ matrix

$$\{\Phi_1 | \odot | \Phi_1 \rangle = \begin{pmatrix} A & B \\ C & D \end{pmatrix}$$

where the $L \times L$ matrices A, B, C and D are :

$$\begin{aligned} A &= \langle 1\mu | 1\mu' \rangle & B &= \langle 1\mu | 2N\mu' \rangle \\ C &= \langle 2N\mu | 1\mu' \rangle & D &= \langle 2N\mu | 2N\mu' \rangle \end{aligned}$$

If this matrix is I then the states are called orthogonal.

It can be shown that the $2L \times 2L$ matrices A_n and B_n are block-tridiagonal members of the matrix representation of the Hamiltonian in the new basis:

$$A_n = \{\Phi_n | \odot H | \Phi_n \rangle \quad B_n = \{\Phi_n | \odot H | \Phi_{n-1} \rangle \quad (7.11)$$

so that the transformed Hamiltonian matrix can be divided in $2L \times 2L$ blocks, with only non-zero diagonal and sub-diagonal blocks.

The wave function $|\Psi\rangle$ may be represented in this new basis by a set $\{\psi_n\}$ so that $|\Psi\rangle = \sum_n \psi_n |\Phi_n\rangle$. These wave function amplitudes ψ_n also satisfy an equation identical with Eqn. (7.10).

In the ballistic part of the effective 1D lead chain, the onsite and hopping terms do not vary. Therefore, electron potential must be periodic in this region and the solution to the Schrödinger's equation in the μ channel of the ballistic leads is traveling Bloch wave : $A \sum_m \exp[\pm im\theta^\mu] |m\rangle$. As the wave travels in the leads, the phase of its wave function changes by $\theta^\mu = \cos^{-1} [(E - \alpha_c^\mu) / (2\beta_c^\mu)]$, where E is the energy of the incoming electron. In order to have only propagating solutions, we fix E as real and $|E - \alpha_c| < 2\beta_c$. This sets the energy window. This is reasonable because eventually only the propagating modes enter in the expression of transmission matrix elements, as evanescent modes do not contribute to the transmission directly [35]. In the μ channel of the incoming lead, the incident and the reflected waves can be expressed as a sum

$$A \sum_m \sum_{\mu'} \left[\exp(im\theta^\mu) \delta_{\mu\mu'} + r^{\mu\mu'}(E) \exp(-im\theta^{\mu'}) \right] |m\rangle$$

The second term is the reflected wave in the μ channel from incident waves in μ' channels.

In the μ channel of the output lead there is a transmitted wave from incident waves in μ' channels [36]

$$A \sum_m \sum_{\mu'} t^{\mu\mu'}(E) \exp(-im\theta^{\mu'}) |m\rangle$$

$r^{\mu\mu'}(E)$ and $t^{\mu\mu'}(E)$ are the complex reflection and transmission coefficients. The boundary conditions are then imposed from the known solution in the leads at the junction labeled by 0 and 1:

$$\psi_0 = \begin{pmatrix} \sum_{\mu'} [\delta_{\mu\mu'} + r^{\mu\mu'}(E)] \\ \sum_{\mu'} t^{\mu\mu'}(E) \end{pmatrix} \quad (7.12)$$

$$\psi_1 = \begin{pmatrix} \sum_{\mu'} \left\{ \exp[i\theta^\mu] \delta_{\mu\mu'} + r^{\mu\mu'}(E) \exp[-i\theta^{\mu'}] \right\} \\ \sum_{\mu'} t^{\mu\mu'}(E) \exp[-i\theta^{\mu\mu'}] \end{pmatrix} \quad (7.13)$$

The amplitude at the n -th basis ψ_n may be written as

$$\psi_n = X_n \psi_0 + Y_n \psi_1 \quad (7.14)$$

where X_n and Y_n satisfy the same recurrence relation as Eqn. (7.10) with EI replacing H and also satisfy the boundary conditions $X_0 = I$ and $X_1 = 0$, while $Y_0 = 0$ and $Y_1 = I$. Note that X and Y are $2L \times 2L$ matrices and ψ_n 's are column matrices of dimension $2L$.

This new basis terminates after $\nu = N$ steps, as the rank of the space spanned by the original tight-binding basis remains unchanged after the transformation. Hence the recursion also terminates after ν steps. This gives an additional boundary condition,

$$X_{\nu+1} \psi_0 + Y_{\nu+1} \psi_1 = 0_{2L \times 2L}. \quad (7.15)$$

If we now interchange the incoming and outgoing leads, we get a similar pair of equations for $r'^{\mu\mu'}$ and $t'^{\mu\mu'}$, the transmission and reflection coefficients for a wave incident from the second lead. Time-reversal symmetry demands that t must be the same for waves of the same energy incident from either lead so that $t^{\mu\mu'} = t'^{\mu\mu'}$. In addition, $r^{\mu\mu'}$ and $r'^{\mu\mu'}$ differ only by a phase factor. Solving these equations for the S-matrix in the effective scattering region, one has,

$$\begin{aligned} S(E) &= -(X_{N+1} + Y_{N+1}E^*(\theta))^{-1}(X_{N+1} + Y_{N+1}E(\theta)) \\ &= \begin{pmatrix} r^{\mu\mu'}(E) & t^{\mu\mu'}(E) \\ t^{\mu\mu'}(E) & r'(E)^{\mu\mu'} \end{pmatrix} \end{aligned} \quad (7.16)$$

where

$$E(\theta) = \begin{pmatrix} \exp(i\theta^\mu)\delta_{\mu\mu'} & 0 \\ 0 & \exp(i\theta^\mu)\delta_{\mu\mu'} \end{pmatrix}$$

The various steps of our approach are shown schematically in Fig. 7.1.

The conductance is then given by Landauer formalism. It expresses the electronic conductance in one-dimensional conductor as a quantum mechanical scattering problem and relates to the total transmission probability of the electron at the Fermi level [37], $T(E_F)$, as

$$G = \left(\frac{e^2}{\pi\hbar}\right) T(E_F) = \left(\frac{e^2}{\pi\hbar}\right) \left| (1/L) \sum_{\mu\mu'} t^{\mu\mu'}(E_F) \right|^2 \quad (7.17)$$

We have assumed in our derivation the leads to have finite lateral dimensions, though in actual experiments, the leads are three dimensional. In order to study the influence of the extend of the lateral dimension of the leads, we have checked our results with increasing size of the lateral cross-section of the leads. Though the quantitative values do change with the change of the lateral dimension, the qualitative nature holds good in every case. In addition, we find for sufficiently large choice of lateral cross-section, the recursion coefficients (α, β) for the leads converge to that of a bulk system (see for details section 7.3.1), indicating for such large lateral cross-section, the leads behave as truly three-dimensional leads. The other approach to the problem could have been inclusion of periodic boundary condition as have been adopted in various works [15]-[18],[31, 35, 38, 39]. If we impose periodic boundary conditions on the lead surfaces, only

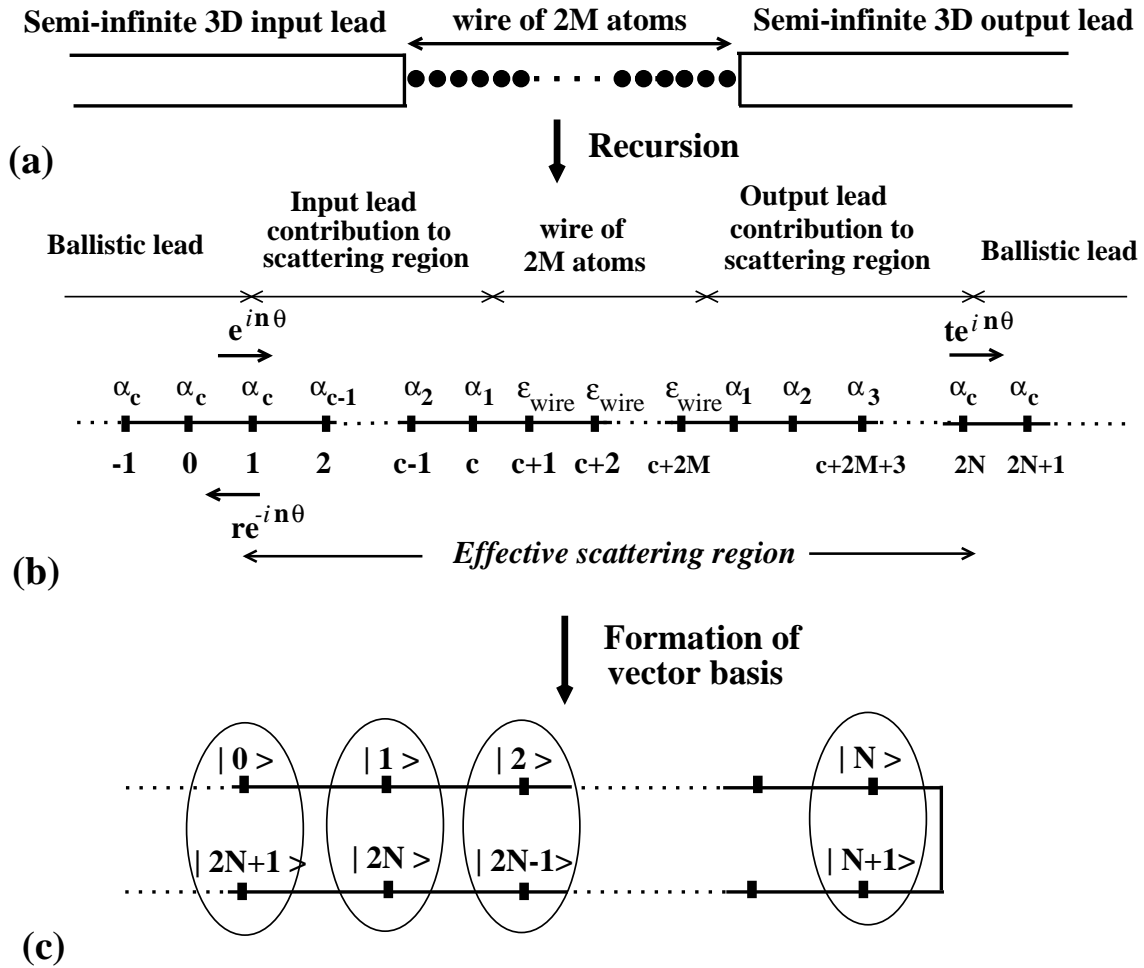


Figure 7.1: Recursive reduction of (a) a system of two quasi 1D semi-infinite leads plus 1D wire into (b) a system of infinite linear chain. The numbering of sites of the equivalent 1D infinite chain is shown in (b). The directions of incident wave $e^{in\theta}$ to the scattering region, the reflected wave $re^{-in\theta}$ and transmitted wave $te^{in\theta}$ from the scattering region are shown with arrows. (c) Formation of vector basis by folding the infinite chain and clubbing the two sites together.

those modes which are consistent with the boundary conditions can travel through them. In an earlier paper we have shown [40], that it is possible to change over from a site to a mode basis and reformulate the vector recursion in the new basis. The lead is broken up into slices perpendicular to its length and the composite site label i is partitioned into two : one is the slice label s and the other is the position on this slice k . The basis $\{|sk\rangle\}$ is then converted into a slice-mode basis $\{|s\nu\rangle\}$ and the Hamiltonian is expressed in this new basis. Exactly as the Hamiltonian [Eqn. (7.6)] mixes orbital labeled channels because of off-diagonal terms $v^{\mu\mu'}$, in the mode based formalism off-diagonal terms in the corresponding Hamiltonian causes the outgoing wave to be of a mixed mode type even if the incoming wave is in a single mode. Otherwise, the formal methodology is identical in the two cases. The interested reader is referred to the paper referenced above for the details. At this point, it is important to mention that recently K. K. Saha *et al* have suggested a method that is able to take into account periodicity in the leads without assuming the periodicity of the conductor in the lateral direction by solving the Dyson equation [41].

7.3 Application

7.3.1 The model

Since our aim here is to propose a method rather than to evaluate the properties of any particular system in quantitative detail, we present the study of a simple model system. It consists of a wire, few atoms long, sandwiched between two identical semi-infinite leads. Both the wire and the leads have only a single channel ($L = 1$) corresponding to single s -band. The cross-sectional size of each lead in our calculation was 5×5 . The atoms in the leads form a simple cubic lattice. Each lead is described by a single-band nearest-neighbour TB Hamiltonian. Two TB parameters in Eqn. (7.1) : the on-site and the hopping terms, which are material specific in realistic cases, have been chosen as $\epsilon^i = \epsilon_{\text{lead}} = 0$ and $t^{ij} = t_{\text{lead}} = 2$ in some arbitrary energy unit. As a first step, we performed scalar recursion on the leads to convert them into equivalent chains and determined the contribution of each lead to the effective scattering region. We took the starting state of recursion to be the sites which bound the leads to the wire. For a simple cubic lead,

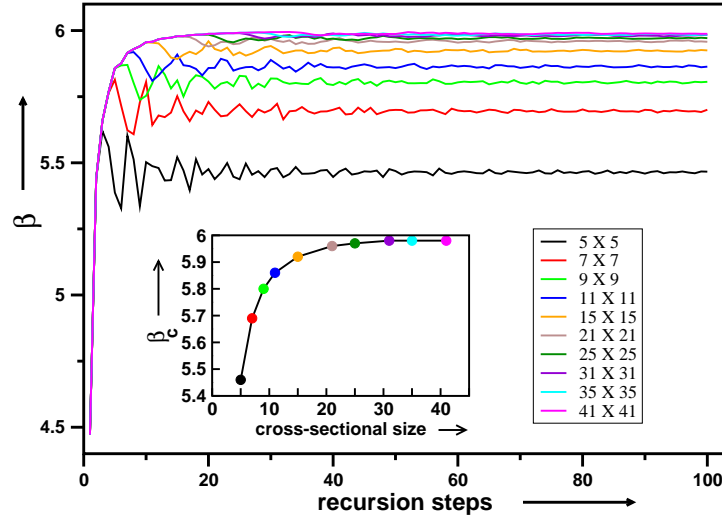


Figure 7.2: Variation of recursion coefficient β with recursion steps for different cross-sectional sizes of the lead, with $t_{lead} = 2.0$ and $\epsilon_{lead} = 0.0$. The lower left inset shows the variation of converged values of β (β_c) with cross-sectional size.

the recursion coefficients $\alpha_n = \epsilon_{lead} = 0$ while the other coefficients β_n fluctuate with recursion steps converging to an asymptotic value β_c . The convergence of β_n depends on the lattice structure and lateral cross-sectional size of lead. We have not used any periodic boundary conditions in the lateral direction. To see the finite size effect of lead in the lateral direction, we have repeated our calculations for different cross-sectional sizes. Convergence of β with recursion steps for different cross-sectional sizes is shown in Fig. 7.2. As the cross-section increases, the number of recursion steps required to converge β decreases (*i.e.* size of effective scattering region decreases which facilitates to easier computational execution). Variation of converged value of β (β_c) with lateral cross-sectional size of the lead is shown within the inset. Notice after a certain cross-sectional size (30×30 with the present choice of parameters), β converges to that of the bulk cubic system, which is 6 for choice of $\epsilon_{lead} = 0$ and $t_{lead} = 2.0$. This implies that there is no further effect of finite cross-section on β_c and therefore on conductance. In changing cross-section from 5×5 to 30×30 , β_c changes by 9 % (The change is mostly coming in going from 5×5 to 11×11 and after that change is very minute). The corresponding

change in conductance is much smaller : 5 % for even numbered wire, less than 1 % for odd numbered wire (cf. Fig. 7.3). We have checked that qualitatively results are same for any cross-sectional size, but if one is concerned about the quantitative value, then convergence of β_c with cross-sectional size has to be checked. For our chosen case, β_n converged after around 80 recursions. So in our calculation, c was taken to be 80 and $\beta_n = \beta_{80}$ for $n \geq 80$. For a model simple cubic lead, the Fermi energy is at $E_F^{\text{lead}} = \epsilon_{\text{lead}}$ which is obvious from the dispersion relation $E = \epsilon_{\text{lead}} + 6t_{\text{lead}} \cos(ka)$ for a half-filled band with Fermi wave number $k_F = \pi/2a$. Fermi energy E_F of the lead-wire-lead system tends to align with the Fermi energy of the semi-infinite lead. Conductance is therefore calculated at $E_F = \epsilon_{\text{lead}}$.

7.3.2 Results and discussions

Our calculated conductance as a function of number of atoms in the wire is shown in Fig. 7.4. The inter-atomic hopping within the wire was fixed to $t_{\text{wire}} = 2 = t_{\text{lead}}$. To consider the effect of charge transfer between the leads and the wire [$\Delta\epsilon = \epsilon_{\text{lead}} - \epsilon_{\text{wire}} \neq 0$], we considered the cases $|\Delta\epsilon| = 0.2$ and $|\Delta\epsilon| = 0.4$ along with no charge transfer condition $|\Delta\epsilon| = 0$. Non zero values of $\Delta\epsilon$ were achieved by changing ϵ_{wire} . For each case, we considered three types of coupling between lead and atomic wire, given by lead-wire hopping coefficient t_c : (i) $t_c = 0.9 t_{\text{lead}}$ for weak coupling, (ii) $t_c = t_{\text{lead}}$ for direct coupling and (iii) $t_c = 1.1 t_{\text{lead}}$ for strong coupling.

The odd-even oscillation in conductance for no charge transfer situation is obvious from Fig. 7.4a *i.e* wires with odd-number of atoms have larger conductance as compared to the even numbered ones, for all the three types of couplings. In this ideal case of no charge transfer situation, all odd numbered atomic wires have conductances equal to quantum unit $G_0 = (e^2/\pi\hbar)$ for all the three coupling cases, while for even numbered wires the conductances are lower. The conductance of even-numbered wires decreases as one moves from strong to direct to weak coupling. This means that the amplitude of conductance oscillation is a maximum for the weak coupling case ($t_c = 0.9 t_{\text{lead}}$) and it is a minimum for the strong coupling case ($t_c = 1.1 t_{\text{lead}}$). Similar results have been predicted by Khomyakov *et al* for a system of 1D wire connected with 1D leads using tight-binding

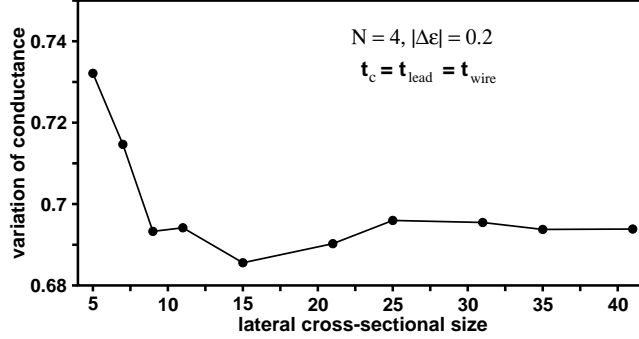


Figure 7.3: Variation of conductance with cross-sectional sizes for an even numbered wire, $N = 4$ considering direct coupling and $|\Delta\epsilon| = 0.2$. Variation in conductance is around 5% for even numbered wire. For odd numbered wire (not shown in the above plot), it is less than 1%.

calculation [26] which expressed the dependence of conductance on t_c for even numbered wire as

$$G = G_0 \frac{4t_c^4/t_{\text{wire}}^2}{[1 + 4t_c^4/t_{\text{wire}}^2]^2}$$

It follows the same trend as observed in the top panel of Fig. 7.4. Another point to notice from Fig. 7.4a is that the length of the wire does not have any effect in this case either on amplitude or phase of the oscillation. All odd numbered atomic wires and also all even numbered atomic wires have equal conductances for a fixed coupling type. The odd-even oscillations for our single band model system is in agreement with the results on Na-atom wires [22]-[28].

For $|\Delta\epsilon| = 0.2$ in Fig. 7.4b, the odd-even oscillation in conductance is again obvious within the range of our plot. However, a close view to these curves, indicates that the conductance of the odd numbered atomic wires gradually decreases while that of the even numbered atomic wires slowly increases. If we increase the number of atoms in the wire to more than 10 (not shown in Fig. 7.4), we find that the parity of conductance oscillation changes from odd-even to even-odd, *i.e.* even numbered atomic wires now have larger conductance than the conductance of odd numbered atomic wires.

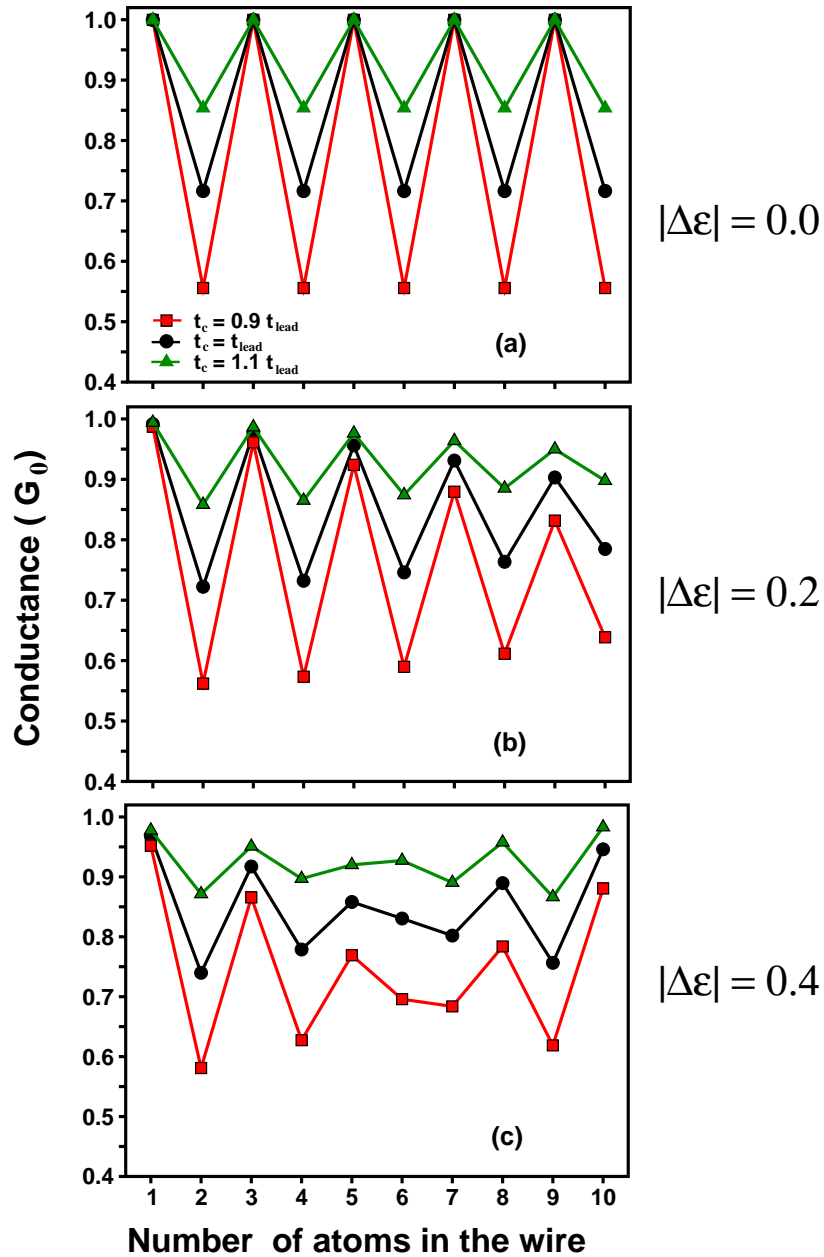


Figure 7.4: Conductance as a function of the number of atoms in the wire. For given values of t_{lead} and t_{wire} , we consider three cases: (a) $|\Delta\epsilon| = 0$, (b) $|\Delta\epsilon| = 0.2$ and (c) $|\Delta\epsilon| = 0.4$. For each case, we consider three types of coupling between lead and wire : green curve for strong coupling, black for direct coupling and red curve for weak coupling.

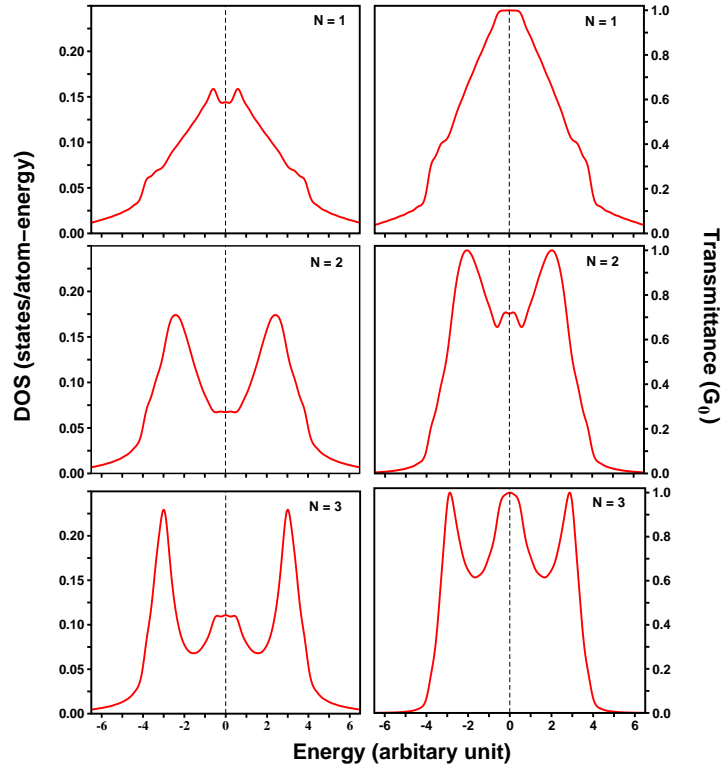


Figure 7.5: Density of states (left panel) and total transmittance (right panel) in no charge transfer ($|\Delta\epsilon| = 0$) and direct coupling ($t_c = t_{lead}$) situation for wires of lengths $N = 1$, $N = 2$ and $N = 3$ (from top to bottom). The dashed lines label the Fermi energy.

Increasing $|\Delta\epsilon|$ to 0.4, there will be larger charge transfer between the lead and wire. This causes a change in the parity of conductance oscillation from odd-even to even-odd for even shorter lengths : around wire lengths of 7 atoms as shown in Fig. 7.4c. From our study, it is therefore clear that the amplitude of conductance oscillation is mainly controlled by coupling coefficient between the leads and the wire, while the parity of the oscillation is controlled by the length of the wire and onsite energy difference between wire and lead Hamiltonians. There are few reports [27, 29] which indicate the change of parity of conductance oscillation and variation of oscillation amplitude for Na-atom wire.

To understand the odd-even oscillation in the conductance, we have calculated the density of states and transmittance as a function of energy for wires of lengths $N = 1$, $N = 2$ and $N = 3$ for the case of zero charge transfer. The results shown in Fig. 7.5 bring out

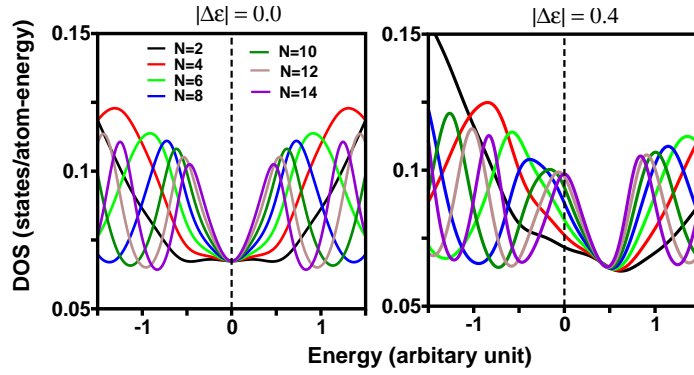


Figure 7.6: DOS around Fermi energy for several even numbered wires in two cases - $|\Delta\epsilon| = 0$ (left) and $|\Delta\epsilon| = 0.4$ (right). For $|\Delta\epsilon| = 0.4$, DOS at E_F gradually increases with wire size. For $N = 14$, the deep at E_F for $|\Delta\epsilon| = 0$ case is replaced by a peak at E_F for $|\Delta\epsilon| = 0.4$. Lead-wire coupling was considered to be of direct type in all cases.

the essential mechanism which has been discussed also in Ref. [26]. For odd-numbered atomic wires, the Fermi-energy falls in the non-bonding peak and it gives a maximum in the transmittance at $E = E_F$. On the other hand, for even numbered wire, the Fermi level lies in the minimum between the bonding and non-bonding peaks and consequently it exhibits a less transmission at $E = E_F$.

In order to explain the flipping of conductance oscillation from odd-even to even-odd, we have plotted in Fig. 7.6 the DOS around Fermi energy of several even numbered atomic wires for two cases of no charge transfer and finite charge transfer situations. When there is no charge transfer ($|\Delta\epsilon| = 0$), all the even numbered wires have a minimum in DOS at E_F . When we allow sufficient charge transfer to take place between wire and lead, DOS at E_F gradually increases with increasing length and at a critical size, a peak will appear in DOS at E_F . The opposite occurs for odd-numbered atomic wire (not shown in the Fig. 7.6) and the nature of conductance oscillations flips from odd-even to even-odd. If we increase the wire size further, again after another critical size, the odd-even nature of oscillations is restored. This repetition of even-odd or odd-even oscillation continues with increasing wire size. To investigate the effect of $|\Delta\epsilon|$ on the period of parity flip, we have plotted the conductance as a function of number of atoms in the wires in Fig. 7.7 for two different values of $|\Delta\epsilon|$ keeping coupling parameter fixed. One can see clearly that as

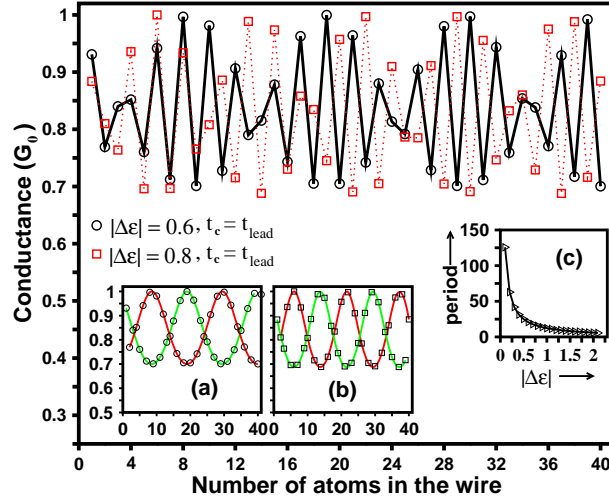


Figure 7.7: Plot of conductance as a function of wire size for two values of $|\Delta\epsilon|$: circles connected by solid line for $|\Delta\epsilon| = 0.6$ and squares connected by dashed line for $|\Delta\epsilon| = 0.8$. Conductances for all even numbered wires and all odd numbered wires are shown separately by red line and green line respectively within the insets. Inset (a) for $|\Delta\epsilon| = 0.6$ and inset (b) for $|\Delta\epsilon| = 0.8$. Inset (c) shows the variation of period of parity flip with $|\Delta\epsilon|$ and solid line through the right triangles is the fitted curve.

$|\Delta\epsilon|$ increases, frequency of parity flip increases *i.e.* period of parity flip decreases. To get a better insight into parity flip, we have shown in Fig. 7.7 the conductance variation of odd numbered and even numbered wires separately in insets (a) and (b) for $|\Delta\epsilon| = 0.6$ and $|\Delta\epsilon| = 0.8$ respectively. Each curve shows sinusoidal-like variations. Curves of even numbered and odd numbered wires together constitute loops. Length of one loop indicates the wire size required to flip the oscillation from odd-even to even-odd. The nodal points of loop indicate the boundaries between odd-even and even-odd. Two consecutive loops constitute a period. Number of loops in inset (b) is larger than in inset (a). Variation of period of parity-flip with $|\Delta\epsilon|$ is shown by right triangles in inset (c). For $|\Delta\epsilon| = 0$, there is no parity flip *i.e.* period is infinity. As $|\Delta\epsilon|$ increases, the period decreases. For sufficiently large value of $|\Delta\epsilon|$ ($\gg t_c$), the odd-even nature of conductance oscillation no longer persists. Period of conductance oscillation then changes to more than two atoms which is the characteristic of wires consisting of atoms of higher valency. Within

the odd-even nature of conductance oscillations, the period of parity flip goes roughly as $(A/|\Delta\epsilon|) + B$ with $A = 12.605$ and $B = -0.253$. However, coupling parameter t_c does not

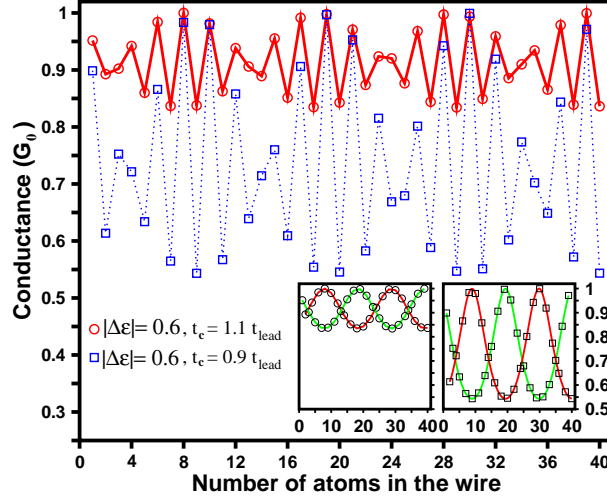


Figure 7.8: Plot of conductance as a function of wire size for two values of t_c - circles connected by solid line for $t_c = 1.1 t_{lead}$ and squares connected by dashed line for $t_c = 0.9 t_{lead}$. Conductances for all even numbered wires and all odd numbered wires are shown separately by red line and green line respectively. Left inset corresponds to $t_c = 1.1 t_{lead}$ and right one to $t_c = 0.9 t_{lead}$.

have any effect on period of parity flip. To check this, we have plotted the conductance variation with wire size in Fig. 7.8 for two different coupling constant t_c keeping $|\Delta\epsilon|$ fixed, while two insets show the conductance variation of odd numbered wires and even numbered wires separately (left inset corresponds to $t_c = 1.1 t_{lead}$ and right one to $t_c = 0.9 t_{lead}$). The number of loops in both the cases are same indicating t_c has no effect on the period. Larger width of loops in right inset compared to that in left inset indicates that t_c controls the amplitude of odd-even oscillations.

So far we have studied the role of the charge neutrality on the conductance oscillations of monoatomic wires considering the mirror symmetry between the two junctions. We found odd-even oscillation in the conductance. Moreover, for no charge transfer situation, conductance of odd numbered wires is quantized to G_0 , while for even numbered wires conductance is less than G_0 . Now we consider the situation where mirror symmetry

Table 7.1: Values of conductances for various wire lengths in absence of mirror symmetry. t_{c1} and t_{c2} are the two lead-wire couplings of the two junctions.

wire length (N)	$t_{c1} = t_{lead}$ $t_{c2} = t_{lead}$	$t_{c1} = t_{lead}$ $t_{c2} = 1.1 t_{lead}$	$t_{c1} = t_{lead}$ $t_{c2} = 1.2 t_{lead}$
1	0.9996	0.9906	0.9672
2	0.7164	0.7876	0.8482
3	0.9996	0.9906	0.9672
4	0.7164	0.7876	0.8482
5	0.9996	0.9906	0.9672

between two lead-wire junctions is broken by using two different coupling coefficients for two junctions, keeping charge-neutrality intact. Table 7.1 contains our result. Clearly, odd-even oscillations still occur, but the conductance quantization for odd numbered wires is weakened by reducing the value less than G_0 . This observation is in accordance with the previous study [24, 42].

7.4 Summery and conclusions

To conclude, we have used combination of real-space based scalar and vector recursion techniques to study the transport properties of a lead-wire-lead system. Our study on model system described by single band TB Hamiltonian provides a detail understanding of the effect of lead-wire coupling on the conductance of monoatomic wire. Working with model system, gives us the freedom of changing the model parameters and allows us to work with much longer wires than usually considered in literature. Odd-even oscillation in the conductance with increasing length of wire has been observed in agreement with earlier studies [3]-[30]. In presence of charge neutrality between the leads and the wire and in presence of perfect mirror symmetry between the incoming and outgoing leads, the conductance of odd numbered wires is quantized to G_0 , while it is less than G_0 for even numbered wires. As the charge neutrality is broken, the oscillation in conductance still exists, but with the distinction that for a given choice of charge transfer ($\Delta\epsilon$) and lead-wire hopping (t_c), the conductance values of the odd numbered and even numbered

wires are no longer fixed quantities as the size of the wires is changed. For such systems, we further found a change of phase of conductance oscillation from odd-even to even-odd with increasing number of atoms in the wire. We found that while the amplitude of oscillation depends on lead-wire coupling parameter t_c , it is the amount of charge transfer between lead and wire, which affects the period of oscillation. Lifting of mirror symmetry between two lead-wire junctions in no charge transfer condition is found to reduce the conductance of odd numbered wires below the quantized value of G_0 . The proposed technique can be easily generalized for application to realistic cases. To apply this approach to real systems, one needs to generate TB parameters of lead and wire via self consistent calculations while multi-orbital effect can be taken into account via multi-channel generalization of Landauer-Büttiker formula (see Eqn. 7.17). The proposed real space technique of calculation of conductance coupled with localized Wannier basis generated out of self-consistent DFT calculation [43, 44] can lead to a viable technique for study of quantum transmittance and conductance of nanoscale systems of various geometries in general.

Bibliography

- [1] A. I. Yanson, G. R. Bollinger, H. E. van der Brom, N. Agrait, J. M. van Ruitenbeek, *Nature* **395**, 783 (1998).
- [2] H. Ohnishi, Y. Kondo, K. Takayanagi, *Nature* **395**, 780 (1998).
- [3] R. H. M. Smit, C. Untiedt, G. Rubio-Bollinger, R. C. Segers, J. M. van Ruitenbeek, *Phys. Rev. Lett.* **91**, 076805 (2003).
- [4] W. H. A. Thijssen, D. Marjenburgh, R. H. Bremmer, J. M. van Ruitenbeek, *Phys. Rev. Lett.* **96**, 026806 (2006).
- [5] J. M. Krans, J. M. van Ruitenbeek, V. V. Fisun, I. K. Yanson, L. J. de Jongh, *Nature (London)* **375**, 767 (1995); A. I. Yanson, I. K. Yanson, J. M. van Ruitenbeek, *ibid.* **400** 144 (1999).
- [6] P. Sautet, C. Joachim, *Phys. Rev. B* **38**, 12238 (1988).
- [7] E. G. Emberly, G. Kirzenow, *Phys. Rev. B* **58**, 10911 (1988).
- [8] K. Hirose, M. Tsukada, *Phys. Rev. Lett.* **73**, 150 (1994).
- [9] K. Hirose, M. Tsukada, *Phys. Rev. B* **51**, 5278 (1995).
- [10] H. J. Choi, J. Ihm, *Phys. Rev. B* **59**, 2267 (1999).
- [11] P. A. Khomyakov, G. Brocks, *Phys. Rev. B* **70**, 195402 (2004).
- [12] N. D. Lang, *Phys. Rev. B* **52**, 5335 (1995); N. D. Lang, *Phys. Rev. Lett.* **79**, 1357 (1997).

- [13] M. D. Ventura, S. T. Pantelides, N. D. Lang, *Phys. Rev. Lett.* **84**, 979 (2000).
- [14] Y. Xue, S. Datta, M. A. Ratner, *Chem. Phys.* **281**, 151 (2001).
- [15] M. Brandbyge, J. L. Mozos, P. Ordejon, J. Taylor, K. Stokbro, *Phys. Rev. B* **65**, 165401 (2002).
- [16] K. S. Thygesen, M. V. Bollinger, K. W. Jacobsen, *Phys. Rev. B* **67**, 115404 (2003).
- [17] A. Calzolari, N. Marzari, I. Souza, M.B. Nardelli, *Phys. Rev. B* **69**, 035108 (2004).
- [18] P. Khomyakov, G. Brocks, V. Karpan, M. Zwierzycki, P. J. Kelly, *Phys. Rev. B* **72**, 035450 (2005).
- [19] R. Haydock, V. Heine, M. J. Kelly, *J. Phys. C :Solid State Phys* **5**, 2845 (1972).
- [20] R. Haydock, *Solid State Physics*, editor: H. Ehrenreich, F. Sietz, D. Turnbull (Academic, New York, 1980) volume 35.
- [21] T. J. Godin, R. Haydock, *Phys. Rev. B* **38**, 5237 (1988).
- [22] N. D. Lang, *Phys. Rev. Lett.* **79**, 1357 (1997).
- [23] S. Tsukamoto, K. Hirose, *Phys. Rev. B* **66**, 161402 (2002).
- [24] H. -S. Sim, H. -W. Lee, K. J. Chang, *Phys. Rev. Lett.* **87**, 096803 (2001).
- [25] P. Havu, T. Torsti, M. J. Puska, R. M. Nieminen, *Phys. Rev. B* **66**, 075401 (2002).
- [26] P. Khomyakov, G. Brocks, *Phys. Rev. B* **74**, 165416 (2006).
- [27] R. Gutierrez, F. Grossmann, R. Schmidt, *Acta Phys. Pol. B* **32**, 443 (2001).
- [28] Y. Egami, T. Ono, K. Hirose, *Phys. Rev. B* **72**, 125318 (2005).
- [29] P. Major, V. G. Suarez, S. Sirichantaropass, J. Cserti, C. J. Lambert, J. Ferrer, G. Tichy, *Phys. Rev. B* **73**, 045421 (2006).
- [30] J. K. Viljas, J. C. Cuevas, F. Pauly, M. Hafner, *Phys. Rev. B* **72**, 245415 (2005).

- [31] K. S. Thygesen, K. W. Jacobsen, *Chem. Phys.* **319**, 111 (2005).
- [32] T. J. Godin, R. Haydock, *Comp. Phys. Comm.* **64**, 123 (1991).
- [33] I. Dasgupta, T. Saha, A. Mookerjee, *Phys. Rev. B* **47**, 3097 (1993).
- [34] S. Datta, D. Choidhuri, T. Saha-Dasgupta, S. Sengupta, *Eur. Phys. Lett.* **73**, 765 (2006).
- [35] K. Xia, M. Zwierzycki, M. Talanana and P. J. Kelly, *Phys. Rev. B* **73**, 064420 (2006).
- [36] The process of vector recursion converts the lattice into a one-dimensional chain, which is then folded to clump two sites of the chain together to define the vector basis set. For a chain with folded configuration (see Ref. [21] for details) both the reflected and transmitted waves move in the opposite direction to that of the incident wave.
- [37] The Fermi energy of the lead-wire composite system is determined by the macroscopic lead Hamiltonian.
- [38] M. B. Nardelli, *Phys. Rev. B* **60**, 7828 (1999).
- [39] P. A. Khomyakov and G. Brocks, *Phys. Rev. B* **70**, 195402 (2004).
- [40] K. Tarafder, T. Mitra and A. Mookerjee, *Physica B* **371**, 100 (2006).
- [41] K. K. Saha *et al*, *Phys. Rev. B* **77**, 085427 (2008).
- [42] H. -W. Lee and C. S. Kim, *Phys. Rev. B* **63**, 075306 (2001).
- [43] N. Marzari, D. Vanderbilt, *Phys. Rev. B* **56**, 12847 (1997).
- [44] O. K. Andersen, T. Saha-Dasgupta, *Phys. Rev. B* **62**, R16219 (2000).